

STRUCTURAL OPTIMIZATION OF COMPOSITE AND ALUMINUM
HORIZONTAL TAIL PLANE OF A HELICOPTER

A THESIS SUBMITTED TO
THE GRADUATE SCHOOL OF NATURAL AND APPLIED SCIENCE
OF
THE MIDDLE EAST TECHNICAL UNIVERSITY

BY

BERTAN ARPACIOĞLU

IN PARTIAL FULFILLMENT OF THE REQUIREMENTS
FOR
THE DEGREE OF MASTER OF SCIENCE
IN
AEROSPACE ENGINEERING

MAY 2019

Approval of the thesis:

**STRUCTURAL OPTIMIZATION OF COMPOSITE AND ALUMINUM
HORIZONTAL TAIL PLANE OF A HELICOPTER**

submitted by **Bertan Arpaciođlu** in partial fulfillment of the requirements for the degree of **Master of Science in Aerospace Engineering Department, Middle East Technical University** by,

Prof. Dr. Halil Kalıpçılar
Dean, Graduate School of **Natural and Applied Sciences** _____

Prof. Dr. İsmail Hakkı Tuncer
Head of Department, **Aerospace Engineering** _____

Prof. Dr. Altan Kayran
Supervisor, **Aerospace Engineering, METU** _____

Examining Committee Members:

Assoc. Prof. Dr. Demirkan Çöker
Aerospace Engineering, METU _____

Prof. Dr. Altan Kayran
Aerospace Engineering, METU _____

Assoc. Prof. Dr. Ercan Gürses
Aerospace Engineering, METU _____

Assoc. Prof. Dr. Melin Şahin
Aerospace Engineering, METU _____

Prof. Dr. Kemal Levend Parnas
Mechanical Engineering, TEDU _____

Date: 03.05.2019

I hereby declare that all information in this document has been obtained and presented in accordance with academic rules and ethical conduct. I also declare that, as required by these rules and conduct, I have fully cited and referenced all material and results that are not original to this work.

Name, Surname: Bertan Arpaciođlu

Signature:

ABSTRACT

STRUCTURAL OPTIMIZATION OF COMPOSITE AND ALUMINUM HORIZONTAL TAIL PLANE OF A HELICOPTER

Arpacioğlu, Bertan
Master of Science, Aerospace Engineering
Supervisor: Prof. Dr. Altan Kayran

May 2019, 164 pages

This thesis presents structural optimization studies of aluminum and composite material horizontal tail plane structure of a helicopter by using MSC.NASTRAN optimization capabilities. Structural design process starts from conceptual design phase, and structural layout design is performed by using CATIA. In the preliminary design phase, study focuses on minimum weight optimization with multiple design variables and similar constraints for both materials.

Aerodynamic load calculation is performed using ANSYS and pressure distribution is used as the common loading for both aluminum and composite horizontal tail. Horizontal tail plane finite element model is created by using MSC.PATRAN. According to the characteristics of materials, design variables are chosen. For aluminum horizontal tail, thickness and flange areas are used as design variables; and for composite horizontal tail, attention is mainly focused on the ply numbers and ply orientations of the laminated composite panels. By considering manufacturability issues, discrete design variables are used. For different mesh sizes, initial values of the design variables, and design constraints, optimizations are repeated and the results of optimizations are examined and compared with each other. In the optimizations performed, constraints are taken as strength and local buckling constraints.

It is shown that the optimization methodology used in this thesis gives confident results for optimizing structures in the preliminary design phase.

Keywords: Multidisciplinary Structural Optimization, Structural Design, Finite Element Analysis, Horizontal Tail Plane, Helicopter

ÖZ

KOMPOZİT VE ALÜMİNYUM BİR HELİKOPTER YATAY KUYRUK KANADININ YAPISAL OPTİMİZASYONU

Arpacıođlu, Bertan
Yüksek Lisans, Havacılık ve Uzay Mühendisliđi
Tez Danışmanı: Prof. Dr. Altan Kayran

Mayıs 2019, 164 sayfa

Bu tez, MSC.NASTRAN optimizasyon yetenekleri kullanılarak, alüminyum ve kompozit malzemeli helikopter yatay kuyruk kanadının yapısal optimizasyon çalışmalarını sunmaktadır. Yapısal tasarım süreci kavramsal tasarım aşamasından başlamaktadır ve CATIA kullanılarak yapısal yerleşim tasarımı gerçekleştirilmiştir. Ön tasarım aşamasında, çalışma, her iki malzeme için birden fazla tasarım değişkeniyle ve benzer kısıtlarla minimum ağırlık optimizasyonuna odaklanmaktadır.

ANSYS kullanılarak aerodinamik yük hesaplaması yapılmıştır ve hem alüminyum hem de kompozit yatay kuyruk için ortak yük olarak basınç dağılımı kullanılmıştır. Yatay kuyruk sonlu elemanlar modeli MSC.PATRAN kullanılarak yaratılmıştır. Malzemelerin özelliklerine göre tasarım değişkenleri seçilmiştir. Alüminyum yatay kuyruk için, tasarım değişkenleri olarak kalınlık ve flanş alanları kullanılmıştır ve kompozit yatay kuyruk için esas olarak lamine kompozit panellerin kat sayılarına ve kat oryantasyonlarına dikkat edilmiştir. İmal edilebilirlik konuları dikkate alınarak, belirli tasarım değişkenleri kullanılmıştır. Farklı ağ boyutları, tasarım değişkenlerinin başlangıç değerleri ve tasarım kısıtlamaları için optimizasyonlar tekrar edilmiş ve optimizasyonların sonuçları incelenerek ve birbirleriyle karşılaştırılmıştır. Yapılan optimizasyonlarda kısıtlamalar, dayanım ve yerel burkulma kısıtları olarak alınmıştır.

Bu tezde kullanılan optimizasyon metodolojisinin, ön tasarım aşamasında yapıları optimize etmek için güvenilir sonuçlar verdiği gösterilmiştir.

Anahtar Kelimeler: Çok Disiplinli Yapısal Optimizasyon, Yapısal Tasarım, Sonlu Elemanlar Analizi, Yatay Kuyruk Kanadı, Helikopter

to my beloved wife & my lovely family

ACKNOWLEDGMENTS

First of all, I would like to express my sincere appreciation to my supervisor Prof. Dr. Altan KAYRAN for his guidance, support and helpful advices throughout the research and giving me the opportunity to work with him.

Besides my supervisor, I would like to thank my dear wife for listening, emotionally supporting and bearing with me during the whole process.

I would like to thank my company TAI for supporting its employees in the academic field. I would also thank to my colleagues who helped me deciding on such a study.

I would also like to thank my parents; this study is ended thanks to their prayers.

TABLE OF CONTENTS

ABSTRACT.....	v
ÖZ	vii
ACKNOWLEDGMENTS.....	x
TABLE OF CONTENTS	xi
LIST OF TABLES	xiv
LIST OF FIGURES	xv
LIST OF ABBREVIATIONS	xxi
CHAPTERS	
1. INTRODUCTION	1
1.1. Introduction	1
1.2. Literature Survey.....	2
1.3. Scope and Contents of the Study.....	5
1.4. MSC.NASTRAN Optimization Process	7
2. DESIGN OF HORIZONTAL TAIL PLANE OF HELICOPTER.....	13
2.1. Description of Horizontal Tail Plane	13
2.2. Structural Design.....	14
2.3. Creation of the FE Mesh Model	17
3. DETERMINATION OF AERODYNAMIC LOADING	21
3.1. Introduction	21
3.2. CFD Analysis of the Horizontal Tail	22
3.3. Interpolation of the Aerodynamic Forces from CFD Mesh to the FE Mesh..	26
4. OPTIMIZATION OF THE ALUMINUM HTP	37
4.1. Introduction	37

4.2. Material Properties	37
4.3. FE Model Properties.....	40
4.4. Formulation of the Optimization Problem for the Aluminum HTP.....	40
4.4.1. Design Variables	40
4.4.1.1. Discrete Design Variables.....	43
4.4.1.2. Initial Values of the Design Variables	45
4.4.2. Constraints.....	46
4.4.2.1. Strength Constraints	46
4.4.2.2. Local Buckling Constraints.....	49
4.4.2.3. Thickness Constraints	50
4.4.3. Objective Function of the Optimization.....	52
4.5. Optimization Results	52
4.5.1. Optimization Using Continuous Design Variables	52
4.5.2. Optimization Using Discrete Design Variables	57
4.6. Optimization of the Aluminum HTP Using Line Distributed Load.....	65
5. OPTIMIZATION OF THE COMPOSITE HTP	69
5.1. Introduction	69
5.2. Material Properties	69
5.3. FE Model Properties.....	70
5.4. Formulation of the Optimization Problem for the Composite HTP.....	73
5.4.1. Design Variables	73
5.4.1.1. Discrete Design Variables.....	75
5.4.1.2. Initial Values of the Design Variables	75
5.4.2. Constraints.....	76
5.4.2.1. Strength Constraints	76
5.4.2.2. Local Buckling Constraints.....	77

5.4.2.3. Thickness Constraints	87
5.4.3. Objective Function of the Optimization.....	87
5.5. Optimization Results	87
6. BENCHMARKING OF ALUMINIUM AND COMPOSITE MATERIALS AND COMPARISON OF OPTIMIZATION RESULTS.....	105
6.1. Introduction	105
6.2. Advantages of Composites and Aluminum.....	105
6.3. Disadvantages of Composites and Aluminum	106
6.4. Comparison of Optimization Results for the Aluminum and Composite HTP	107
7. CONCLUSION.....	109
7.1. General Conclusion	109
7.2. Recommendation for Future Work.....	111
REFERENCES.....	113
APPENDICES	117
APPENDIX A.....	117
APPENDIX B	119
APPENDIX C	149
APPENDIX D.....	157
APPENDIX E	161

LIST OF TABLES

TABLES

Table 1.1: Stages, tasks, outputs, and tools that are used in the study	7
Table 1.2: Convergence Criteria Parameters (P and P-1 refer to the current and previous cycle) [4].....	11
Table 2.1: Element and node numbers for three different mesh densities	20
Table 4.1: Material properties and strengths used in the aluminum HTP optimization [22]	39
Table 4.2: Design variables defined for the aluminum HTP optimization	43
Table 4.3: Discrete design variable values for the aluminum HTP optimization	44
Table 4.4: Selection of discrete and continuous design variables.....	45
Table 4.5: Minimum, middle and maximum input values of the design variables within the lower and upper limits of the design variables.....	45
Table 4.6: All constraints applied for the aluminum HTP optimization	50
Table 4.7: Thickness constraints	51
Table 4.8: Optimization results for the strength constraint only using continuous design variables.....	54
Table 4.9: Optimization results for the combined strength and local buckling constraints using continuous design variables	56
Table 4.10: Optimization results for the combined strength and local buckling constraints using discrete design variables.....	60
Table 4.11: Optimization results for the combined strength and local buckling constraints using discrete design variables with line distributed load applied.....	67
Table 5.1: Material properties of HexplyAS4/8552/RC34/AW134.....	70
Table 5.2: Design variables (ply thickness and orientation) for the composite HTP optimization.....	74
Table 5.3: Discrete design variables used for the composite HTP optimization	75
Table 5.4: Local buckling load comparison of NASTRAN and Equation (5.2) results for various design regions	85
Table 5.5: Optimization results for the strength constraint only with discrete design variables	97

LIST OF FIGURES

FIGURES

Figure 1.1: Optimization process used in this study	5
Figure 1.2: MSC.NASTRAN SOL 200 implementation of structural optimization [15]	8
Figure 1.3: Soft convergence decision logic of SOL 200 [4]	9
Figure 1.4: Hard convergence decision logic of SOL 200 [4]	10
Figure 2.1: Horizontal tail plane creating negative lift	13
Figure 2.2: NACA 4415 airfoil profile	14
Figure 2.3: Left HTP consisting of two spars and six skins.....	16
Figure 2.4: Finalized conceptual model of horizontal tail plane.....	16
Figure 2.5: Surfaces imported from CATIA to PATRAN.....	17
Figure 2.6: Mesh 1 density.....	18
Figure 2.7: Mesh 2 density.....	19
Figure 2.8: Mesh 3 density.....	19
Figure 2.9: Mesh 3 with displacement boundary conditions	20
Figure 3.1: ANSYS Project Schematic that is followed	22
Figure 3.2: ANSYS Geometry Toolbox Surfaces.....	23
Figure 3.3: Air volume mesh that is created	23
Figure 3.4: Boundary conditions.....	24
Figure 3.5: Pressure distribution [Pa] on the lower skin.....	25
Figure 3.6: Pressure distribution [Pa] on the upper skin and the wing tip.....	25
Figure 3.7: Velocity [knot] stream lines	26
Figure 3.8: Imported pressure data [MPa] in Patran environment (lower skin and wing tip)	27
Figure 3.9: Imported pressure data [MPa] in Patran environment (upper skin and wing tip)	27
Figure 3.10: CFD Mesh density and three different mesh densities.....	28
Figure 3.11: Comparison of the CFD pressure with the interpolated FE pressure on the Mesh 1 for upper skin.....	29

Figure 3.12: Comparison of the CFD pressure with the interpolated FE pressure on the Mesh 1 for lower skin.....	29
Figure 3.13: Comparison of the CFD pressure with the interpolated FE pressure on the Mesh 2 for upper skin.....	30
Figure 3.14: Comparison of the CFD pressure with the interpolated FE pressure on the Mesh 2 for lower skin.....	30
Figure 3.15: Comparison of the CFD pressure with the interpolated FE pressure on the Mesh 3 for upper skin.....	31
Figure 3.16: Comparison of the CFD pressure with the interpolated FE pressure on the Mesh 3 for lower skin.....	31
Figure 3.17: Constraint forces of interpolated pressure in lift direction on Mesh 1 ..	32
Figure 3.18: Constraint forces of interpolated pressure in lift direction on Mesh 2 ..	32
Figure 3.19: Constraint forces of interpolated pressure in lift direction on Mesh 3 ..	33
Figure 3.20: Total lift force vs. element numbers of Mesh 1, 2 and 3	33
Figure 3.21: Displacement result for Mesh 1	34
Figure 3.22: Displacement result for Mesh 2	35
Figure 3.23: Displacement result for Mesh 3	35
Figure 3.24: Displacement vs. element numbers of Mesh 1, 2 and 3	36
Figure 4.1: Spars and root rib which are made of 7050 T7451 aluminum plate material.....	38
Figure 4.2: Ribs which are made of aluminum 2024 T42 sheet plate.....	38
Figure 4.3: Skins which are made of 2024 T3 sheet plate aluminum material.	39
Figure 4.4: 1D rod elements (yellow lines) and 2D shell elements (blue surfaces)...	40
Figure 4.5: Upper skin design variables and variable names	41
Figure 4.6: Lower skin design variables and variable names	41
Figure 4.7: Rib design variables and variable names	42
Figure 4.8: Spar design variables and variable names	42
Figure 4.9: One rivet line connection example	43
Figure 4.10: Normal y stresses on spars.....	47
Figure 4.11: Normal y stresses on skins.....	48
Figure 4.12: Thickness constraints.....	51

Figure 4.13: Continuous optimization iterations for the Mesh 1 / Three different initial values for design variables / Strength constraint only	53
Figure 4.14: Continuous optimization iterations for the Mesh 2 / Three different initial values for design variables / Strength constraint only	53
Figure 4.15: Continuous optimization iterations for the Mesh 3 / Three different initial values for design variables / Strength constraint only	54
Figure 4.16: Continuous optimization iterations for the Mesh 1 / Three different initial values for design variables / Strength and local buckling constraints	55
Figure 4.17: Continuous optimization iterations for the Mesh 2 / Three different initial values for design variables / Strength and local buckling constraints	55
Figure 4.18: Continuous optimization iterations for the Mesh 3 / Three different initial values for design variables / Strength and local buckling constraints	56
Figure 4.19: Discrete optimization iterations for the Mesh 1 / Three different initial values for design variables / Strength and local buckling constraints	58
Figure 4.20: Discrete optimization iterations for the Mesh 2 / Three different initial values for design variables / Strength and local buckling constraints	58
Figure 4.21: Discrete optimization iterations for the Mesh 3 / Three different initial values for design variables / Strength and local buckling constraints	59
Figure 4.22: Optimum thickness variation for the Mesh 3 HTP with the upper skin / Minimum initial values / Discrete design variables / Strength and buckling constraints together	61
Figure 4.23: Optimum thickness variation for the Mesh 3 HTP without the upper skin / Minimum initial values / Discrete design variables / Strength and buckling constraints together	61
Figure 4.24: Maximum value of the constraint vs. iteration number of the optimization that gives 7.21 kg as the optimum mass	62
Figure 4.25: Shear stresses in the elements of the upper middle skin 6 th region	63
Figure 4.26: Normal y stresses in the elements of the upper middle skin 6 th region .	64
Figure 4.27: Line distributed load application on Mesh 1 through the front spar	65
Figure 4.28: Line distributed load application on Mesh 2 through the front spar	66
Figure 4.29: Line distributed load application on Mesh 3 through the front spar	66

Figure 4.30: Discrete optimization iterations for the minimum initial value design variables / Three different mesh densities / Strength and local buckling constraints / line distributed load applied	67
Figure 5.1: Material coordinate axis for spars.....	71
Figure 5.2: Material coordinate axis for lower skin	71
Figure 5.3: Material coordinate axis for upper skin	72
Figure 5.4: Material coordinate axis for ribs.....	72
Figure 5.5: Rib design regions and design region names.....	73
Figure 5.6: Spar design regions and design region names	74
Figure 5.7: Initial stacking sequence for all design regions	76
Figure 5.8: Plate with under compressive load	78
Figure 5.9: Critical buckling load variation versus the axial wave number m.....	79
Figure 5.10: Simply supported composite plate subjected to unit distributed unit load	80
Figure 5.11: Buckling analysis result for relatively fine mesh	80
Figure 5.12: Fine meshed middle lower skin, 3 th zone.....	81
Figure 5.13: Simply supported panel with distributed unit load applied to the middle lower skin in the 3 th zone	82
Figure 5.14: Buckling analysis result for the middle lower skin 3 th zone with the [-45/90/90/45/0/0] _s stacking sequence	82
Figure 5.15: Variation of the critical buckling load with the m value for the middle lower skin, 3 th zone	83
Figure 5.16: Simply supported flat panel with distributed unit load applied to the front spar web in the 4 th zone	83
Figure 5.17: Buckling analysis result for the front spar 4 th zone with the [-45/90/90/45/45/0/0] _s stacking sequence	84
Figure 5.18: Variation of the critical buckling load with the m value for the front spar web in the 4 th zone.....	84
Figure 5.19: Implementation of the composite strength and local buckling constraints into the optimization process.....	86
Figure 5.20: Optimization iterations for the Mesh 1 / Thickness as the only design variable / Strength constraint only	88

Figure 5.21: Optimum thickness variation for the Mesh 1 HTP without upper skin / Thickness as the only design variable / Strength constraint only	88
Figure 5.22: Optimum thickness variation for the Mesh 1 HTP with upper skin / Thickness as the only design variable / Strength constraint only	89
Figure 5.23: Optimization iterations for the Mesh 2 / Thickness as the only design variable / Strength constraint only	89
Figure 5.24: Optimum thickness variation for the Mesh 2 HTP without upper skin / Thickness as the only design variable / Strength constraint only	90
Figure 5.25: Optimum thickness variation for the Mesh 2 HTP with upper skin / Thickness as the only design variable / Strength constraint only	90
Figure 5.26: Optimization iterations for the Mesh 3 / Thickness as the only design variable / Strength constraint only	91
Figure 5.27: Optimum thickness variation for the Mesh 3 HTP without upper skin / Thickness as the only design variable / Strength constraint only	91
Figure 5.28: Optimum thickness variation for the Mesh 3 HTP with upper skin / Thickness as the only design variable / Strength constraint only	92
Figure 5.29: Optimization iterations for the Mesh 1 / Thickness and fiber orientation angle as design variables / Strength constraint only	93
Figure 5.30: Optimum thickness variation for the Mesh 1 HTP without upper skin / Thickness and fiber orientation angle as design variables / Strength constraint only	93
Figure 5.31: Optimum thickness variation for the Mesh 1 HTP with upper skin / Thickness and fiber orientation angle as design variables / Strength constraint only	94
Figure 5.32: Optimization iterations for the Mesh 2 / Thickness and fiber orientation angle as design variables / Strength constraint only	94
Figure 5.33: Optimum thickness variation for the Mesh 2 HTP without upper skin / Thickness and fiber orientation angle as design variables / Strength constraint only	95
Figure 5.34: Optimum thickness variation for the Mesh 2 HTP with upper skin / Thickness and fiber orientation angle as design variables / Strength constraint only	95
Figure 5.35: Optimization iterations for the Mesh 3 /Thickness and fiber orientation angle as design variables / Strength constraint only	96
Figure 5.36: Optimum thickness variation for the Mesh 3 HTP without upper skin / Thickness and fiber orientation angle as design variables / Strength constraint only	96

Figure 5.37: Optimum thickness variation for the Mesh 3 HTP with upper skin / Thickness and fiber orientation angle as design variables / Strength constraint only	97
Figure 5.38: Average stress distribution for the Mesh 1 HTP in 1 st iteration / Thickness and fiber orientation angle as design variables / Strength constraint only	98
Figure 5.39: Average stress distribution for the Mesh 2 HTP in 1 st iteration / Thickness and fiber orientation angle as design variables / Strength constraint only	98
Figure 5.40: Average stress distribution for the Mesh 3 HTP in 1 st iteration / Thickness and fiber orientation angle as design variables / Strength constraint only	99
Figure 5.41: Optimization results for the Mesh 3 / Thickness as the only design variable / Strength and local buckling constraints	100
Figure 5.42: Optimum thickness variation for the Mesh 3 HTP without upper skin / Thickness as the only design variable / Strength and local buckling constraints	100
Figure 5.43: Optimum thickness variation for the Mesh 3 HTP with upper skin / Thickness as the only design variable / Strength and local buckling constraints	101
Figure 5.44: Optimization results for the Mesh 3 / Thickness and fiber orientation angle as design variables / Strength and local buckling constraints	101
Figure 5.45: Optimum thickness variation for the Mesh 3 HTP without upper skin / Thickness and fiber orientation angle as design variables / Strength and local buckling constraints.....	102
Figure 5.46: Optimum thickness variation for the Mesh 3 HTP with upper skin / Thickness and fiber orientation angle as design variables / Strength and local buckling constraints.....	103
Figure 5.47: Combined optimization results for the Mesh 3 / Strength and local buckling constraints.....	103
Figure 6.1: Comparison of optimization results for aluminum and composite HTP	108

LIST OF ABBREVIATIONS

AOA	Angle of Attack
CAD	Computer Aided Design
CATIA	Computer Aided Three Dimensional Interactive Application
CID	Coordinate System Identity
CFD	Computational Fluid Dynamics
CFRP	Carbon Fiber Reinforced Plastic
CNC	Computer Numerical Control
DOE	Design of Experiments
FE	Finite Element
HTP	Horizontal Tail Plane
MATLAB	Matrix Laboratory
MSC	The MacNeal-Schwendler Corporation
NACA	National Advisory Committee for Aeronautics
NASTRAN	NASA Structure Analysis
OA	Orthogonal Arrays
TAI	Turkish Aerospace Industries Inc.
UD	Unidirectional

CHAPTER 1

INTRODUCTION

1.1. Introduction

Nowadays, optimization techniques are gaining attention especially in the early stages of product development in aerospace industry. In addition, composite materials are developing; therefore, in every aerospace structure, industry is trying to replace aluminum material with composite material because of their advance characteristics, lightweight and special abilities. This does not mean that composites are much better than aluminum in every aspect; aluminum material still has trusted characteristics and production techniques. In this thesis, these two special materials frequently used in aerospace industry are benchmarked in the optimization study of a helicopter horizontal tail plane (HTP). Structural weight is usually taken as the objective function and minimum weight HTP is sought for.

In the aerospace industry, projects are very long lasting as they need so much design iteration on load calculations and associated analyses. As mentioned previously, optimizations are gaining attention because optimization tools are very timesaving tools in the preliminary design stage. Optimization results create preliminary design outputs, and optimization techniques are very fast way to get these outputs. It should be noted that optimization results cannot be implemented directly in a real structure that would be produced. They should be used as detail design stage inputs. In the detail design stage, actual values of the design variables are determined. When

optimized inputs are used in the detail design stage, iterations in the detail design stage decrease. In conclusion, optimization techniques used in the preliminary design stage speed up the whole project time.

1.2. Literature Survey

When literature is examined in detail, there are numerous studies about structural design, finite element analysis, and structural optimization methods. Structural optimization is mentioned firstly in 1869 at Maxwell's basic theory which explains truss structures with only stress constraint and minimum weight objective under a single load condition [1]. However, design of an aircraft structure is determined by multidisciplinary criteria such as stress, buckling, fatigue, flutter etc. Recent developments show that engineers can make structural multi-disciplinary optimizations with what is known today.

In recent years, aircraft industry programmed many in-house multi-disciplinary optimization tools. Paper of Barker and Johnson shows that Lockheed Martin has collaborated with MSC to enhance MSC.NASTRAN SOL 200 and LM's in-house optimization tools. Paper describes new functional features of the core MSC.NASTRAN product and ongoing development efforts to achieve manufacturable structural designs. They also illuminate the need for further investigation of design variable selection methods for optimum composite structure complexity [2]. As it is seen, MSC.NASTRAN is a developing commercial program that has also SOL 200 solver that is capable of multi-disciplinary optimizations.

MSC.NASTRAN optimization code is based on sequential linear programming and sequential quadratic programming [3]. The optimization algorithms used in MSC.NASTRAN belong to the family of methods generally referred to as "gradient-based" [4]. In 2010, Sevastyanov investigated two multi-objective optimization methods named as multi-gradient explorer and multi-gradient pathfinder. These methods are based on "gradient-based" multi-objective optimizations and his paper

points out “gradient-based” algorithms optimize computationally expensive models, and are able to optimize models with thousands of design variable [5].

Kennedy and Martins (2012), presented a ply parametrization technique for layered composites. This parametrization takes into account the discrete selection of ply angles, layup thicknesses, and the continuity of ply angles. They applied the technique to structural optimization problems that have thousands of design variables and hundreds of constraints. They stated that their proposed laminate parametrization technique is well suited for “gradient-based” design optimization. As an example, they applied their method to the sizing of a composite wing-box, they also showed that the proposed parametrization is effective for a wide range of structural optimization problems [6].

In an article named ‘The Optimization of Wing Structures’, Butler gives potential applications of today’s structural optimization methods related with wing design. Article is a survey and explains design variables, constraints and objective functions about these methods [7].

In the paper of Shabeer and Murtaza (2013), optimization of an aircraft wing with composite skins, aluminum spars and aluminum ribs is done by only considering minimum stress and displacement as objective. Their design variables were five different ply sequences. They used CATIA V5 in structural modelling and MSC.PATRAN in finite element modelling. Optimum design is selected only comparing tip displacements and von Mises stresses of wings with five different ply sequences that used on composite skins [8].

Muralikrishna et al. examined design optimization of a rotorcraft horizontal tail plane in their paper. Their geometrical modeling is carried out by Unigraphics NX7.5 and FE is modelled by the pre-processor of MSC.PATRAN. Static analyses are done using MSC.NASTRAN. They designed an aluminum HTP and then extend their studies for a composite HTP. Their optimum structures are selected according to design experiments. The results obtained from the design experiments were used for

the verification and the tuning of the initially developed structural model. In the paper, the total weight reduction from aluminum HTP to composite HTP is pointed out as 43.8% [9].

In 2001, Liu applied a two-level optimization procedure for composite wing design subject to strength and buckling constraints. At wing-level design, continuous optimization of ply thicknesses with orientations of 0° , 90° , and $\pm 45^\circ$ is performed to minimize weight. At the panel level, the number of plies of each orientation rounded to integers, and genetic algorithm is used to optimize the stacking sequence. His procedure allows the use of continuous optimization for the overall design, avoiding the high computational cost associated with optimization of all panels simultaneously [10].

Engelstad, et al. investigated optimization strategies for F/A-22 horizontal tail plane. They compared three methods. Their second method was MSC.NASTRAN Sol 200 by using external responses from closed form buckling software and their third method was MSC.NASTRAN Sol 200 by using native linear buckling solutions. They stated that while second method requires a coarse-grid mesh, third method requires a fine-grid mesh in order to accurately compute linear buckling modes across the individual panels of the structure [11].

In 2018, Dababneh, et al. revealed that the change in the optimized mass value for an aluminum or composite aircraft wing structure is related with different starting values for the design variables, as well as different optimization algorithms in the optimization process. The paper also shows that composite construction materials used in optimization dramatically alter the size of the design space. The results of the paper show the effectiveness of the proposed procedures in finding an optimized solution for high-dimensional search space cases with a given level of accuracy and reasonable computational resources and user efforts [12].

In his thesis, Rongxin Xu made structural optimization for a composite wing skin using MSC.NASTRAN. Thickness and layup of the laminated upper and lower

stiffened skin panels are used as design variables. Multiple constraints are given including failure criterion related to laminate strength, minimum flutter speed and minimum percentage of each ply orientation. As result of the thesis, 36% lower skin weight achieved which contributed to 7.7% weight reduction in the whole outer wing structure by only optimizing the laminated skins [13].

In conclusion, literature shows many examples of multidisciplinary optimizations with so many design variables and constraints in aircraft structures like wings designed by composite and aluminum materials. In addition, use of “gradient-based” method, which MSC.NASTRAN Sol 200 solver has, is one of the best ways of solving these kinds of minimum mass optimizations.

1.3. Scope and Contents of the Study

The main objective of this thesis is to design and optimize a composite and an aluminum horizontal tail plane of a helicopter, and also to compare these two optimized designs. Motivation of the thesis is to design a lightweight and an enduring horizontal tail plane of a helicopter by showing the pros and cons of aluminum and composite material design. The general flowchart used in this study is shown in Figure 1.1.

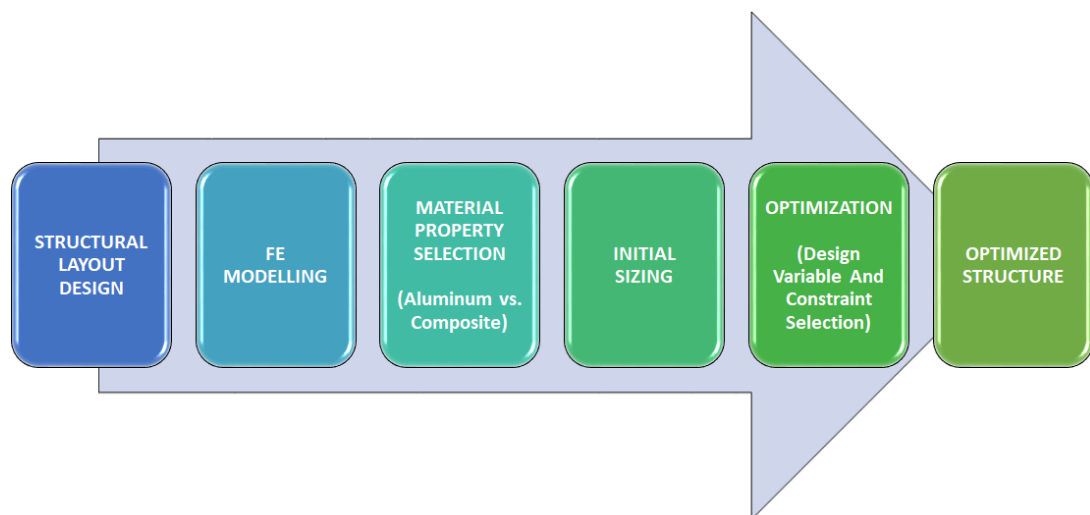


Figure 1.1: Optimization process used in this study

This schematic flowchart is a brief explanation of process that is followed. In the second chapter, horizontal tail plane structure is described and designed. According to the structural layout design, finite element model and boundary conditions are created for both aluminum and composite HTPs. Every finite element analysis requires material properties, boundary conditions and load application. For materials that are chosen, material properties are appointed. Then, boundary conditions of the FE model are identified and calculated loads are applied.

Determination of aerodynamic loads is described in the third chapter. Created CFD model, CFD analysis and selected load case are explained. Then interpolation of the CFD pressure loads to the FE model is shown and comparisons are made.

In chapters four and five, aluminum and composite HTP optimizations are explained, respectively. Material properties and finite element procedures are described in detail. Then, the optimization problem statements are given. Optimization problem statement is composed of three items.

- Design variables:

$$(x_1, x_2, \dots)$$

- Design constraints:

$$g_1(x_1, x_2, \dots) = 0 \tag{1.1}$$

$$g_2(x_1, x_2, \dots) \leq 0 \tag{1.2}$$

⋮

- Design objective:

$$f_{min}(x_1, x_2, \dots)$$

Design variables are the answer of “What parameters are allowed to vary to reach the design objective?” question. Design constraints are restrictions that must be satisfied and design objective is a main goal which is tried to be minimized or maximized. These items are explained in detail in aluminum and composite HTP optimization studies presented in Chapters 4 and 5, respectively.

While explaining design variables, initial sizing is given for both optimizations. All optimizations described in chapter four and five are performed using MSC.NASTRAN [14] SOL 200 solver.

All tasks and tools are tabulated in Table 1.1.

Table 1.1: Stages, tasks, outputs, and tools that are used in the study

Stages	Tasks	Outputs	Tools
Conceptual Design	Structure Layout Design	3D Model	CATIA
	Material Selection	Material Property	MSC.PATRAN
Preliminary Design	Initial Sizing		
	Finite Element Modelling	FE Model	
	Static Analysis	Stress, Failure Index	MSC.NASTRAN
	Buckling Analysis	Buckling Mode	
Optimization	Optimized Structure		

1.4. MSC.NASTRAN Optimization Process

Finite element analyses and numerical methods are used in optimization studies for years. For large-scale optimization problems, FE solvers need very powerful computers. Also creating such complex finite element structures takes time for engineers. Hence, in early days of optimization, optimization techniques were not used very effectively. Today, engineers who have basic understanding of optimization and finite element analysis can easily make optimizations with the help of recent advances in MSC.PATRAN pre-post processor, and MSC.NASTRAN SOL 200 solver. SOL 200 solver has an implementation of structural optimization shown in Figure 1.2.

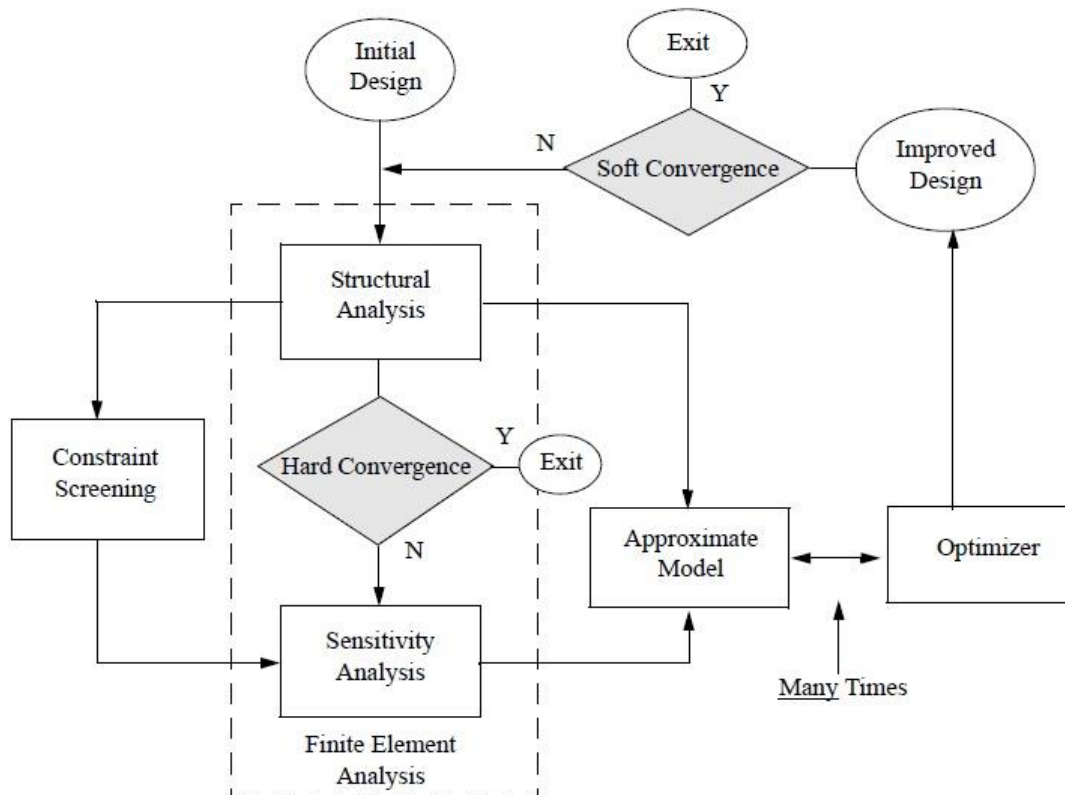


Figure 1.2: MSC.NASTRAN SOL 200 implementation of structural optimization [15]

In Figure 1.2, optimization process is described as a flow chart. First, an initial design is created by the user. Then this design goes through a structural analysis, and structural analysis results are used to create an approximate model while constraint screening activity is done. Constraint screening activity identifies whether constraints are violated or likely to be violated, and temporarily removes those constraints which are below the threshold value in the current design cycle. Design sensitivity analysis is done only for those constraints which are kept after constraint screening. Sensitivity analysis calculates changes in constraint values with respect to changes in the design variables defined. By gathering information from sensitivity analysis and structural analysis, an approximate model is created. Then, optimization is done by the optimizer using the approximate model with gradient-based methods. MSC.NASTRAN 2010 uses IPOPT optimization code as optimizer [16]. Soft

convergence compares the design variables, properties output from the approximate optimization with those of the input to the approximate optimization, and an improved design has been obtained. The improved design is a new starting model prepared with the optimizer results so that a new structural analysis is done. Before the structural analysis, improved design is compared with the previous design. If changes are close to the desired values, process reaches a soft convergence.

After an improved design structural analysis is done, one more convergence is performed. Hard convergence compares the most recent finite element analysis with those from the previous design cycle. Since this test compares exact results from two consecutive analyses, it is named as hard convergence. If improved design structural analysis reaches hard convergence, optimization stops.

In soft convergence if the changes in the design variables and properties are not significant, the objective and constraints are unchanged and there is no need to continue optimization. Soft convergence decision logic flowchart is shown in Figure 1.3.

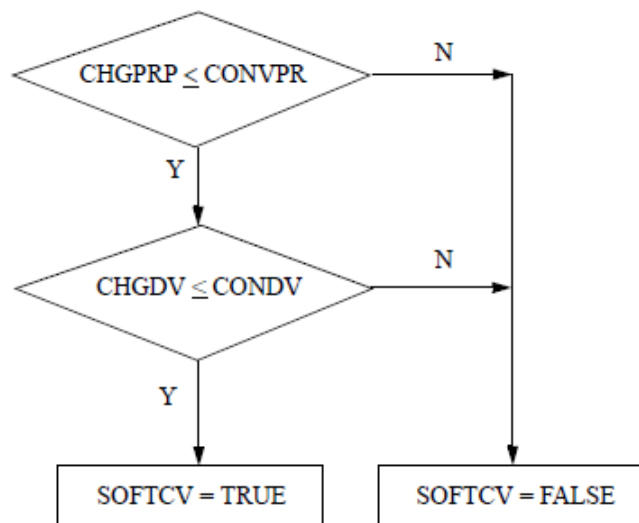


Figure 1.3: Soft convergence decision logic of SOL 200 [4]

Parameters in Figure 1.3 are explained in Table 1.2. Result of the soft convergence is a true or false value for the logical variable SOFTCV. Cycle terminates only if SOFTCV is true and the parameter SOFTEXTIT is yes.

Hard convergence is a decision of whether the optimization iterations should continue or not if the maximum allowable number of design cycles (DESMAX) has not been reached. If a hard convergence criterion is reached, optimization process always stops. In Figure 1.4, hard convergence decision logic flowchart is given.

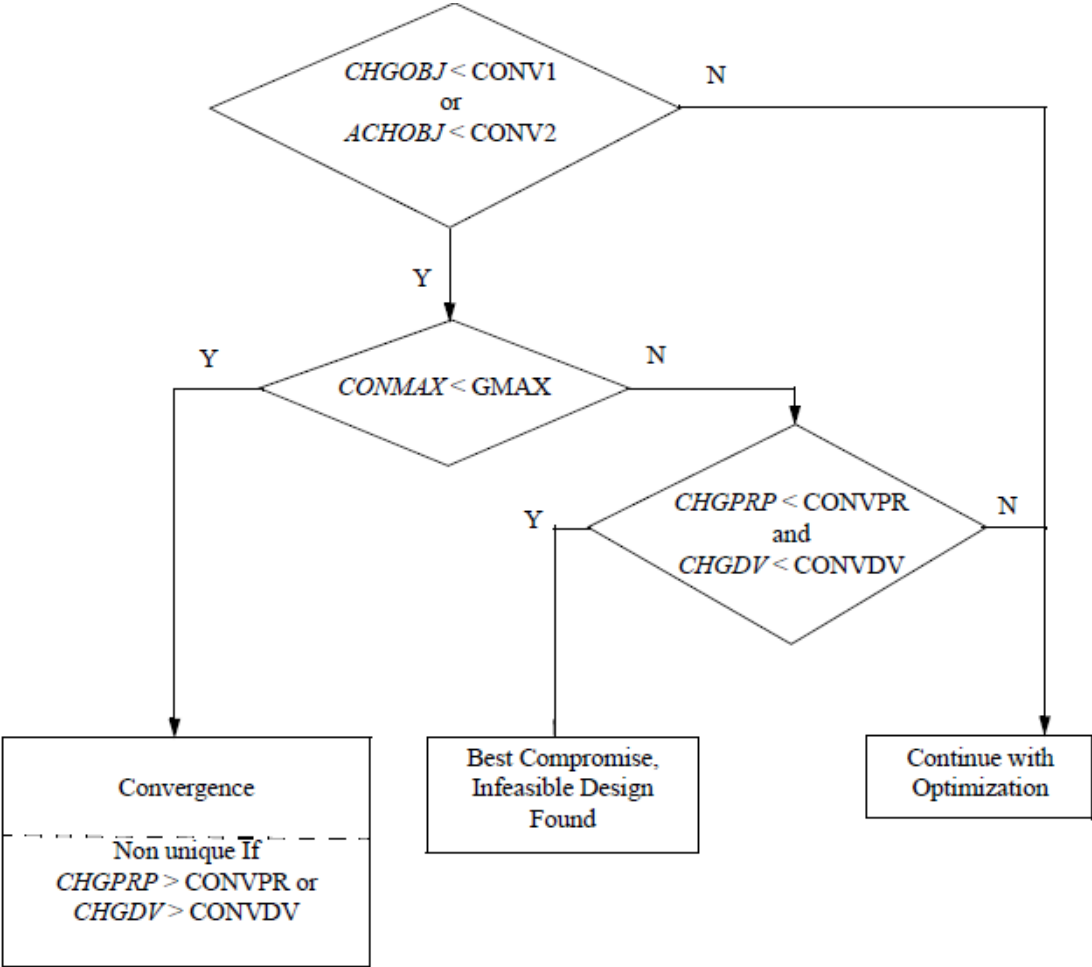


Figure 1.4: Hard convergence decision logic of SOL 200 [4]

Parameters in Figure 1.4 are explained in Table 1.2. According to Figure 1.4, the first check is done in the objective function. The reasoning behind the usage of an ‘OR’

test is based on the relative and absolute changes in the objective function. When an optimization is done, objective could be a very large number or a very small number. While trying to converge to a large number, relative changes like plus or minus range of a kilogram could be sufficient. On the other hand, while converging to a very small number, minimization of the absolute change could be more meaningful. If objective function check is a ‘Y’, another check is performed in constraints. In constraints check, the maximum constraint value should be less than its maximum value. If this criterion is satisfied, then optimization stops.

Table 1.2: Convergence Criteria Parameters (P and P-1 refer to the current and previous cycle) [4]

Internal Variable	Definition	Parameters	Default
CHGPRP	$\max_{1 \leq i \leq NPROP} \left(\left \frac{P_i^{(P)} - P_i^{(P-1)}}{P_i^{(P-1)}} \right \right)$	CONVPR	0.001
CHGDV	$\max_{1 \leq i \leq NDV} \left(\left \frac{x_i^{(P)} - x_i^{(P-1)}}{x_i^{(P-1)}} \right \right)$	CONVDV	0.001 (1.0E-4 for topology optimization)
CHGOBJ	$\left \frac{OBJ^{(P)} - OBJ^{(P-1)}}{OBJ^{(P-1)}} \right $	CONV1	0.001 (1.0E-5 for topology optimization)
ACHOBJ	$OBJ^{(P)} - OBJ^{(P-1)}$	CONV2	1.00E-20
CONMAX	$\max_k \{g_k(\mathbf{x})\}$	GMAX	0.005

CHAPTER 2

DESIGN OF HORIZONTAL TAIL PLANE OF HELICOPTER

2.1. Description of Horizontal Tail Plane

Horizontal tail plane is a small wing located at the tail part of the air vehicles. The aim of designing a horizontal tail plane is to get horizontal stability and horizontal control by keeping the airplane from pitching over nose down. Because of that, it is also called as horizontal stabilizer. Getting horizontal stability could be different for various air vehicles. According to the airplane type, flight mission or position of the center of gravity, horizontal tail planes need to create positive or negative lift for stability. Most of the time for the conventional arrangements of design, the produced lift from horizontal tail plane is negative.

Apart from airplanes, a helicopter horizontal tail plane needs to create negative lift and balance the nose up moment which is created by helicopter main rotor in forward flight as shown in Figure 2.1.

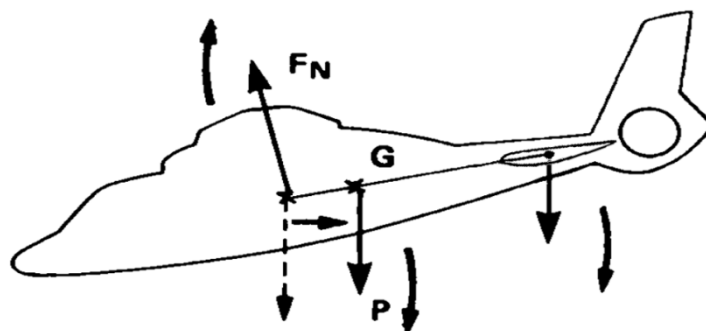


Figure 2.1: Horizontal tail plane creating negative lift

In addition to the helicopter rotor, its fuselage has an inherent negative stability derivative in pitch and the stabilizer helps to give the helicopter better overall handling qualities [17]. As negative lift is required, a downward airfoil profile should be used for fixed horizontal tail. In cruise, helicopters fly lower speeds when they compared to airplanes. In low speeds, thicker airfoil profiles create more lift. Because of these, downward NACA 4415 airfoil profile is chosen for the airfoil of the horizontal tail. This airfoil has very high drag force as it has a thick profile. High drag force is also a desired force when the tail rotor of the helicopter does not function.

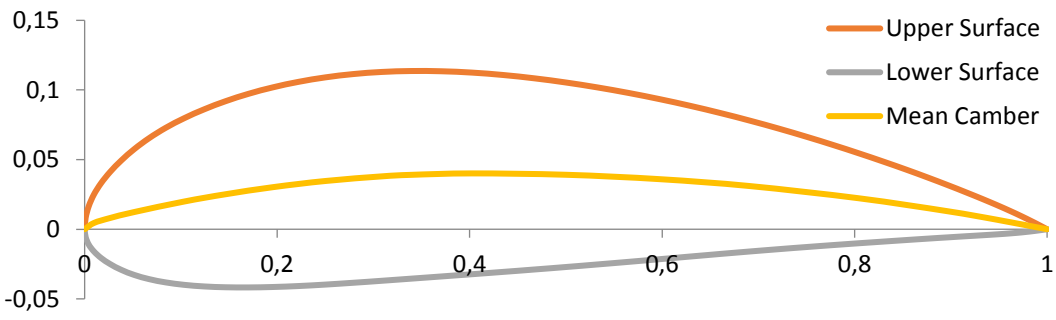


Figure 2.2: NACA 4415 airfoil profile

In this study, a downward NACA 4415 airfoil profile is chosen for a fixed horizontal tail plane. Figure 2.2 shows the NACA 4415 airfoil.

2.2. Structural Design

Master geometry of a helicopter horizontal tail plane should be design according to aerodynamic responses of helicopter that should be design, but that is not scope of this study. Therefore, a master geometry is created just for this study. As master geometry, horizontal tail plane has a 2830 mm wingspan, its chord length is 600 mm, and it is a constant chord length rectangular wing. To simplify the optimization problem, left hand side of the horizontal tail plane is used.

Wing structures frequently encounter bending moment because of its boundary conditions and aerodynamic forces. To overcome this bending moment, wing structures need spars. In addition to that, wing has an airfoil profile, and this profile can only be produced with skins. To preserve skins' airfoil shape, to connect spars with skins and to encounter the shear load, wing structures also need ribs.

A horizontal tail plane could have one or more than one spars. Number of spars should be determined based on the connection concept of horizontal tail plane to the helicopter. Regardless of the amount of spars, there should be a spar at aerodynamic center which can be described as the point about which pitching moment does not vary with the angle of attack. Position of aerodynamic center is located nearly at 25% chord length from the leading edge. Selecting a rectangular wing type results in having the spar line as a parallel line to the leading edge at 25% chord position. For the remaining 75% of chord, decision should be made depending on the connection concept. Conceptual design phase should be initiated with assumptions, such as assuming horizontal tail plane is fixed from two locations from the left hand side of horizontal tail plane, so one more spar could be added. This spar is located at 35% chord length from the front spar as remaining 75% starts narrowing around that percentage. Consequently, there exists two spars in the horizontal tail plane, which are named as front and rear spar. In this manner, horizontal tail plane is divided into three regions, namely leading edge, middle and trailing edge.

Various portions of skin are grouped as upper leading edge, lower leading edge, upper middle skin, lower middle skin, upper trailing edge, and lower trailing edge as shown in Figure 2.3. Skins that are named as upper middle and lower middle skin are in between two spars. Leading edge skins are in front of the front spar, and trailing edge skins are behind the rear spar.

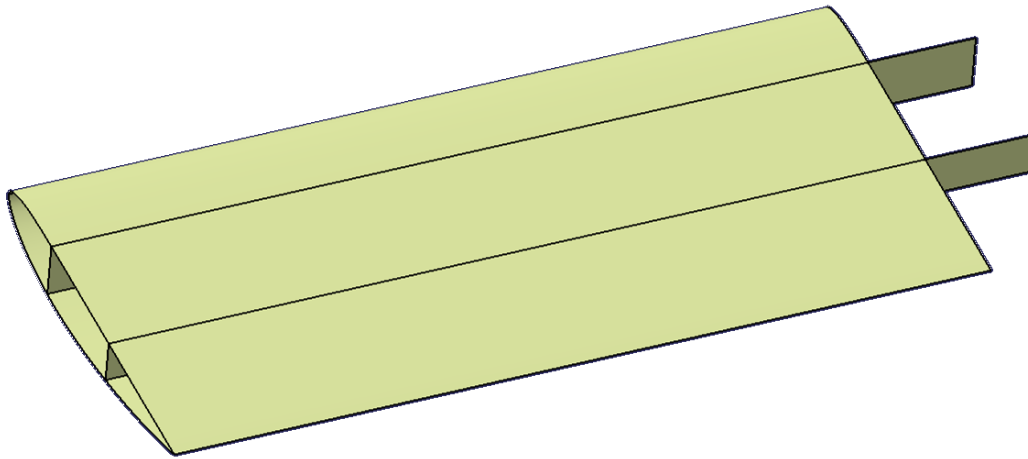


Figure 2.3: Left HTP consisting of two spars and six skins

As the nature of conceptual design phase, rib count is selected by making assumptions. It is decided to have six rib locations, which divide wing's aerodynamic surface equally. In addition to these ribs, assuming a center wing part that is in the helicopter, there should be one more middle rib in the root. According to that, middle skins are extended until that rib. Ribs are in front of the front spar, between the two spars and behind the rear spar. Ribs that are located in front of the front spar are called as leading edge ribs, ribs that are located between spars are called as middle ribs and ribs that are located behind the rear spar are called as trailing edge ribs. In total, there are 19 ribs in the horizontal tail plane structure as pointed out in Figure 2.4.

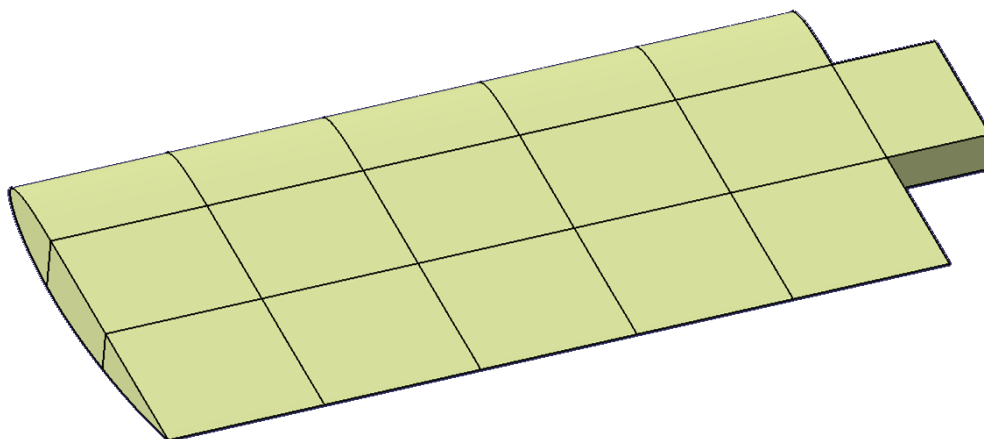


Figure 2.4: Finalized conceptual model of horizontal tail plane

Rib configuration creates various regions on the skins and the spars as seen in Figure 2.4. These regions are investigated as design regions. Depending on the material type, different design variables defined for each region and all materials used in this study are chosen as the most used materials according to TAI's production and supply capabilities. In this study, optimization problem of the horizontal tail plane structure is solved by making every design region optimum.

2.3. Creation of the FE Mesh Model

After the structure is built and modeled in CAD environment in CATIA [18], surfaces that are to be meshed are imported to MSC PATRAN [19]. At first, they are imported as general trimmed surfaces to PATRAN as shown in Figure 2.5 and then they transformed to simply trimmed surfaces which have default color green, as simple trimmed surfaces have four outer edges and it can be meshed with isoparametric meshing.

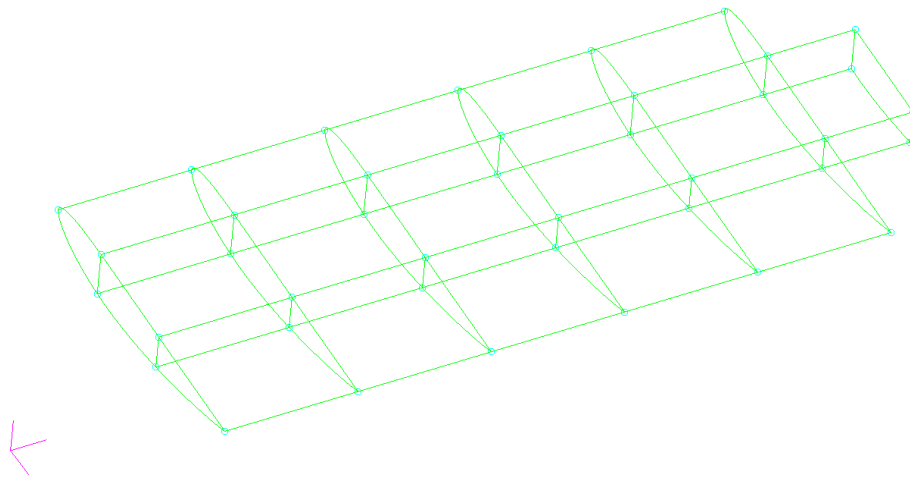


Figure 2.5: Surfaces imported from CATIA to PATRAN

Surfaces are ready for mesh. For optimization problems, fine mesh is not desirable for large-scale strength optimization. Fine meshes are often used to capture large stress gradients in local details. The mesh density should be fine enough to capture

the average stress in each design region [20]. Keeping that in mind, three different mesh densities are created.

First mesh density is named as Mesh 1 and it has equivalent number of elements as the number of design regions as shown in Figure 2.6. For every surface that is imported, one element is created. This mesh density is created because this kind of mesh density is used for Global Finite Element Model (GFEM) in structural analyses, especially in aerospace structures. In total 63 elements are created for Mesh 1 density. For the leading and the trailing edge ribs, 12 TRIA3 elements are modeled. TRIA3 elements are namely three-noded triangular elements. For other surfaces, 51 QUAD4 elements are modeled. QUAD4 elements are four-noded quadrilateral elements.

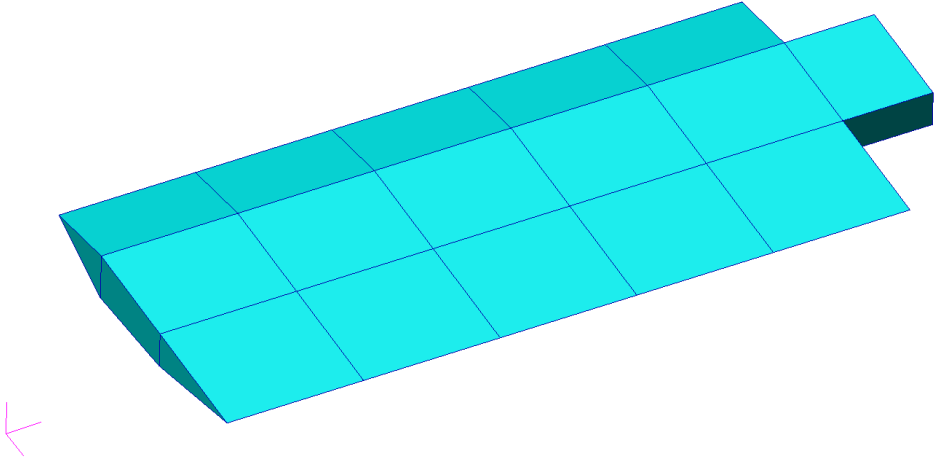


Figure 2.6: Mesh 1 density

Then for every surface, mesh density is increased. For second mesh density, all rib regions have 2 elements, all spar regions except root have 3 elements, all skin regions except root have 6 elements. Root spars have 2 elements and root skins have 4 elements. Second mesh density is called as Mesh 2. As shown in Figure 2.7, leading and trailing edge ribs have 12 TRIA3 elements again, and other 248 elements are QUAD4.

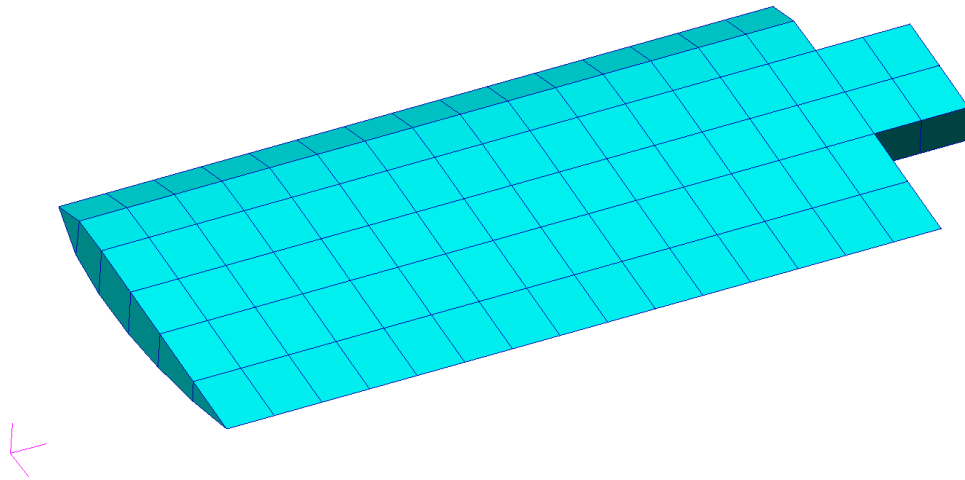


Figure 2.7: Mesh 2 density

After creating Mesh 2, Mesh 3 is created and mesh density is increased more. In Mesh 3 density, all meshes are QUAD4 and there are 876 elements.

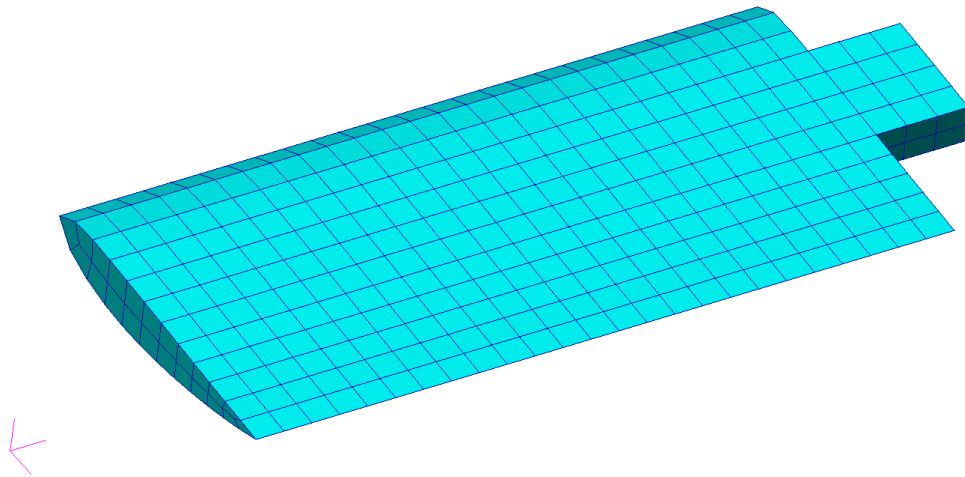


Figure 2.8: Mesh 3 density

As displacement boundary condition, all mesh densities are fixed from the corners of the root of the wing in 6 degrees of freedom. It is visualized on Mesh 3 as shown in Figure 2.9.

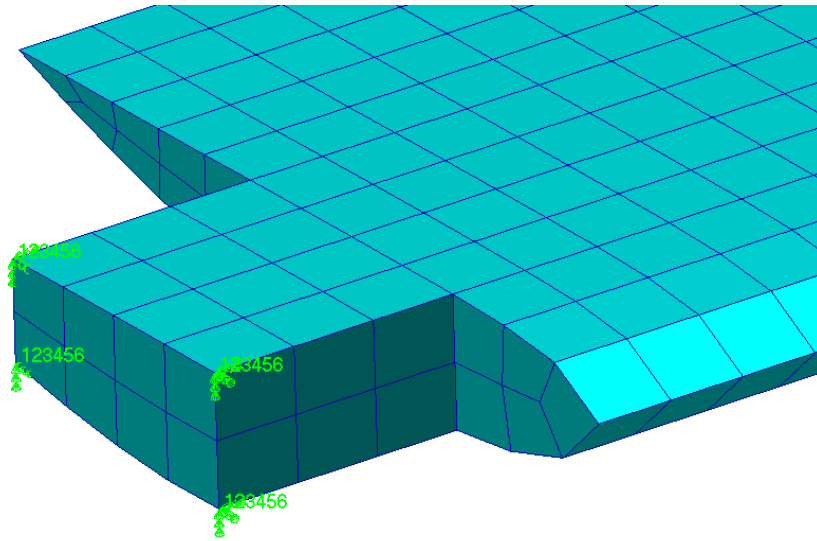


Figure 2.9: Mesh 3 with displacement boundary conditions

Element and node quantities according to mesh densities are tabulated as shown on Table 2.1.

Table 2.1: Element and node numbers for three different mesh densities

	Element Number	Node Number
MESH 1	63	40
MESH 2	260	204
MESH 3	876	770

CHAPTER 3

DETERMINATION OF AERODYNAMIC LOADING

3.1. Introduction

Applied load is important for any kind of structural optimization. In this study, the type of loading that should be applied is determined. Loading could be some critical load cases which include more than one loading type. Different load cases could size different parts of structure; however, optimization with more than one load takes too much time. Finally, it is decided that one load case could be enough to explain methodology of the thesis.

In the description of the horizontal tail plane, it is explained that horizontal tail plane generally works in cruise flight condition. It is also explained that NACA 4415 airfoil is chosen. Keeping them in mind, load is calculated for the maximum cruise speed and for an angle of attack at which the airfoil provides maximum lift coefficient. Maximum cruise speed is taken into account as 165 knot for the helicopter and maximum angle of attack is selected as 14.3° for NACA 4415 airfoil [21]. C_l -alpha curve for NACA 4415 is given in APPENDIX A.

For the 165 knot maximum cruise speed and angle of attack of 14.3° , a pressure distribution for horizontal tail plane's outer surface is calculated as the load to be used in the optimization study using computational fluid dynamics (CFD) analysis.

3.2. CFD Analysis of the Horizontal Tail

To calculate the pressure distribution on the wing surface using CFD analysis, ANSYS 14.5 program is used. In this work, a simple CFD analysis is done. Project Schematic that is followed in ANSYS is as shown in Figure 3.1.

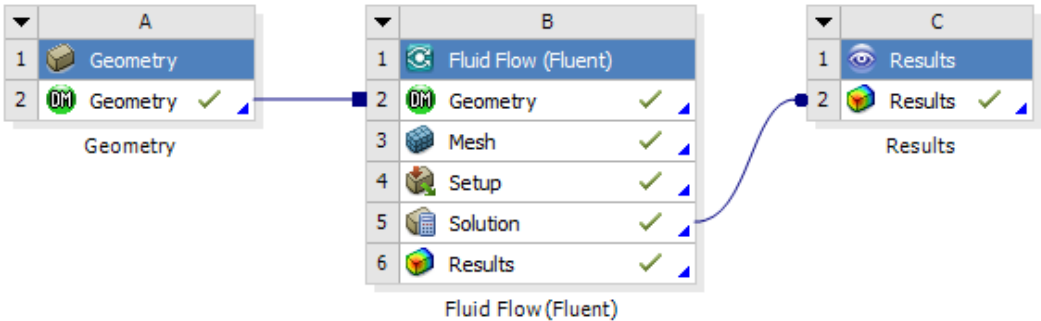


Figure 3.1: ANSYS Project Schematic that is followed

To make a CFD analysis, air volume geometry should be created first. Geometry that is designed by using CATIA is imported to ANSYS 14.5 Geometry Toolbox. Then wing surface is set by rotating it by -14.3 degree to get -14.3 degree angle of attack and its associated pressure distribution. Horizontal tail is rotated downward because horizontal tail plane has downward profile and generating negative lift. Air volume is created as a bigger box than the horizontal tail plane and the imported horizontal tail plane volume is removed from the air volume to observe how the air flows over the outer surfaces of the wing. Then, air inlet, air outlet, wing surface, tail cone side surface and other symmetry surfaces are defined as shown in Figure 3.2.

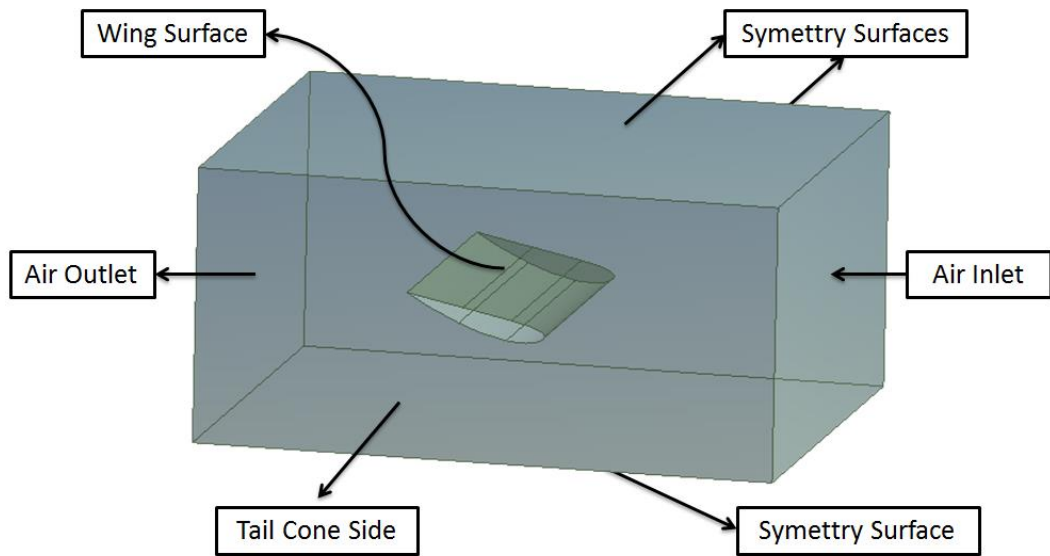


Figure 3.2: ANSYS Geometry Toolbox Surfaces

After the air volume and the wing surfaces are defined, Fluent 14.5.7 Toolbox is opened and geometry, which is prepared in the Geometry Toolbox, is imported to the Fluent Toolbox. Then meshing is opened and air volume meshed as shown in Figure 3.3. Air volume that is close to the wing surface is fine meshed.

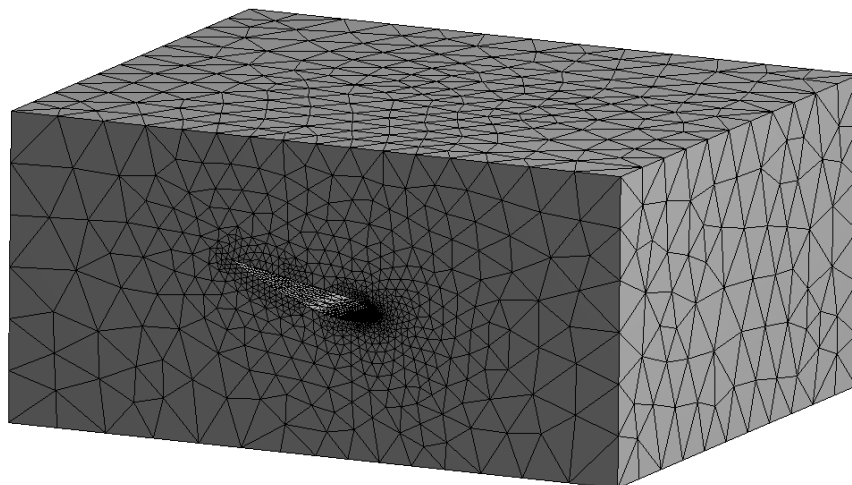


Figure 3.3: Air volume mesh that is created

After the completion of the meshing, Fluent Flow is opened, and boundary conditions and airflow information such as density, viscosity, temperature, velocity vs. are defined.

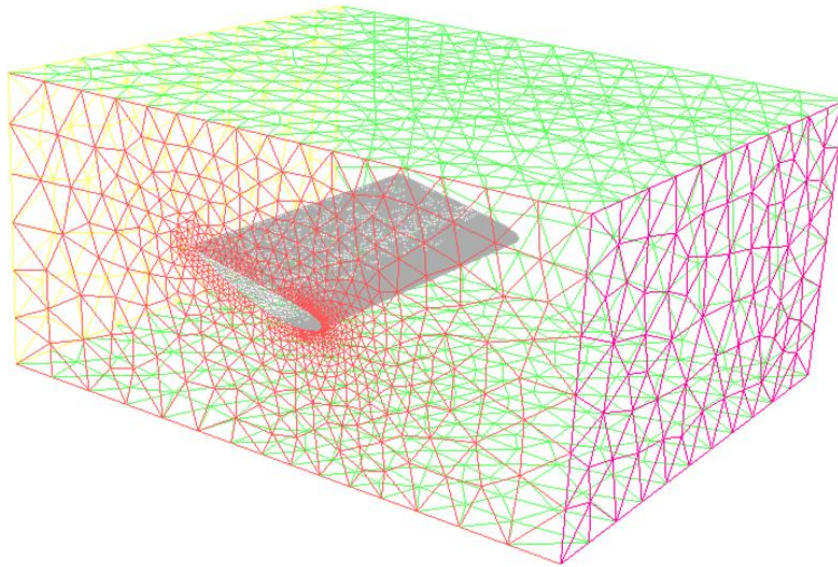


Figure 3.4: Boundary conditions

In Figure 3.4, boundary conditions used in the CFD analysis are seen. Magenta mesh surface, which is in front of the leading edge of the wing, is the air inlet surface; its type is chosen as velocity-inlet and velocity magnitude is given as 84.66 m/s (165 knot). Yellow mesh surface, which is behind the trailing edge of the wing, is the air outlet surface; its type is chosen as pressure-outlet and gauge pressure is given as zero Pascal to refer to steady air. Green surfaces are symmetry surfaces; their types are chosen as symmetry surfaces. This is an assumption meaning that surfaces away from the wing have zero pressure gradients. Finally, red mesh surfaces are the tail cone surface and gray mesh surfaces are the wing outer surfaces. Their types are chosen as wall and they are assumed as stationary wall surfaces.

As results, static pressure distribution is calculated and observed as shown in ANSYS Fluent Toolbox. Figures 3.5 and 3.6 show the pressure distribution on the lower and upper skins of the horizontal tail.

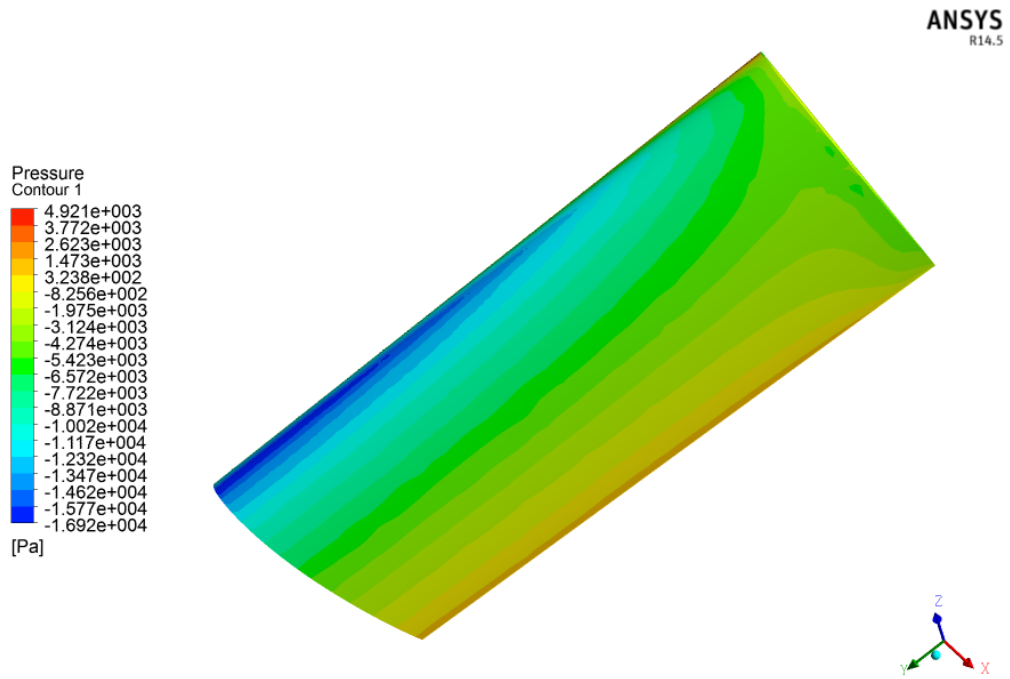


Figure 3.5: Pressure distribution [Pa] on the lower skin

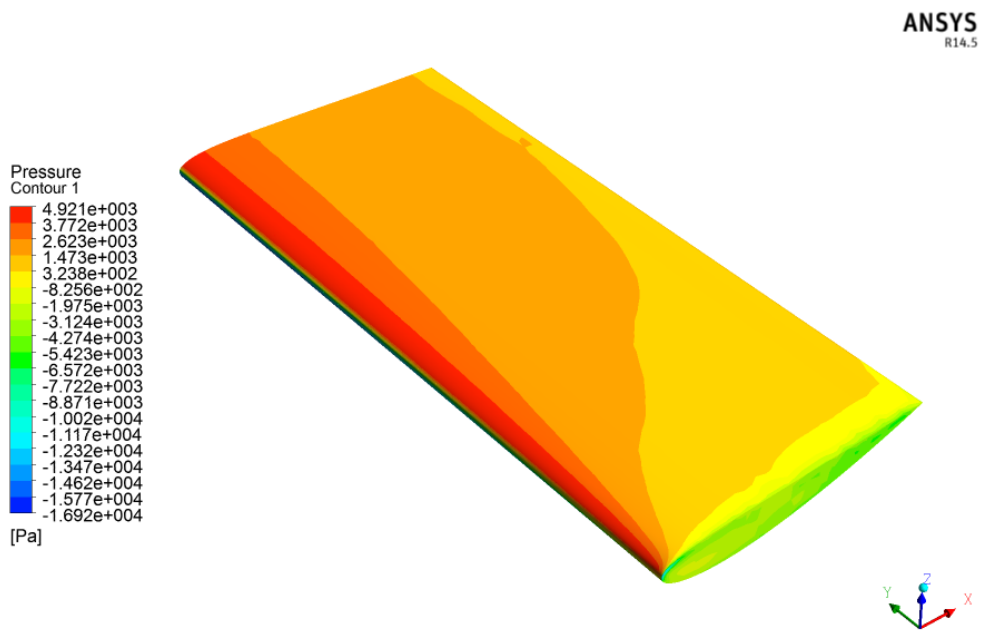


Figure 3.6: Pressure distribution [Pa] on the upper skin and the wing tip

It is clearly seen that pressure on the upper skin is higher than the pressure on the lower skin, and this shows that there is negative lift on the wing structure. In addition, velocity streamlines could be seen as shown on Figure 3.7. On green lines, air velocity is equal to 165 knot.

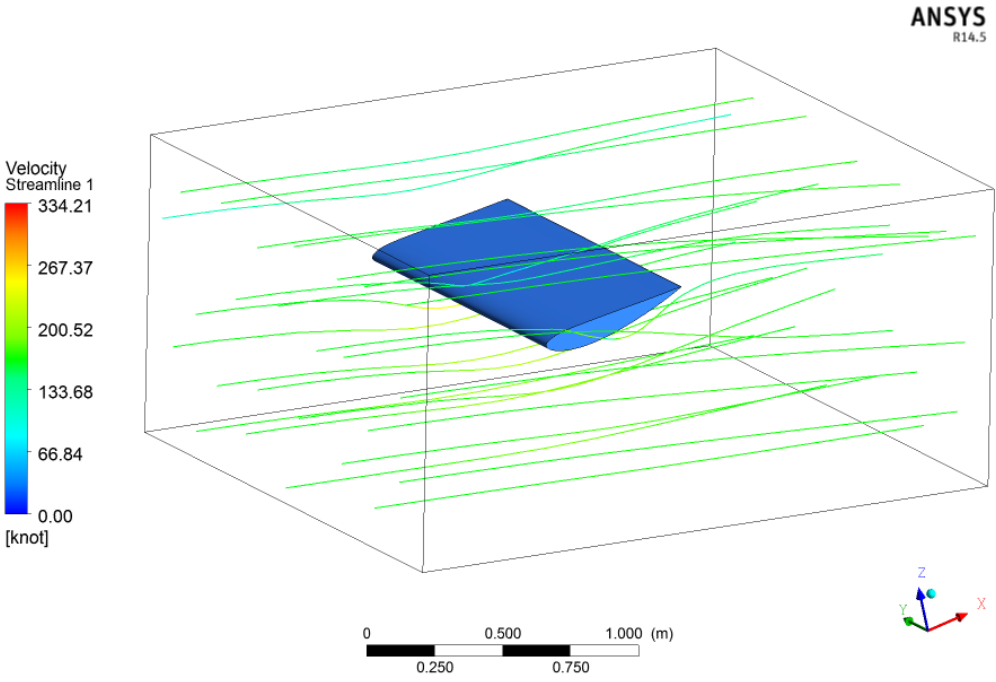


Figure 3.7: Velocity [knot] stream lines

3.3. Interpolation of the Aerodynamic Forces from CFD Mesh to the FE Mesh

Mesh that is created for the CFD analysis is very dense when compared to the FE mesh that is used for the structural analysis. Hence, pressure calculated by the CFD analysis should be interpolated to the FE mesh. In PATRAN, calculated pressure can be interpolated to the FE mesh.

First, CFD pressure data should be imported to PATRAN. Figures 3.8 and 3.9 present the pressure distributions in the Patran environment. If imported pressure data plots are compared to ANSYS plots, it can be seen that they are very close to each other.

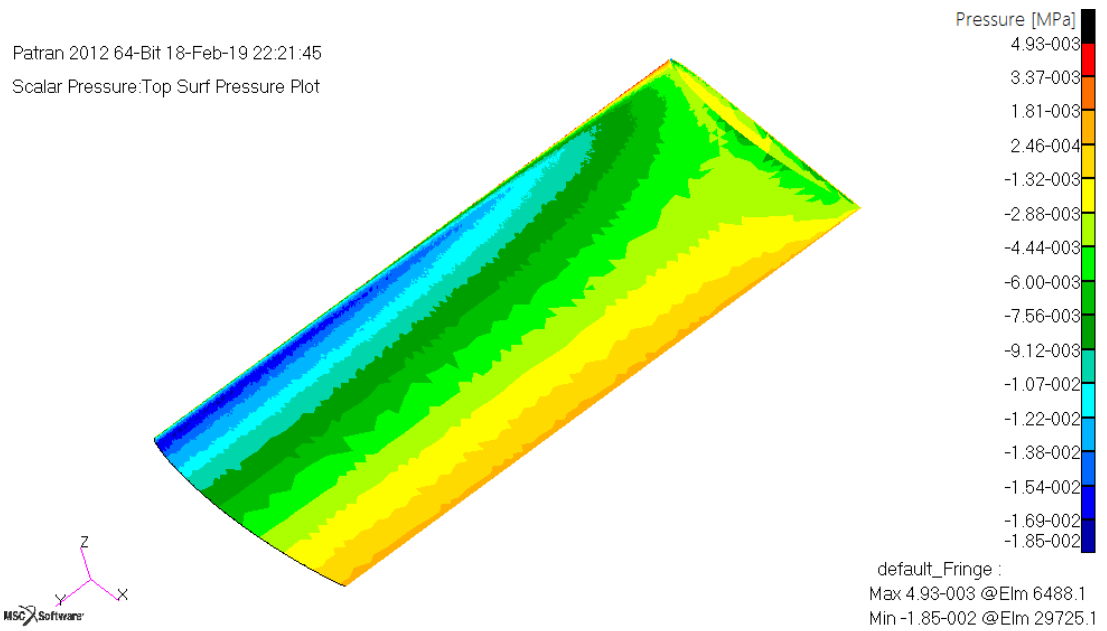


Figure 3.8: Imported pressure data [MPa] in Patran environment (lower skin and wing tip)

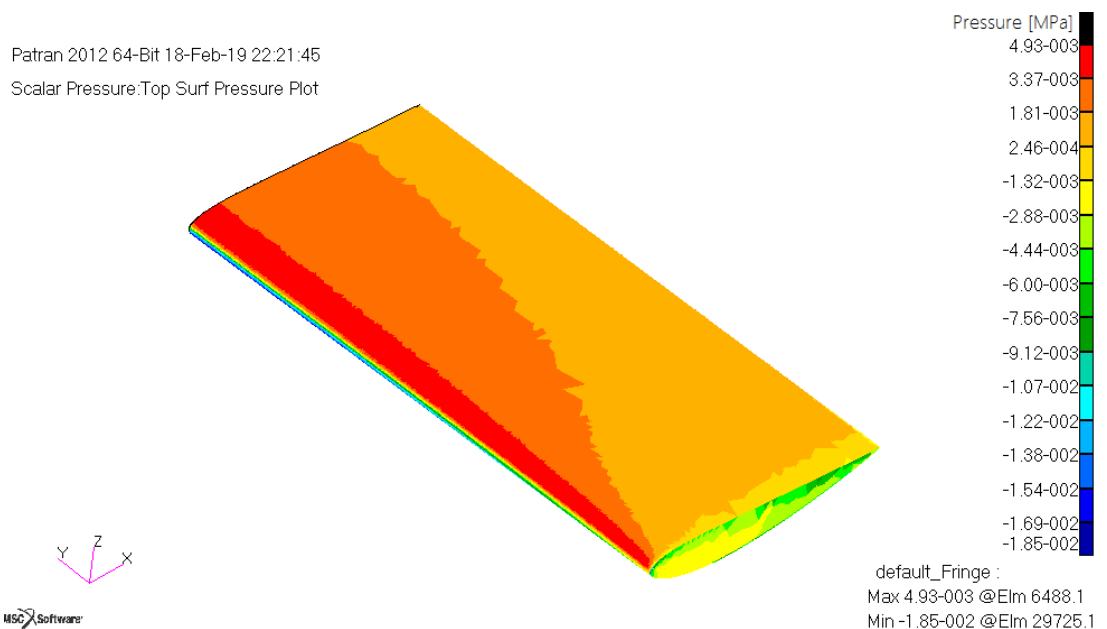


Figure 3.9: Imported pressure data [MPa] in Patran environment (upper skin and wing tip)

Then by creating spatial field using the imported pressure data, pressure distribution could be interpolated to the FE mesh. This interpolation is done for three different mesh densities that are created. Structural mesh sizes are very large when they compared with CFD mesh size as shown on Figure 3.10.

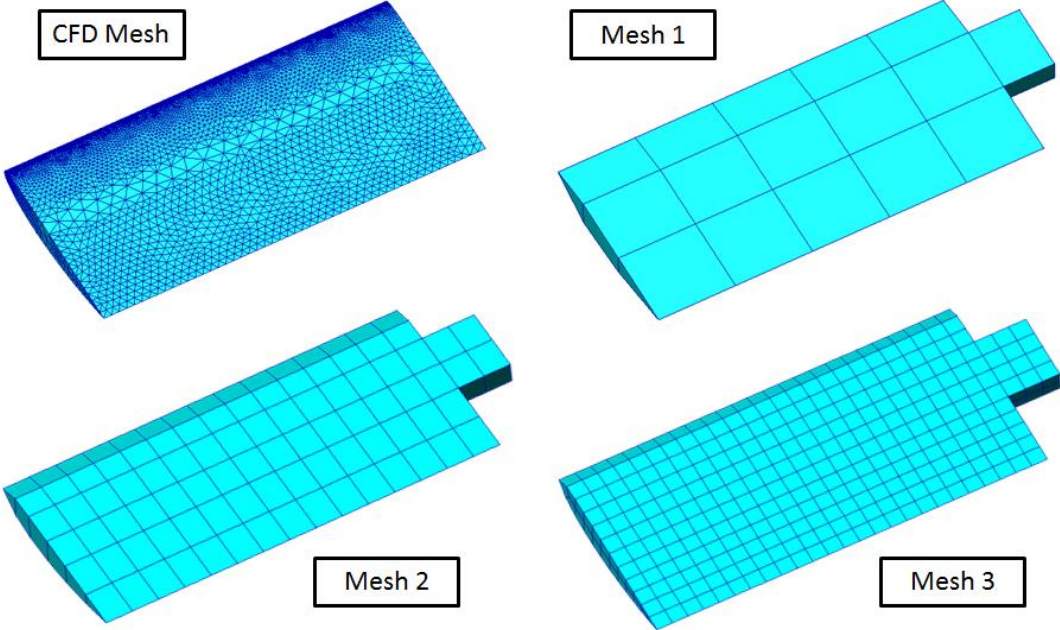


Figure 3.10: CFD Mesh density and three different mesh densities

In Figures 3.11-3.16, comparison of the CFD pressure distribution and the interpolated pressure distribution are given. In these figures, CFD pressure distribution is on the left and interpolated FE pressure distributions are on right.

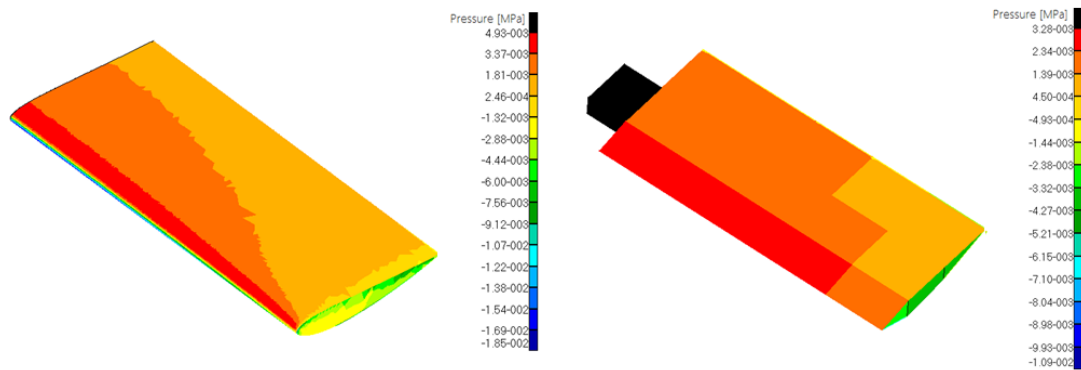


Figure 3.11: Comparison of the CFD pressure with the interpolated FE pressure on the Mesh 1 for upper skin

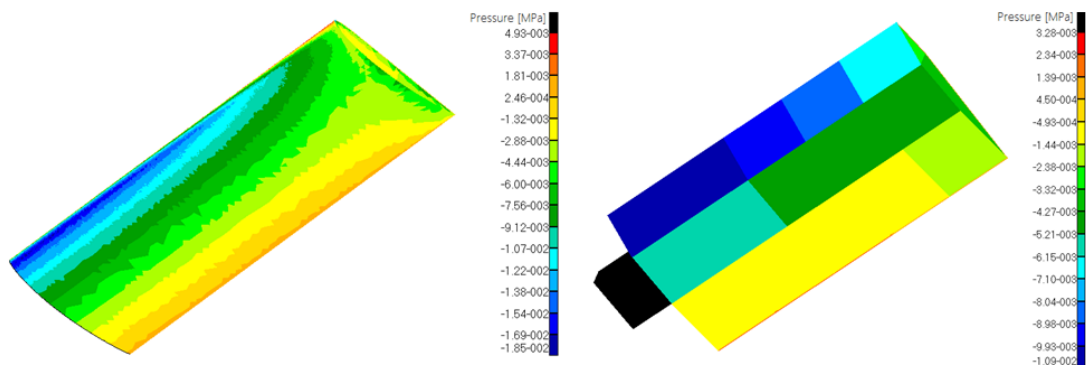


Figure 3.12: Comparison of the CFD pressure with the interpolated FE pressure on the Mesh 1 for lower skin

On the Mesh 1 density, structural mesh size is the largest one when compared with others as the Figure 3.10 shows. For a FE mesh, average pressure is calculated from CFD meshes on that mesh region. For this reason, maximum and minimum pressure values are not same with CFD pressures. Thus, spectrum ranges are not same on Figure 3.11 and 3.12.

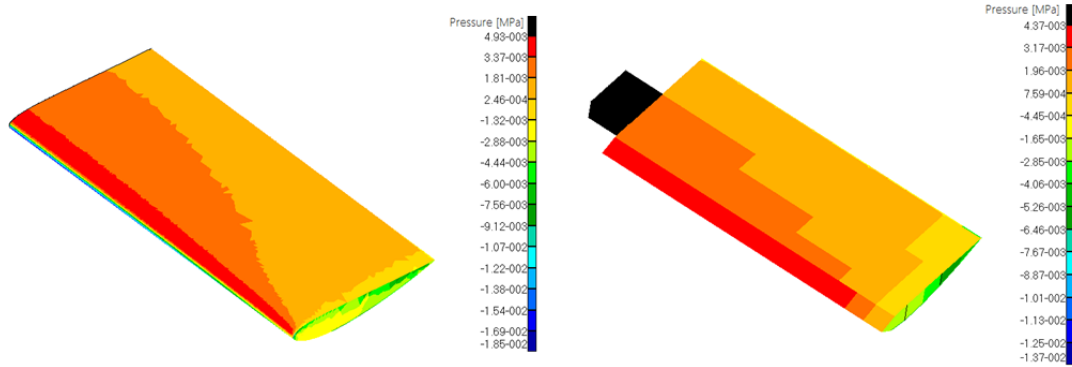


Figure 3.13: Comparison of the CFD pressure with the interpolated FE pressure on the Mesh 2 for upper skin

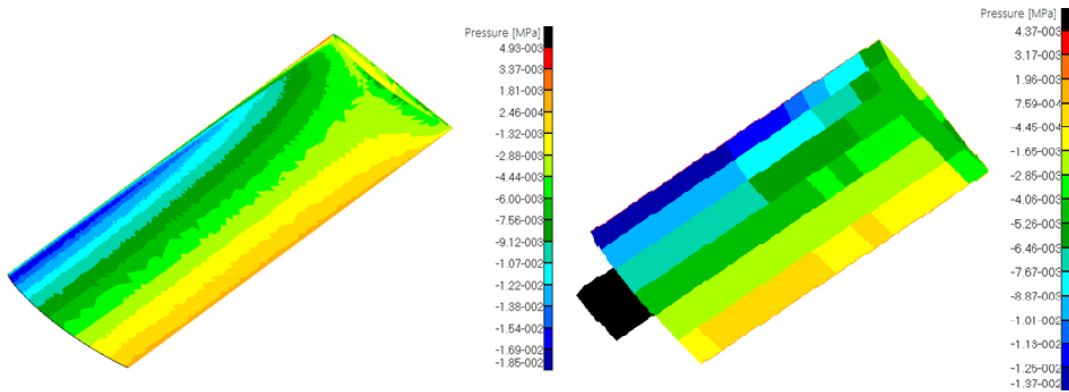


Figure 3.14: Comparison of the CFD pressure with the interpolated FE pressure on the Mesh 2 for lower skin

Mesh 2 pressure distribution is closer to CFD mesh pressure distribution than the Mesh 1 pressure distribution as shown in Figure 3.13 and 3.14. It can be seen that pressure spectrums are close to the pressure spectrums for the CFD pressure.

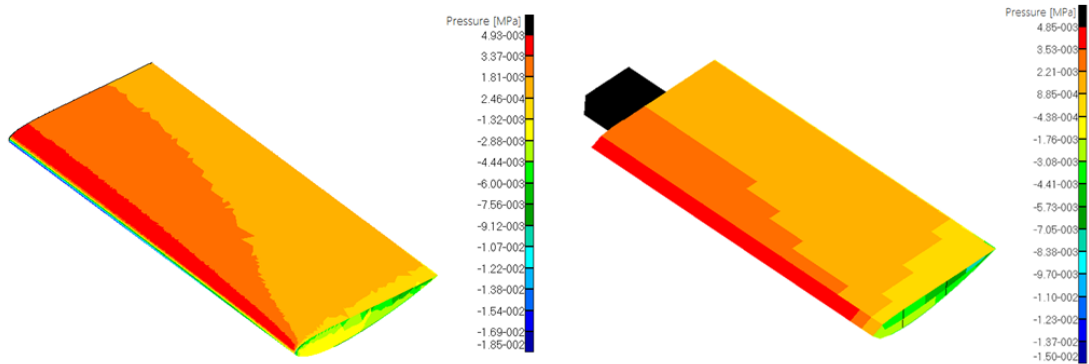


Figure 3.15: Comparison of the CFD pressure with the interpolated FE pressure on the Mesh 3 for upper skin

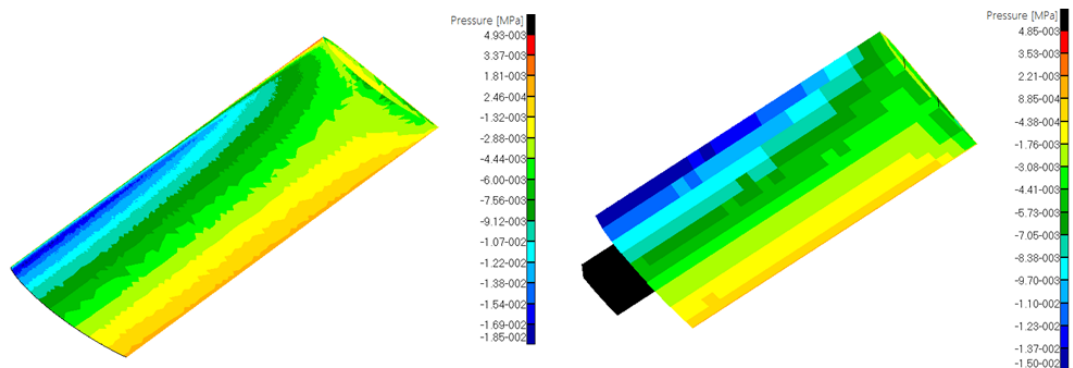


Figure 3.16: Comparison of the CFD pressure with the interpolated FE pressure on the Mesh 3 for lower skin

As the mesh density increases, maximum and minimum pressure values get closer to the maximum and minimum CFD pressure points. For the Mesh 3 case, Figure 3.15 and 3.16 show that pressure spectrums are much closer to the pressure spectrums for the CFD pressure. Therefore, it can be concluded that pressure distribution for the Mesh 3 density has a closer pressure distribution to the CFD pressure distribution.

As interpolated pressure distributions are not exactly same with CFD pressure distribution, constraint forces of interpolated pressures in lift direction of the

horizontal tail plane are investigated. In the Figures 3.17 to 3.19, constraint forces of interpolated pressures in lift direction (z direction) are shown to compare the efficiency of pressure interpolation of CFD mesh to FE meshes. As the total of constraints forces in z direction gives the total lift that is created, this comparison gives whether a convergence occurs with respect to mesh densities or not.

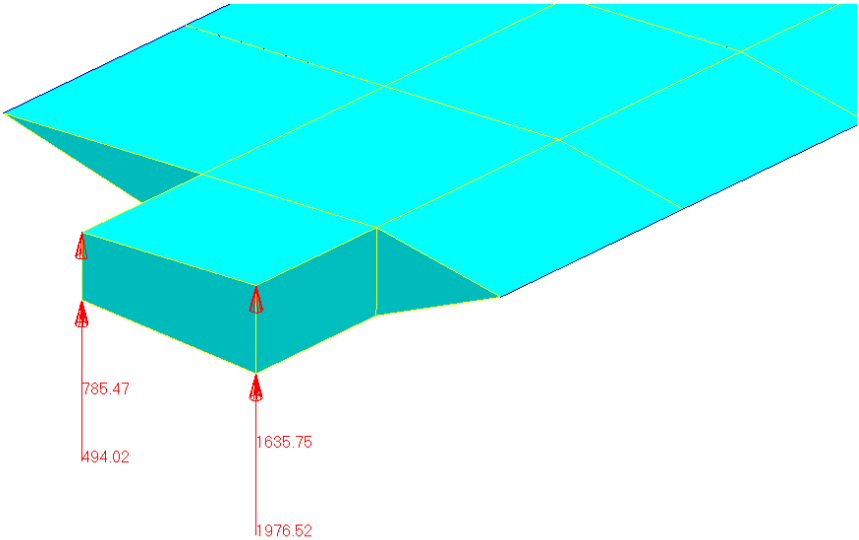


Figure 3.17: Constraint forces of interpolated pressure in lift direction on Mesh 1

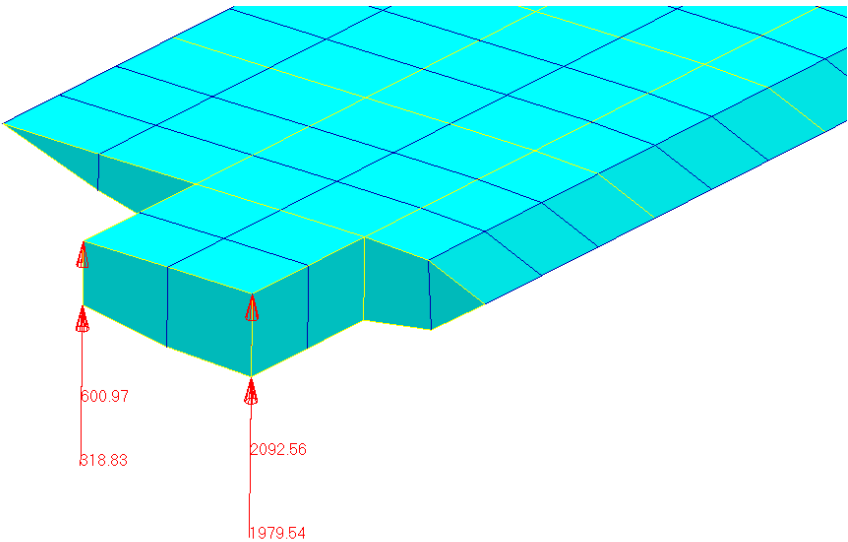


Figure 3.18: Constraint forces of interpolated pressure in lift direction on Mesh 2

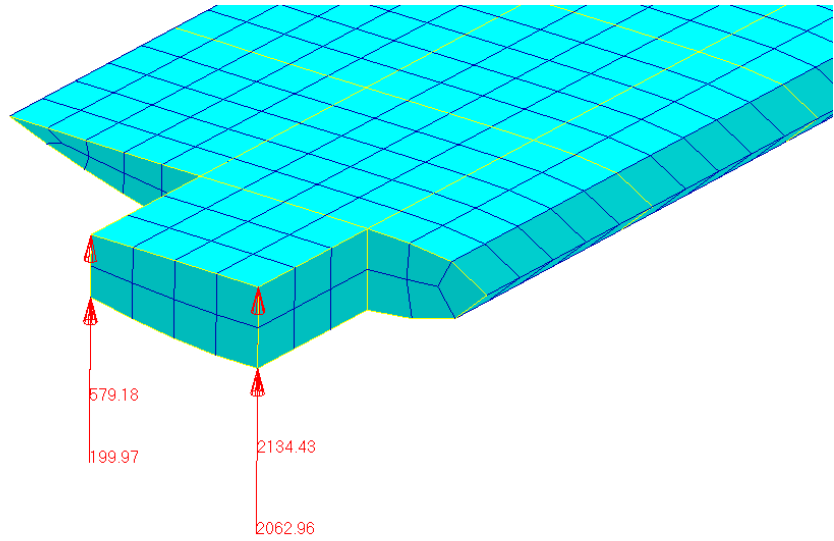


Figure 3.19: Constraint forces of interpolated pressure in lift direction on Mesh 3

In CFD mesh which has 40921 elements, total lift force is measured as 4978.256 N. In Mesh 1 density, which has 63 elements, total constraint force in lift direction is measured as 4891.76. In Mesh 2 density, which has 260 elements, total constraint force in lift direction is measured as 4991.9. In Mesh 3 density, which has 876 elements, total constraint force in lift direction is measured as 4976.54. According to data taken from Figures 3.17 – 3.19, Figure 3.20 compares element numbers vs. total lift forces of mesh densities.

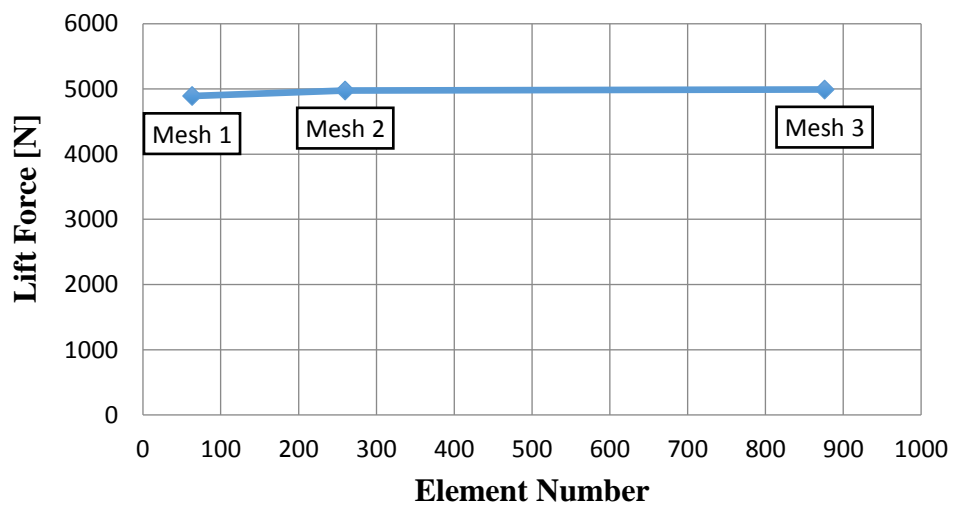


Figure 3.20: Total lift force vs. element numbers of Mesh 1, 2 and 3

According to Figure 3.20, it could be concluded that total lift forces are very close and they converge to the CFD lift force. Although the interpolated pressure spectrums for different FE mesh density results are different from the CFD mesh density pressure spectrum, the interpolated total lift forces are almost same. However, it is a fact that the interpolated pressure distribution is not exactly same in the finite element models with different mesh densities. Therefore, in Chapter 4.6, a subsection is added to investigate how the optimization results change when exactly the same load is applied to three different mesh densities. For this purpose, a distributed line load, which is equal to the total CFD lift force, is applied to the front spar of the finite element models with different mesh densities.

In addition to comparison of constraint forces of interpolated pressures in lift direction, by a static finite element analysis, tip displacements of three different mesh densities are also investigated with using aluminum materials and middle initial values that would be explained in Chapter 4, with applying calculated interpolated pressures, and with using boundary conditions that is shown in Figure 2.9. By doing so, it was evaluated that whether any tip displacement convergence occurs when mesh density increased. In the Figures 3.21 to 3.23, translational displacement results are shown for Mesh 1, 2 and 3 respectively.

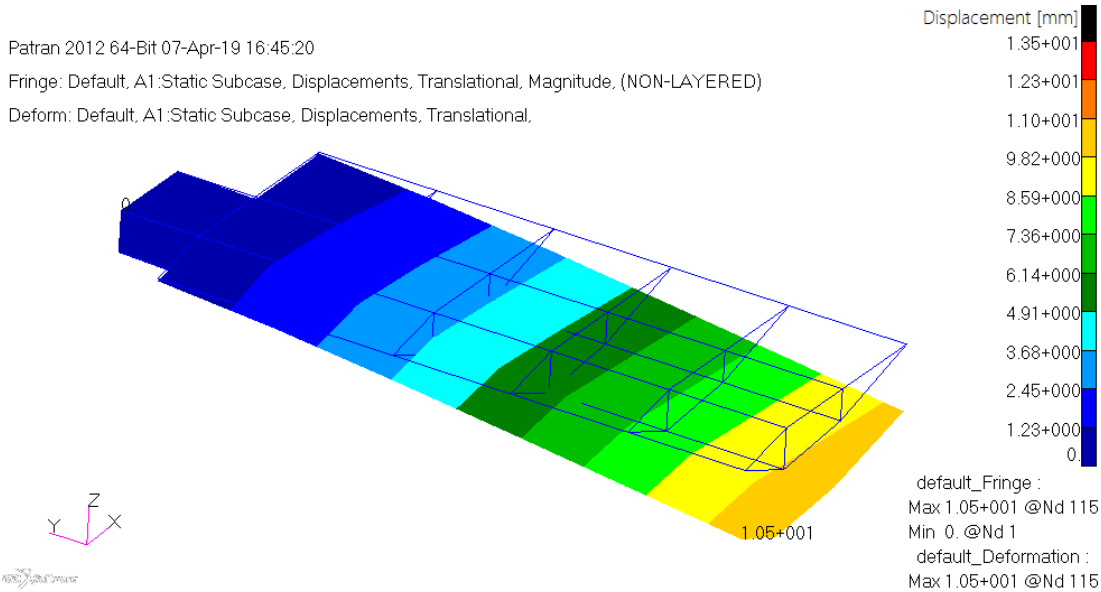


Figure 3.21: Displacement result for Mesh 1

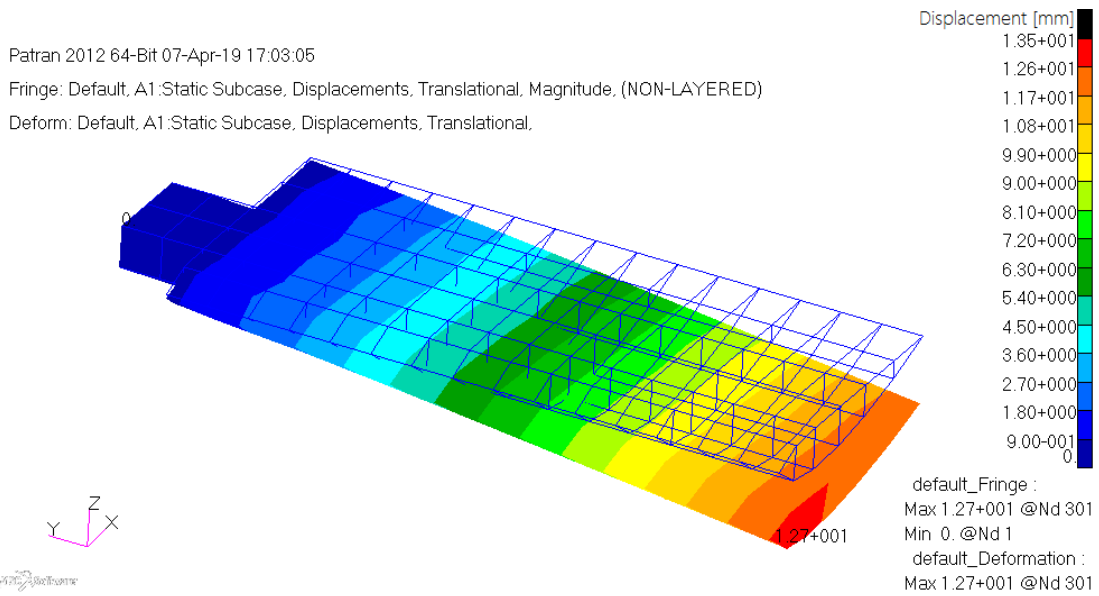


Figure 3.22: Displacement result for Mesh 2

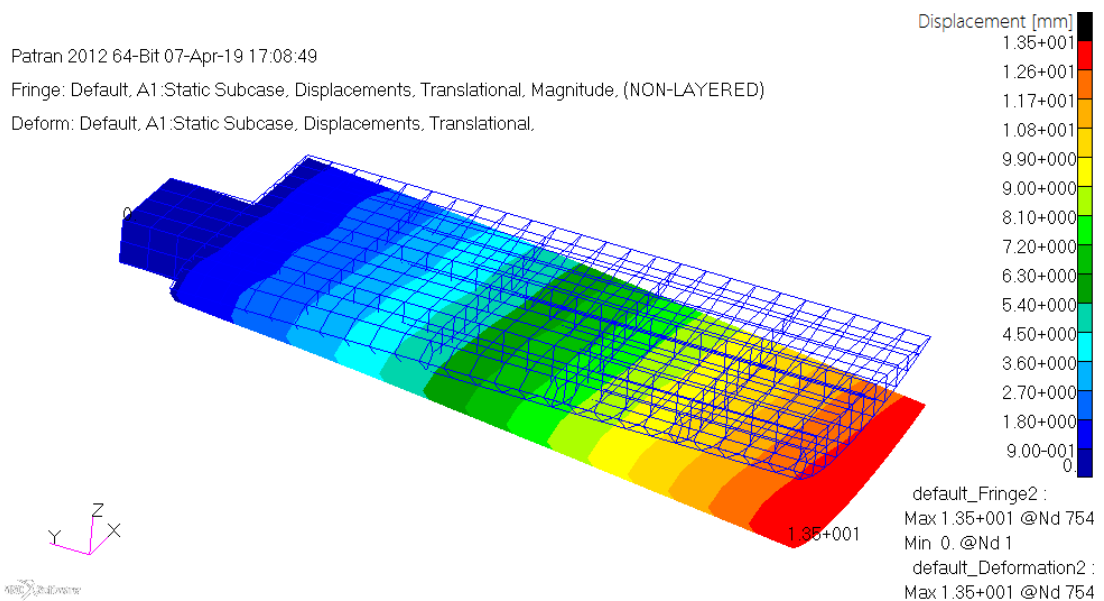


Figure 3.23: Displacement result for Mesh 3

According to Figures 3.21 – 3.23, tip displacements are 10.7 mm, 12.7 mm and 13.5 mm for Mesh 1, 2 and 3 respectively. Figure 3.24 compares the tip displacements with respect to element numbers of mesh densities.

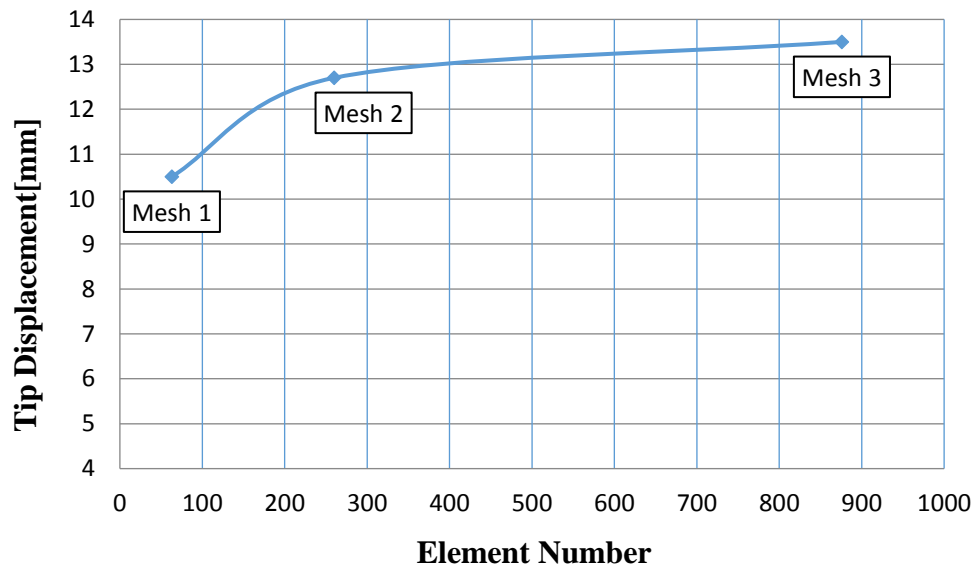


Figure 3.24: Displacement vs. element numbers of Mesh 1, 2 and 3

According to Figure 3.24, a convergence in displacements could be seen when mesh density is increased. This finding proves that interpolated pressure application and these three different mesh densities are fairly enough in optimizations for mesh density comparison.

CHAPTER 4

OPTIMIZATION OF THE ALUMINUM HTP

4.1. Introduction

In this chapter, material properties that are used for aluminum HTP structure are given. Then, optimization process of the aluminum HTP is explained in detail. Optimization results obtained are presented using graphs and tables.

4.2. Material Properties

In the aluminum optimization process, materials which are frequently used in aerospace industry are investigated, and also TAI's production and supply capabilities are taken into account. For every component, proper materials are selected. Spars may have different thicknesses in every region and they could be produced with a CNC machine properly. Hence, aluminum 7050 T7451 is selected because this plate type material is a proper material for a CNC machine and a frequently used material in TAI. In addition, root rib is in a critical position and has the same material as the spars. Figure 4.1 shows the spars and the root rib which are made of aluminum 7050 T7451 plate material.

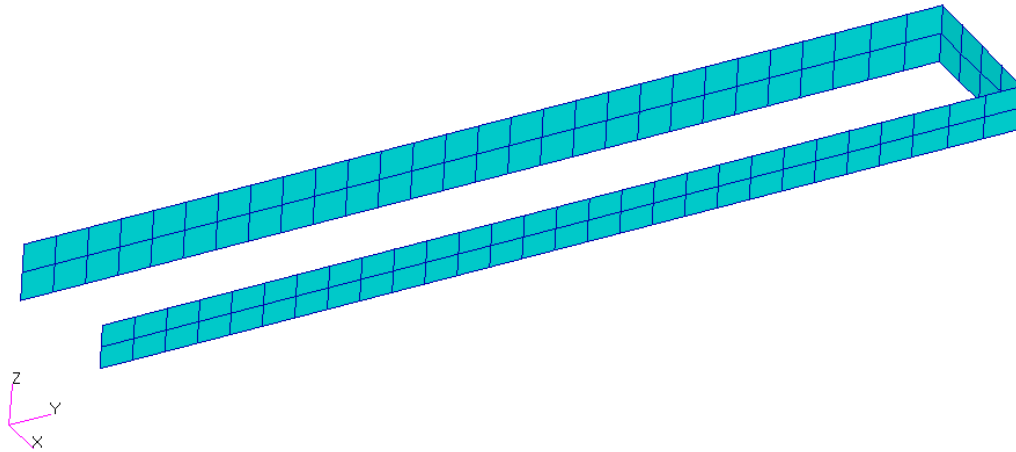


Figure 4.1: Spars and root rib which are made of 7050 T7451 aluminum plate material

Ribs need to be hydro pressed as they form the wing's airfoil shape. Because of that, aluminum 2024 T42 sheet plate material is selected as this material is most used material in TAI for hydro pressed parts. They are formed under water condition, because hydro press could only be applied in that condition, and then heat treatment process should be applied to strengthen the material. Figure 4.2 shows the ribs which are made of aluminum 2024 T42 sheet plate.

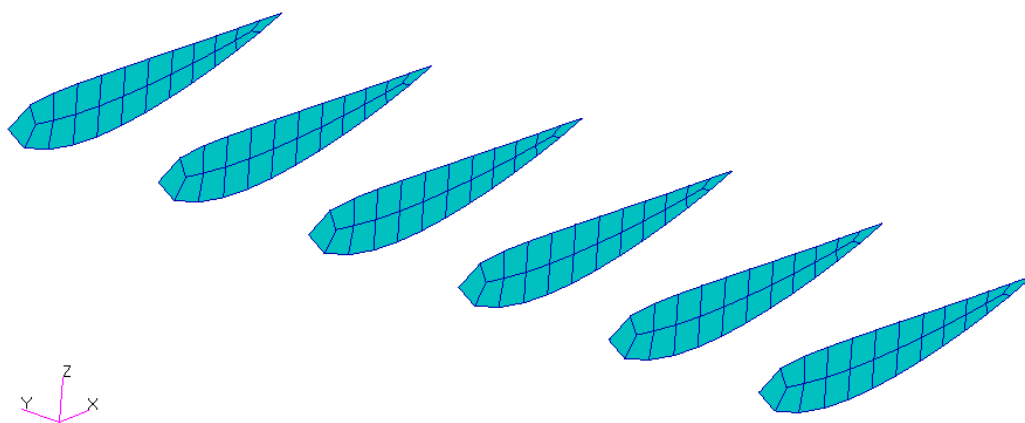


Figure 4.2: Ribs which are made of aluminum 2024 T42 sheet plate

Skins are made of aluminum 2024 T3 sheet plate material as they do not need to be hydro pressed. They can be formed with T3 material finish, and because of that, no heat treatment is required. Figure 4.3 shows the skins which are made of aluminum 2024 T3 sheet plate.

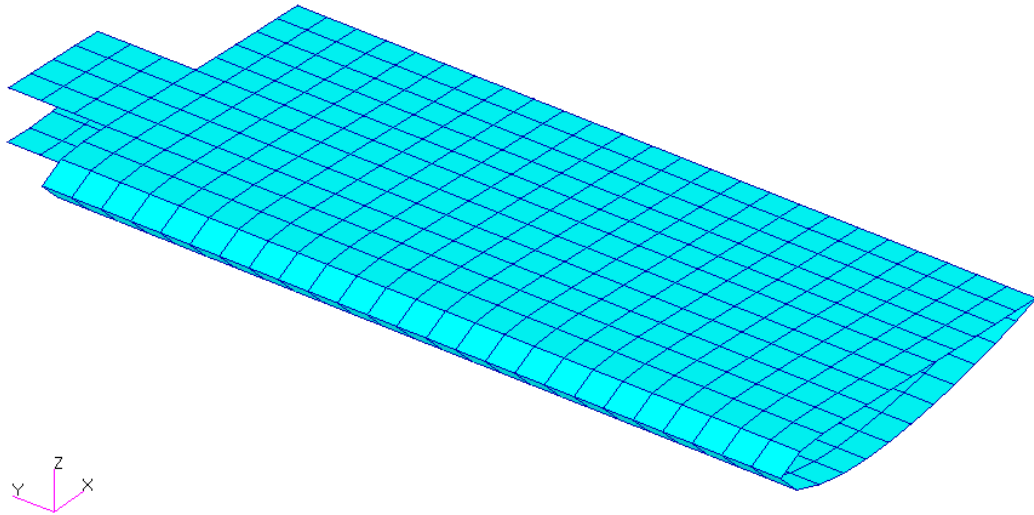


Figure 4.3: Skins which are made of 2024 T3 sheet plate aluminum material.

All material properties that are used in aluminum optimization are tabulated in Table 4.1.

Table 4.1: Material properties and strengths used in the aluminum HTP optimization [22]

	Al 2024 T42	Al 7050 T7451	Al 2024 T3
Modulus of Elasticity, E	73773 N/mm ²	73084 N/mm ²	73773 N/mm ²
Poisson's Ratio, ν	0.33	0.33	0.33
Tensile Ultimate Strength, F_{tu}	427 N/mm ²	524 N/mm ²	434 N/mm ²
Tensile Yield Strength, F_{ty}	262 N/mm ²	455 N/mm ²	324 N/mm ²
Compressive Yield Strength, F_{cy}	290 N/mm ²	441 N/mm ²	269 N/mm ²
Ultimate Shear Strength, F_{su}	255 N/mm ²	310 N/mm ²	276 N/mm ²

4.3. FE Model Properties

All surface regions are modeled by 2D shell elements, and all different flange regions are modeled by 1D rod elements. For skins, there are no flanges; flanges are modeled for spars and ribs. In Figure 4.4, yellow lines are 1D rod elements and blue surfaces are 2D shell elements. To show the 1D rods properly, skins are removed in Figure 4.4.

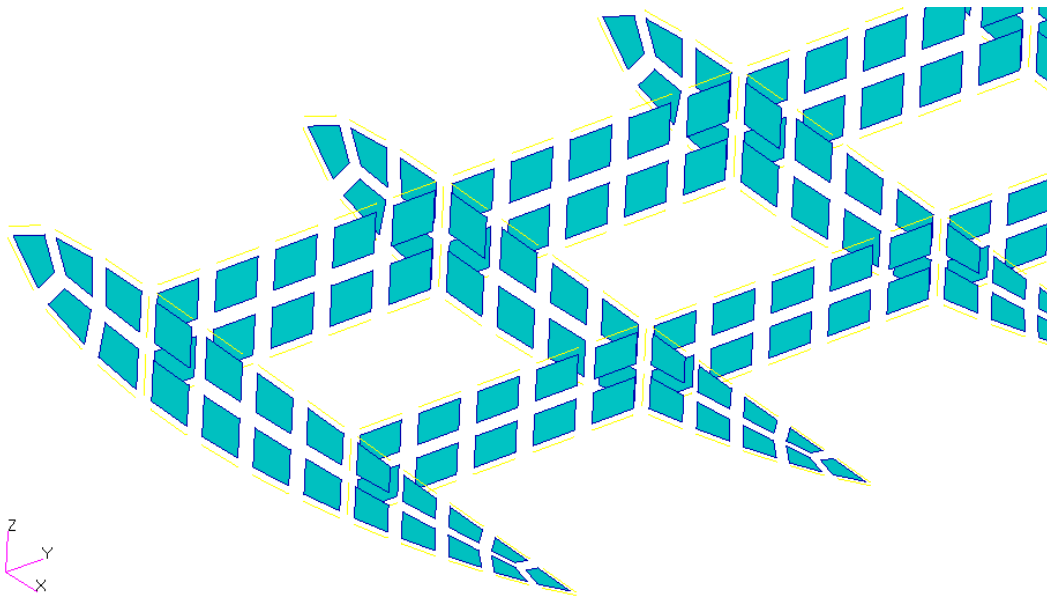


Figure 4.4: 1D rod elements (yellow lines) and 2D shell elements (blue surfaces)

4.4. Formulation of the Optimization Problem for the Aluminum HTP

4.4.1. Design Variables

In the aluminum optimization, skin and web thicknesses, and flange areas are design variables for every design region. There are 63 thicknesses, and 31 flange areas as design variables. Thickness variables are implemented as 2D shell thickness, and area variables are implemented as 1D rod areas. Flanges that are related to web surfaces are assumed as one design variable and they have the same area. In detail, there are 16 skin thicknesses for the upper skin, as shown in Figure 4.5.

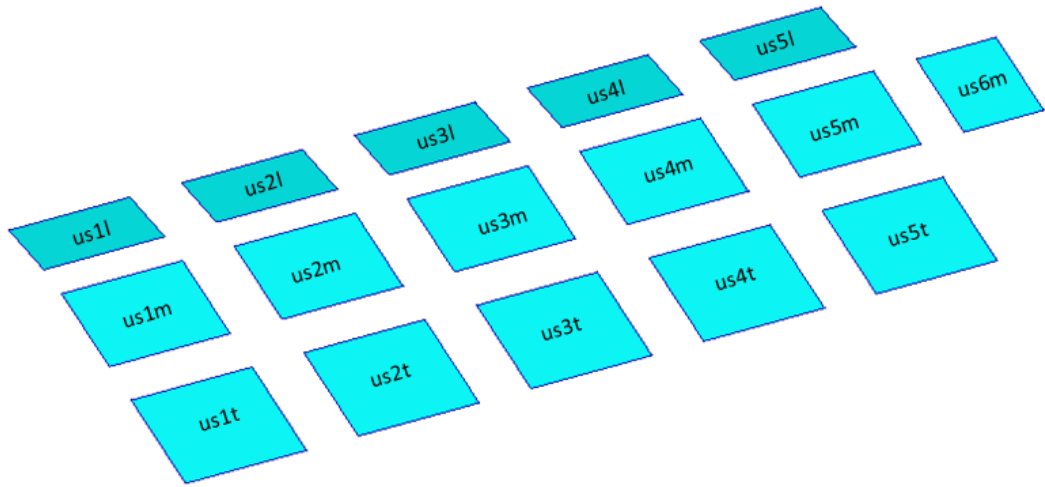


Figure 4.5: Upper skin design variables and variable names

Similarly, for the lower skin, there are 16 skin thicknesses defined as design variables. Figure 4.6 shows the lower skin variables and variable names.

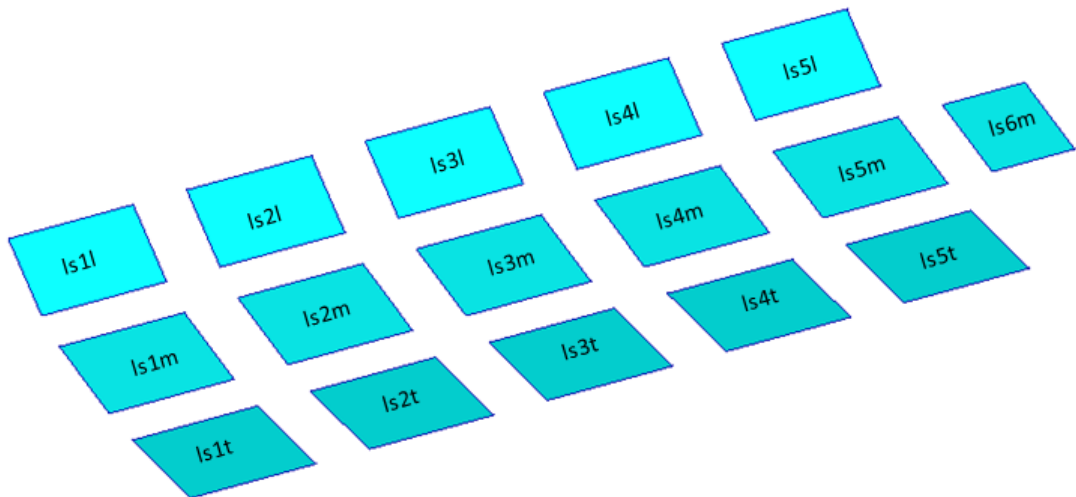


Figure 4.6: Lower skin design variables and variable names

Figure 4.7 shows the design variables defined for the rib. In total, there are 19 web thicknesses and 19 flange areas defined as design variables.

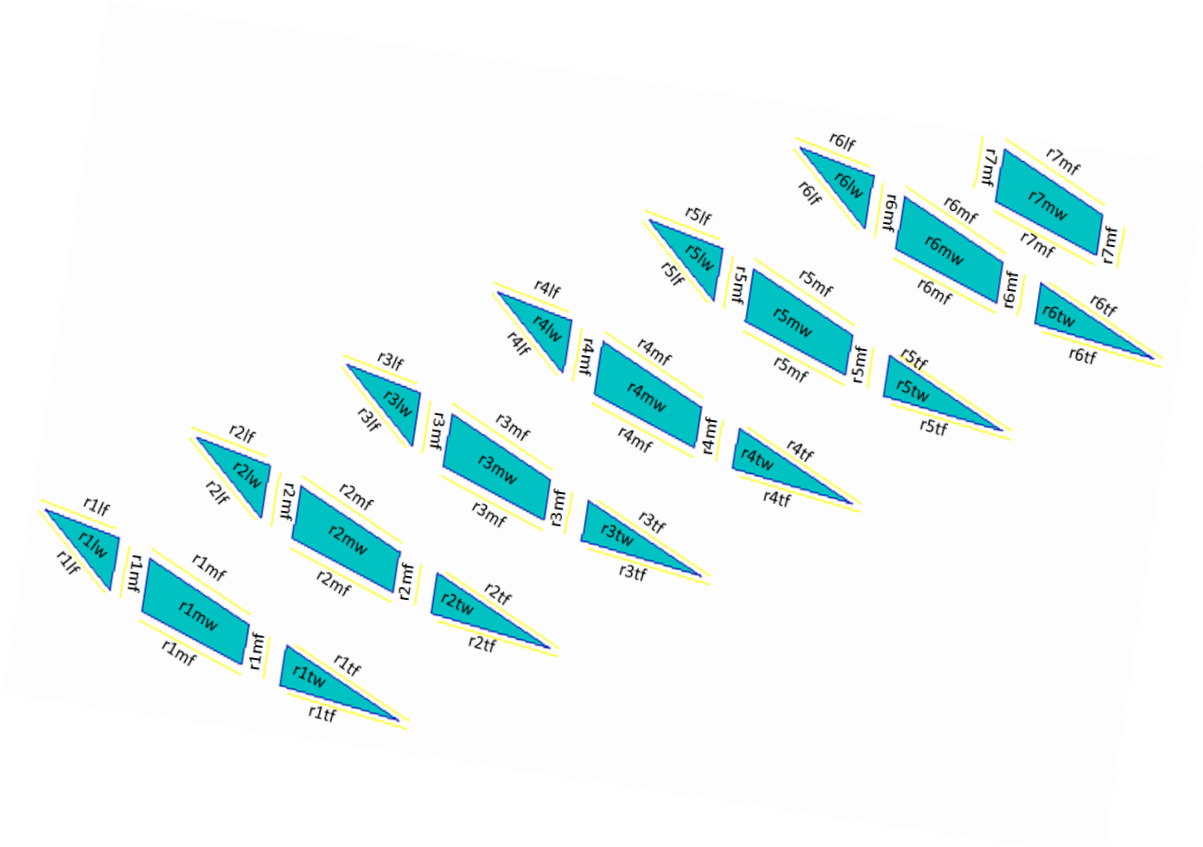


Figure 4.7: Rib design variables and variable names

Figure 4.8 shows the design variables defined for the spars. In total, there are 12 web thicknesses and 12 flange areas defined as design variables.

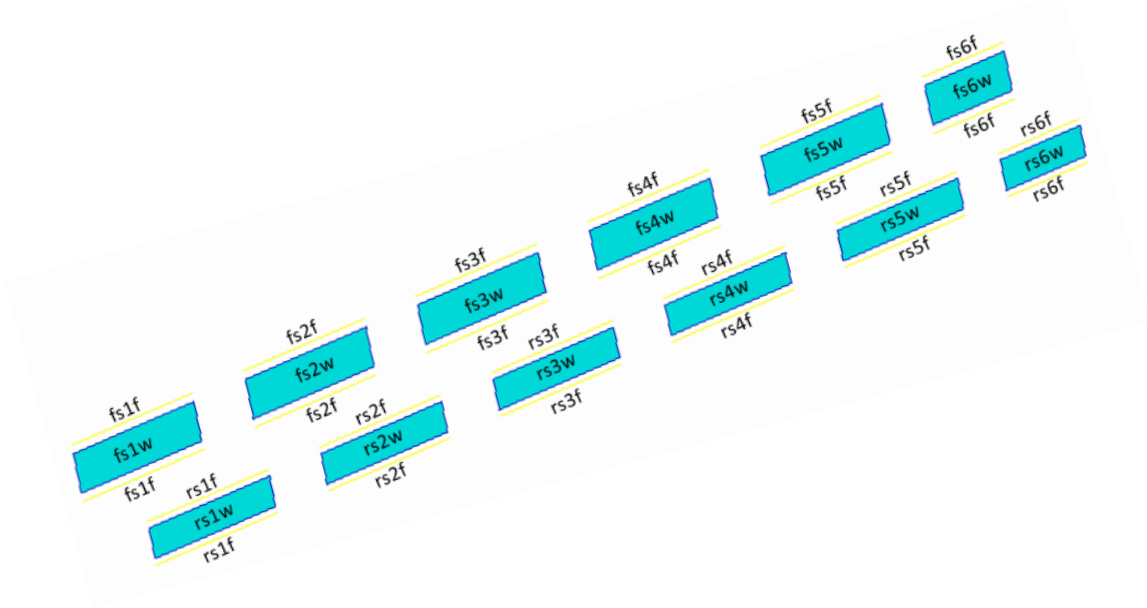


Figure 4.8: Spar design variables and variable names

To sum up, design variables are tabulated as shown in Table 4.2.

Table 4.2: Design variables defined for the aluminum HTP optimization

	Thickness	Flange Area
Upper Skin	16	-
Lower Skin	16	-
Leading Edge Ribs	6	6
Center Ribs	7	7
Trailing Edge Ribs	6	6
Front Spar	6	6
Rear Spar	6	6
Total	63	31

4.4.1.1. Discrete Design Variables

NASTRAN uses continuous design variables as default. However, this approach is not appropriate for real life. In this work, stock sizes of sheet plates and flange areas are used for outputs by considering the manufacturability consideration. Minimum and maximum possible thickness values are searched for this study. Flange areas are calculated according to searched thicknesses and edge distances which are calculated assuming one rivet line connection. In one rivet line connection, all flanges have one rivet line as shown in Figure 4.9.

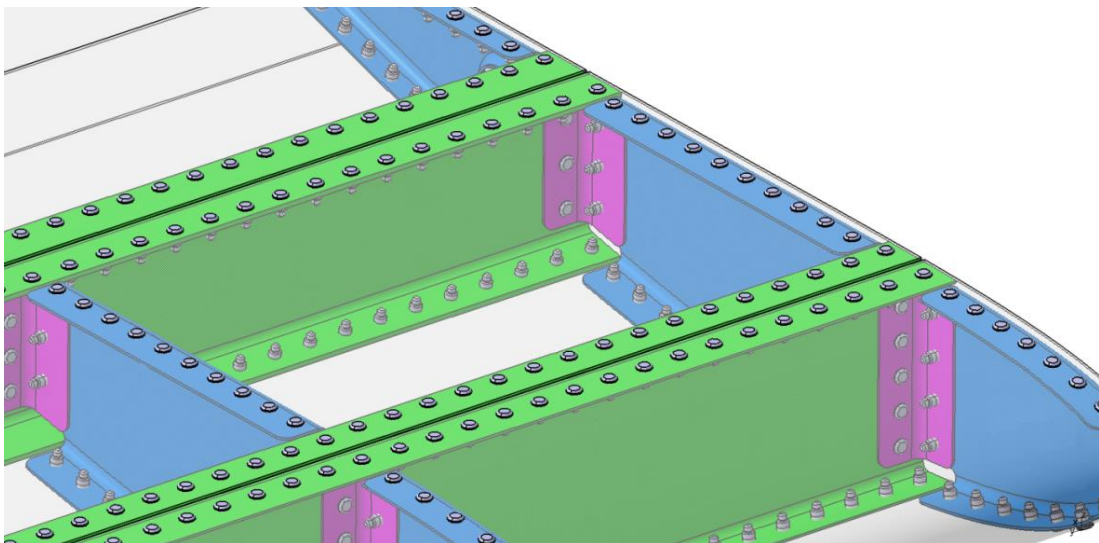


Figure 4.9: One rivet line connection example

Optimization results are rounded to the discrete values by using the NASTRAN DDVAL cards and the design of experiment (DOE) method. NASTRAN has round up and round off methods also. They are simple rounding operations that can be done by the user after continuous optimization results, and no new analysis required when one selects these two.

The DOE method makes use of the concept of orthogonal arrays (OA). After continuous optimization, a new discrete set that contains only the discrete variable values just above and just below the continuous variable can be selected. Thus, discrete design variable values are reduced to 2^n for a problem with n number of design variables. A full fractional array needs 2^n experiments for a problem with n two-level factors. Use of OA can dramatically reduce the required number of experiments as the number of parameters increases [23]. The implementation of DOE employed in MSC.NASTRAN employs an exhaustive search when n is 16 or less. Above 16, orthogonal array concept is employed to select candidate arrays that provide a representative sampling of the overall design space. Clearly, this is an approximation, but the thinking is that this will provide adequate coverage of the possible discrete solutions that it will not be far off from the “true” optimum that would be obtained from an exhaustive search [24].

Discrete values that are used are tabulated as shown in Table 4.3.

Table 4.3: Discrete design variable values for the aluminum HTP optimization

Thicknesses (mm)	0.41	0.51	0.64	0.81	0.91
	1.02	1.27	1.42	1.6	2.03
	2.54	3.56	4.06	4.57	4.83
Flange Areas (mm ²)	5.00	8.2	12.8	16.2	18.2
	20.4	25.4	28.4	32	40

It should be noted that discrete values are used only for skin thicknesses, rib web thicknesses and rib flange areas as they are manufactured from stock sized sheet plates. For spar web thicknesses and flange areas, still continuous design variables

are used because of machined material selection. Discrete and continuous design variables are tabulated in Table 4.4.

Table 4.4: Selection of discrete and continuous design variables

Discrete Design Variables	Skin Thicknesses
	Rib Web Thicknesses
	Rib Flange Areas
Continuous Design Variables	Spar Web Thicknesses
	Spar Flange Areas

4.4.1.2. Initial Values of the Design Variables

At the beginning of the optimization process, every design variable needs an initial value. In this study, minimum, middle and maximum initial values, within the lower and upper limits of the design variables, are used to analyze the effect of initial values of the design variables on the optimum result for every mesh density. Table 4.5 presents the minimum, middle and maximum initial values of the design variables.

Table 4.5: Minimum, middle and maximum input values of the design variables within the lower and upper limits of the design variables

	Minimum Value	Middle Value	Maximum Value
Spar Flange Areas	5 mm ²	42.5 mm ²	80 mm ²
Rib Flange Areas	5 mm ²	22.5 mm ²	40 mm ²
Spar Web Thicknesses Rib Web Thicknesses Skin Thicknesses	0.41 mm	2.62 mm	4.83 mm

It should be noted that the maximum value of the spar flange area, which is a continuous design variable, is taken as 80 mm² to give the freedom for an I-beam design. On the other hand, minimum spar flange area value is kept as 5 mm². If optimization yields a spar flange area that is below 40 mm² or close to 40 mm², C-beam design could be chosen in the detail design phase.

4.4.2. Constraints

For the aluminum optimization, constraints with regard to structural integrity are composed of strength and local buckling constraints. This work investigates two different constraint cases for the aluminum optimization; only strength constraints, and local buckling and strength constraints together. In addition to these two constraints, there is an extra geometric constraint created to reach the global optimum.

4.4.2.1. Strength Constraints

In this study, plastic deformation is not allowed. Hence, yield strength is used for the material allowable. When the optimization code reaches the optimum values for the design variables, it guarantees that the average stress value for every design region remains between the tension and the compression allowable stress of that material for the particular region. For spars, skins and ribs different stress constraints are given according to the loading type.

- For spar regions, constraints are given as;
 - Axial stress in the spar flanges must be between the tension and compression allowables. This axial stress is used also as captured average stress for lower flanges of spars in local in-plane bending buckling equations because lower flanges capture compression according to nature of the load case that is used in this study.

$$-F_{cy} < \sigma_{axial} < F_{ty} \quad (4.1)$$

- In the spar webs, von Mises stress, and normal y stress remain between the tension and the compression allowables, and shear stress is lower than the shear allowable of the material.

$$-F_{cy} < \sigma_{\text{von mises}} < F_{ty} \quad (4.2)$$

$$-F_{cy} < \sigma_{\text{normal y}} < F_{ty} \quad (4.3)$$

$$-F_{su} < \sigma_{\text{shear}} < F_{su} \quad (4.3)$$

Normal y stress is required to capture spar webs' tension and compression stresses because wing spars remain parallel to the y-axis as shown in Figure 4.10.

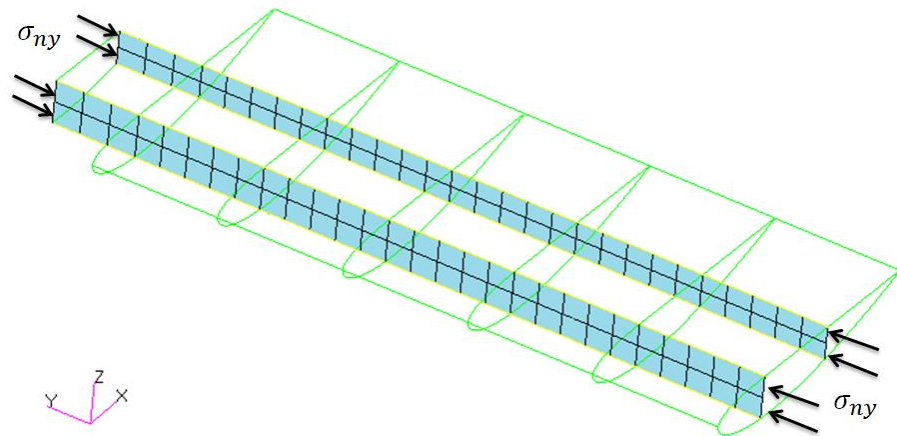


Figure 4.10: Normal y stresses on spars

- For the skin regions, von Mises stress, and normal y stress remain between the tension and the compression allowables, and the shear stress is lower than the shear allowable of the material.

$$-F_{cy} < \sigma_{\text{von misses}} < F_{ty} \quad (4.4)$$

$$-F_{cy} < \sigma_{\text{normal y}} < F_{ty} \quad (4.5)$$

$$-F_{su} < \sigma_{\text{shear}} < F_{su} \quad (4.6)$$

Same as the spar webs, skins need normal y stress to capture tension and compression stresses as shown in Figure 4.11. This normal y stress used also as captured average stress for skins in local compression buckling equations and shear stress is used as captured average stress for skins in local shear buckling equations.

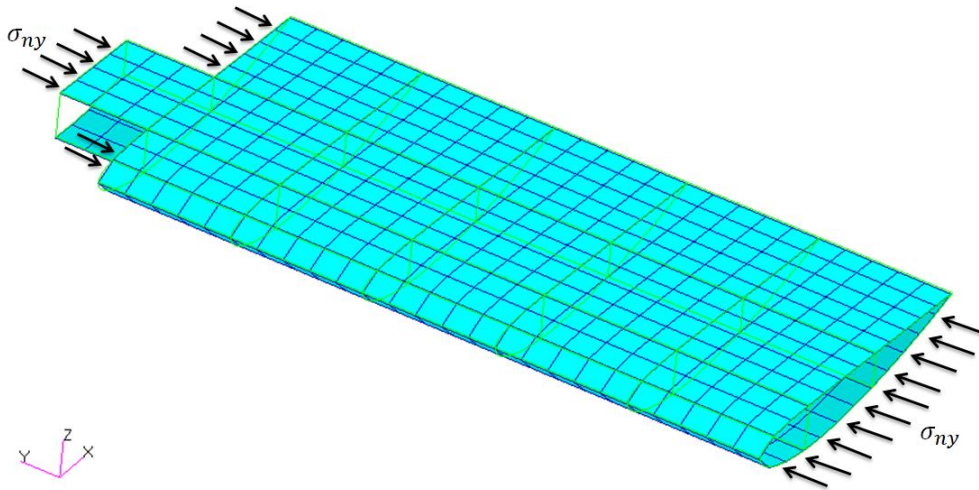


Figure 4.11: Normal y stresses on skins

- For rib regions, constrains are given as;
 - Axial stress in the rib flanges must be between the tension and compression allowables.

$$-F_{cy} < \sigma_{axial} < F_{ty} \quad (4.7)$$

- In the rib webs, von Mises stress remains between the tension and the compression allowables, and the shear stress is lower than the shear allowable of the material.

$$-F_{cy} < \sigma_{von\ misses} < F_{ty} \quad (4.8)$$

$$-F_{su} < \sigma_{shear} < F_{su} \quad (4.9)$$

These constraints are defined in the MSC.PATRAN environment since PATRAN allows users to define these constraints in its GUI.

4.4.2.2. Local Buckling Constraints

In aerospace structures, generally limited local buckling is allowed for the skins for exceptional load cases. If local buckling is not allowed, structures could become heavier than desired as these exceptional loads govern the dimensions. This optimization is done for the preliminary design phase and the load that is calculated is not an exceptional load case, hence local buckling is not allowed in this study.

Combined local buckling equations are used for every design region as design constraints. These constraints are written in NASTRAN input file as additional statements in a special format since MSC.PATRAN interface has no option for defining these constraints. For further information, addition of the local buckling constraints in NASTRAN input file is explained in APPENDIX B. For spars, skins and ribs different local buckling constraints are defined according to the loading type.

- Spar web regions are restricted with combined local shear and in-plane bending buckling equation as shown in Equation 4.10.

$$R_s^2 + R_b^2 \leq 1 \quad \Rightarrow \quad \left(\frac{\tau}{K_s E \left(\frac{t}{b}\right)^2} \right)^2 + \left(\frac{\sigma_{\text{comp}}}{K_b E \left(\frac{t}{b}\right)^2} \right)^2 \leq 1 \quad (4.10)$$

- For skin regions, combined local shear and compression buckling is restricted with using Equation 4.11 as shown.

$$R_s^2 + R_c \leq 1 \quad \Rightarrow \quad \left(\frac{\tau}{K_s E \left(\frac{t}{b}\right)^2} \right)^2 + \left(\frac{\sigma_{\text{comp}}}{K_c E \left(\frac{t}{b}\right)^2} \right)^2 \leq 1 \quad (4.11)$$

- For rib web regions, local shear buckling is not allowed and constraint equation is as shown in Equation 4.12.

$$R_s \leq 1 \quad \Rightarrow \quad \left(\frac{\tau}{K_s E \left(\frac{t}{b}\right)^2} \right) \leq 1 \quad (4.12)$$

In these equations, b is the shorter dimension of the plates for shear buckling as all edges carry shear; for compression and in-plane bending buckling b is the loaded edge of the plate. K is the buckling coefficient which depends on the boundary conditions and the sheet aspect ratio a/b . The calculation of the buckling coefficients is explained in Appendix C.

To sum up, all the constraints are as shown in Table 4.6

Table 4.6: All constraints applied for the aluminum HTP optimization

Regions		Strength	Buckling
Spars	Flanges	$-F_{cy} < \sigma_{axial} < F_{ty}$	
	Webs	$-F_{cy} < \sigma_{von\ misses} < F_{ty}$ $-F_{cy} < \sigma_{normal\ y} < F_{ty}$ $-F_{su} < \sigma_{shear} < F_{su}$	$R_s^2 + R_b^2 \leq 1$
Ribs	Flanges	$-F_{cy} < \sigma_{axial} < F_{ty}$	
	Webs	$-F_{cy} < \sigma_{von\ misses} < F_{ty}$ $-F_{su} < \sigma_{shear} < F_{su}$	$R_s \leq 1$
Skins		$-F_{cy} < \sigma_{von\ misses} < F_{ty}$ $-F_{cy} < \sigma_{normal\ y} < F_{ty}$ $-F_{su} < \sigma_{shear} < F_{su}$	$R_s^2 + R_c \leq 1$

4.4.2.3. Thickness Constraints

Because of the nature of gradient-based methods that is used by NASTRAN, optimization can stop at local optimums. As explained before, horizontal tail plane is fixed at the root of the wing, and the calculated aerodynamic load has higher pressures at the root region. From an engineering point of view, thickness and area

variables have to increase from tip to the root of the horizontal tail plane. Therefore, to end up with the expected thickness and area variations, geometric constraints are written in the NASTRAN input file as equations. For further information, these equations, which are written to the NASTRAN input file in NASTRAN format, are given and explained in APPENDIX B. Geometric constraints applied to design variables are shown in Figure 4.12 and tabulated in Table 4.7.

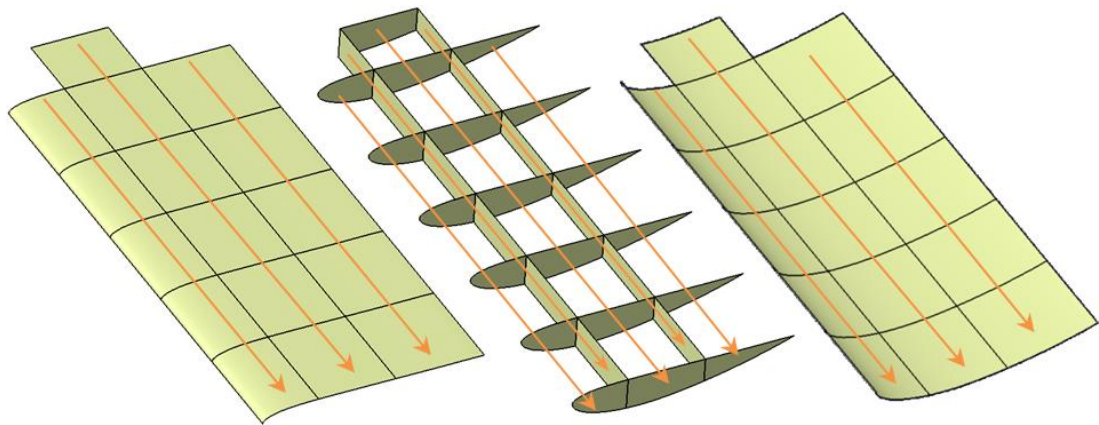


Figure 4.12: Thickness constraints

Table 4.7: Thickness constraints

Geometric Variable Zones	Root Variables > Tip Variables
Front Spar Flanges	$fs6f > fs5f > \dots > fs1f$
Rear Spar Flanges	$rs6f > rs5f > \dots > rs1f$
Middle Rib Flanges	$r7mf > r6mf > \dots > r1mf$
Leading Edge Rib Flanges	$r6lf > r5lf > \dots > r1lf$
Trailing Edge Rib Flanges	$r6tf > r5tf > \dots > r1tf$
Front Spar Webs	$fs6w > fs5w > \dots > fs1w$
Rear Spar Webs	$rs6w > rs5w > \dots > rs1w$
Middle Rib Webs	$r7mw > r6mw > \dots > r1mw$
Leading Edge Rib Webs	$r6lw > r5lw > \dots > r1lw$
Trailing Edge Rib Webs	$r6tw > r5tw > \dots > r1tw$
Middle Upper Skin	$us6m > us5m > \dots > us1m$
Leading Edge Upper Skin	$us5l > us4l > \dots > us1l$
Trailing Edge Upper Skin	$us5t > us4t > \dots > us1t$
Middle Lower Skin	$ls6m > ls5m > \dots > ls1m$
Leading Edge Lower Skin	$ls5l > ls4l > \dots > ls1l$
Trailing Edge Lower Skin	$ls5t > ls4t > \dots > ls1t$

4.4.3. Objective Function of the Optimization

The objective of the aluminum horizontal tail plane optimization problem is to reach the minimum structural weight. Hence, the objective function is the total mass of the horizontal tail. The mass of the horizontal tail is automatically calculated by MSC.NASTRAN and the design objective function is defined in the MSC.PATRAN GUI.

4.5. Optimization Results

In the aluminum horizontal tail optimization problem, three different mesh densities, three different design variable inputs, and two different constraints are considered. Optimization results can be continuous and discrete depending on the design variable. When continuous design variable optimization is done, every design variable is continuous; when discrete design variable optimization is mentioned, skin and rib design variables are discrete as they are stock sized sheet plates, spar design variables are still continuous as they are machined parts.

4.5.1. Optimization Using Continuous Design Variables

For the strength constraint only, according to the minimum, middle and the maximum initial values within the upper and lower limit of the design variables, continuous optimization iterations are shown in Figures 4.13 - 4.15 for the Mesh 1, Mesh 2 and the Mesh 3 densities, respectively.

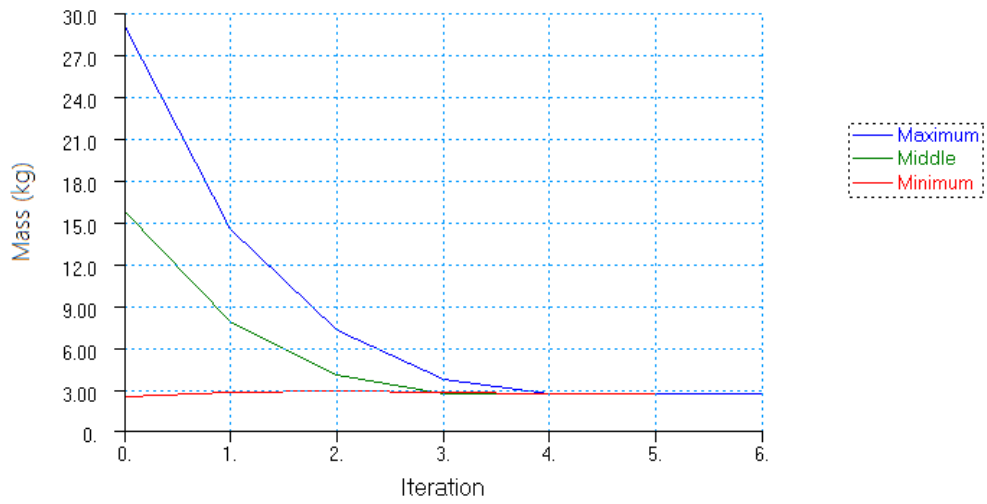


Figure 4.13: Continuous optimization iterations for the Mesh 1 / Three different initial values for design variables / Strength constraint only

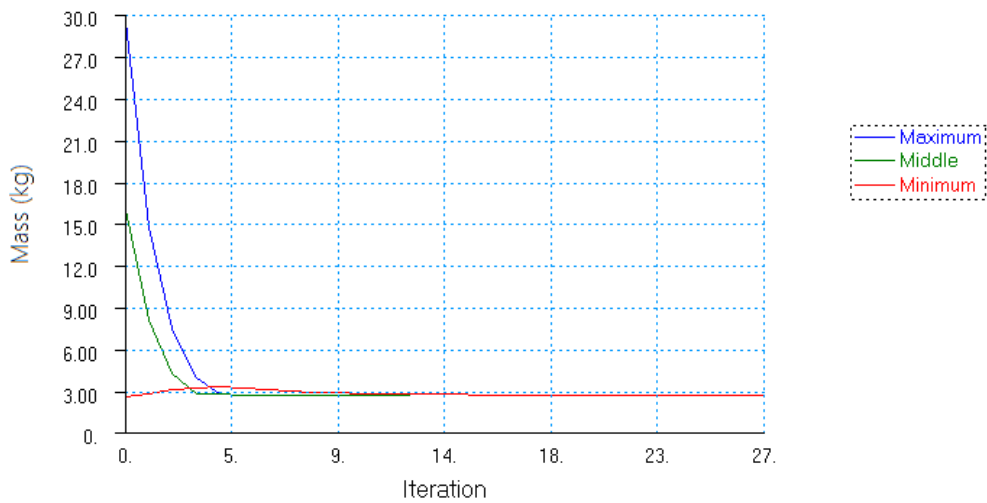


Figure 4.14: Continuous optimization iterations for the Mesh 2 / Three different initial values for design variables / Strength constraint only

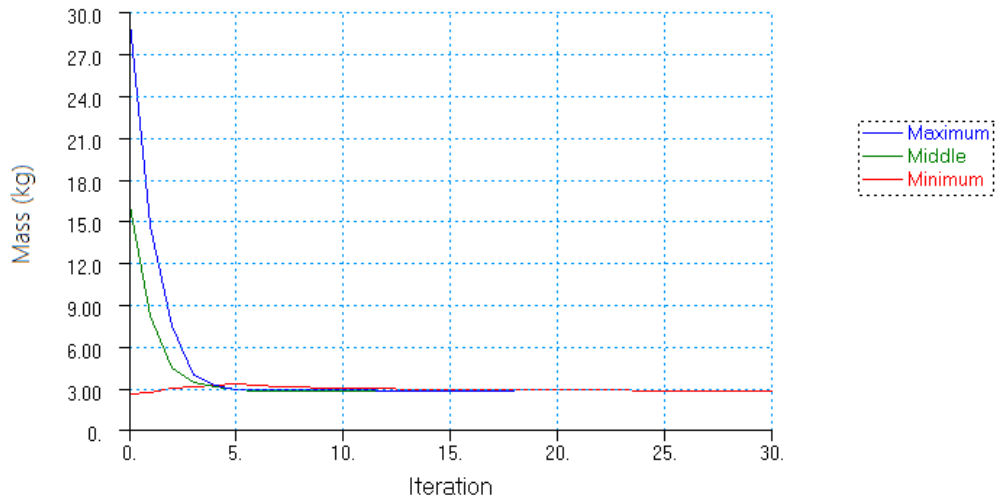


Figure 4.15: Continuous optimization iterations for the Mesh 3 / Three different initial values for design variables / Strength constraint only

For the strength constraint only, the calculated optimum masses of the horizontal tail plane are tabulated in Table 4.8 for the continuous design variable case.

Table 4.8: Optimization results for the strength constraint only using continuous design variables

Initial Values	Mesh 1	Mesh 2	Mesh 3
MINIMUM	2.63 kg	2.67 kg	2.78 kg
MIDDLE	2.63 kg	2.68 kg	2.78 kg
MAXIMUM	2.62 kg	2.68 kg	2.79 kg

For the strength constraint and local buckling constraints together, according to the minimum, middle and the maximum initial values within the upper and lower limit of the design variables, continuous optimization iterations are shown in Figures 4.16 - 4.18 for the Mesh 1, Mesh 2 and the Mesh 3 densities, respectively.

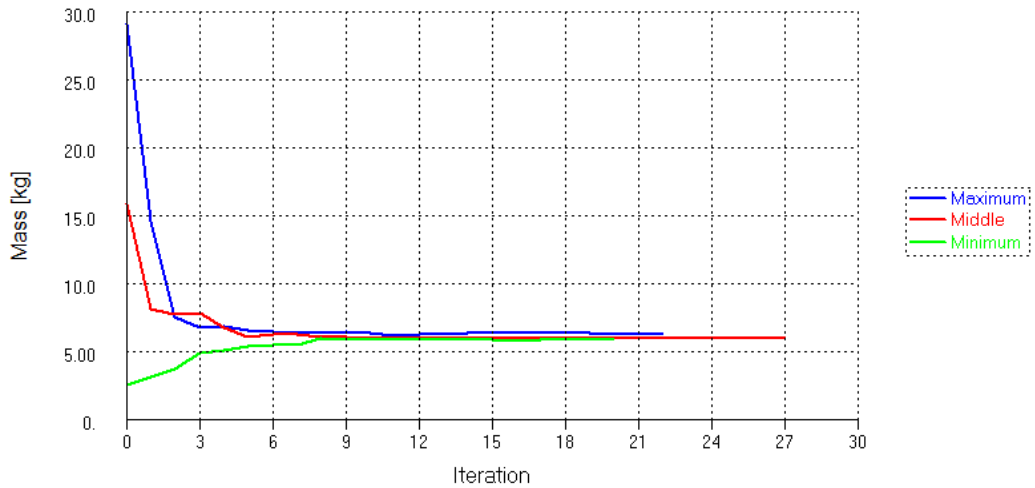


Figure 4.16: Continuous optimization iterations for the Mesh 1 / Three different initial values for design variables / Strength and local buckling constraints

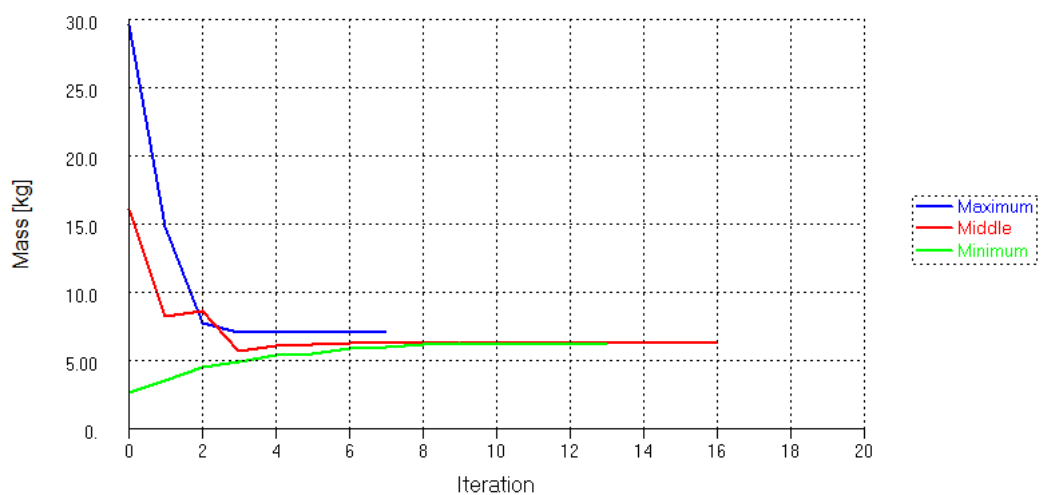


Figure 4.17: Continuous optimization iterations for the Mesh 2 / Three different initial values for design variables / Strength and local buckling constraints

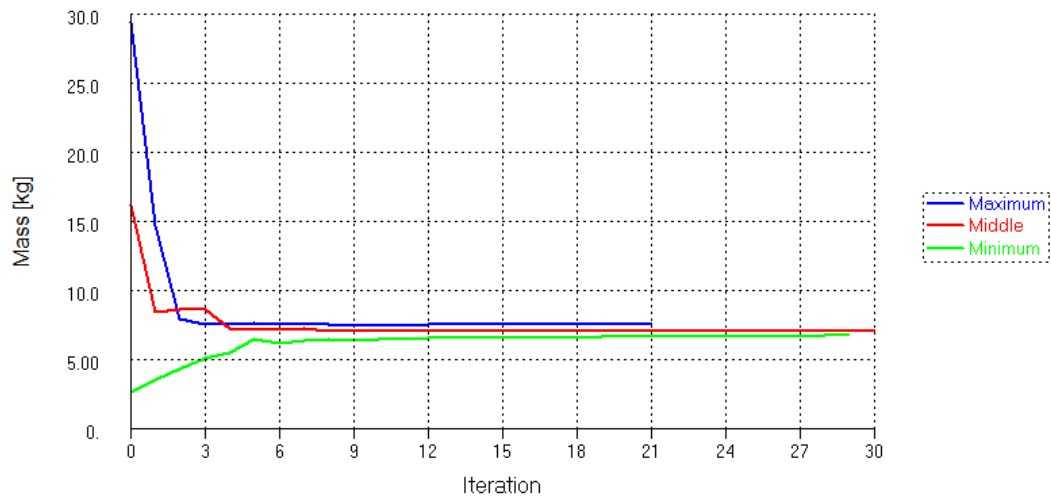


Figure 4.18: Continuous optimization iterations for the Mesh 3 / Three different initial values for design variables / Strength and local buckling constraints

For the strength constraint and local buckling constraints together, the calculated optimum masses of the horizontal tail plane are tabulated in Table 4.9 for the continuous design variable case.

Table 4.9: Optimization results for the combined strength and local buckling constraints using continuous design variables

Initial Values	Mesh 1	Mesh 2	Mesh 3
MINIMUM	5.81 kg	6.16 kg	6.67 kg
MIDDLE	5.94 kg	6.25 kg	6.98 kg
MAXIMUM	6.26 kg	6.96 kg	7.46 kg

This initial study has shown that the effect of the local buckling constraint on the total weight of the horizontal tail plane is more than the effect of the strength constraint. In tail structures like wings, skin buckling constraints mainly govern the skin thicknesses, especially those on the compression side, and the current study has also confirmed this. Moreover, as mesh density increases, mass values obtained from optimizations increase. This also makes sense, because finer mesh catches the stress gradients better and consequentially mass values obtained from optimizations increase. The effect of the initial values of the design variables on the optimum mass is insignificant when strength constraints are used only. It can be said that for the strength constraint case only, global optimum has been reached. However, for the combined strength and local buckling constraint case, as Table 4.9 shows, when the initial values of the design variables are selected near the upper limit of the design variables, slightly higher mass values are obtained. Hence, it can be commented that to be sure about the global optimum additional optimization analyses have to be conducted using different initial values. However, the lightest optimization result for each mesh density can be selected as the optimum mass considering that the differences between the optimization results for different initial values are small.

4.5.2. Optimization Using Discrete Design Variables

Discrete design variable gives more realistic results as sheet plates have restricted stock sizes. However, machined parts do not have stock sizes; they could be machined according to CNC machines' capabilities. Therefore, in discrete design variable optimization part, only skin and rib variables are chosen as discrete design variables; spar variables are still continuous design variables as shown on Table 4.4.

In this case, only the combined strength and local buckling constraints are applied in the optimization. For the strength constraint and local buckling constraints together, according to the minimum, middle and the maximum initial values within the upper and lower limit of the design variables, discrete optimization iterations are shown in Figures 4.19 - 4.21 for the Mesh 1, Mesh 2 and the Mesh 3 densities, respectively.

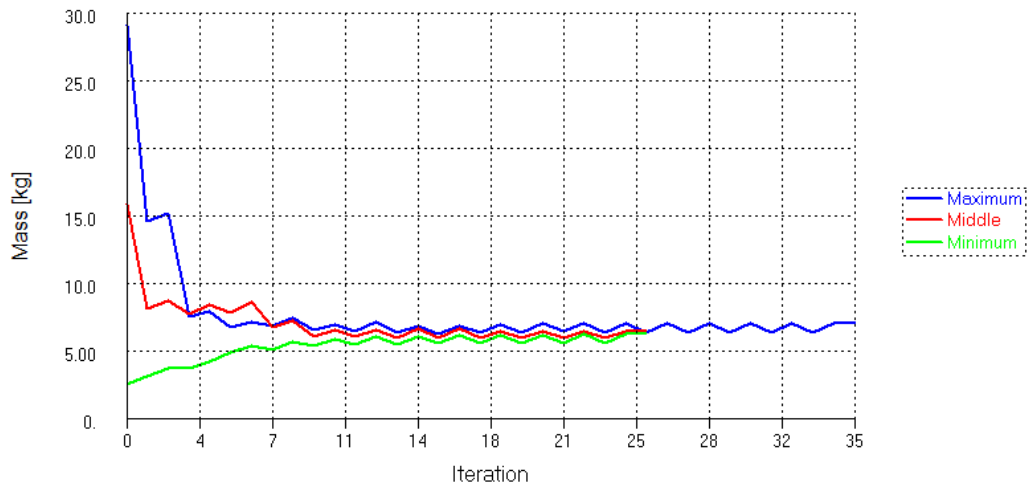


Figure 4.19: Discrete optimization iterations for the Mesh 1 / Three different initial values for design variables / Strength and local buckling constraints

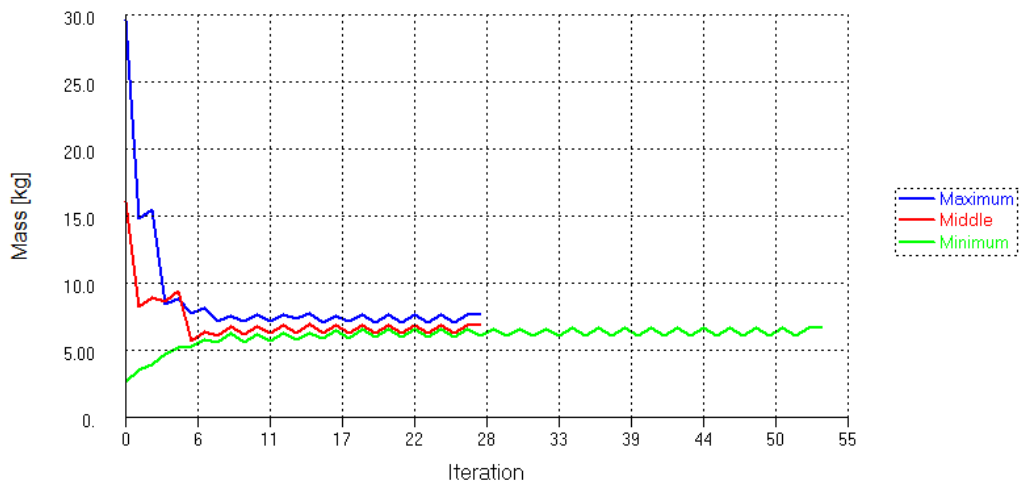


Figure 4.20: Discrete optimization iterations for the Mesh 2 / Three different initial values for design variables / Strength and local buckling constraints

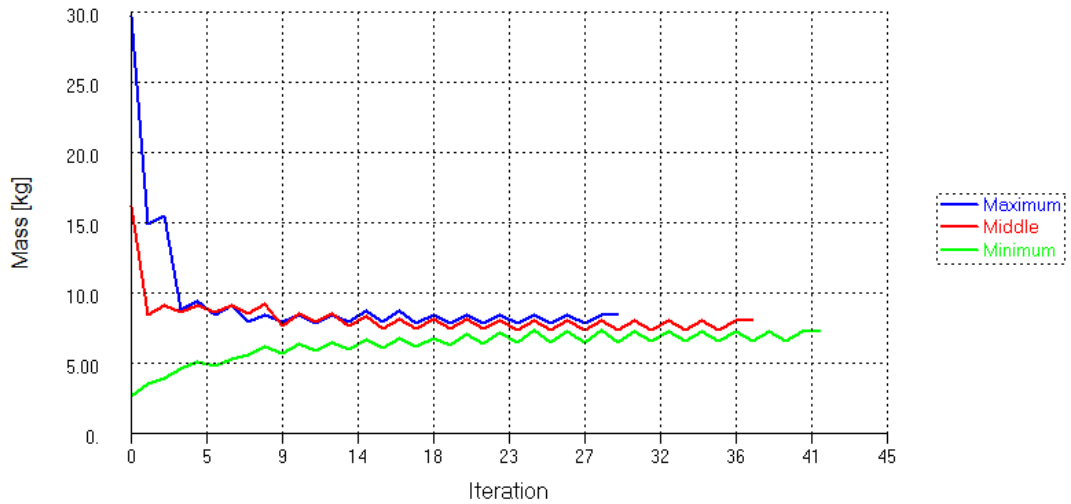


Figure 4.21: Discrete optimization iterations for the Mesh 3 / Three different initial values for design variables / Strength and local buckling constraints

In the discrete optimization, a continuous optimization is done at the first iteration. In the next iteration, as mentioned in Chapter 4.4.1.1, DOE selects the next smaller and the larger discrete value around the value obtained by the continuous optimization for each discrete design variable. Then, a proper OA is selected, the objective and constraint functions are evaluated for each design combination of the OA by the approximation method and the best discrete design is selected. Then, a finite element analysis is carried out and the discrete design is checked whether it is hard or soft feasible. According to this check, next continuous optimization iteration starts or optimization stops. Because of this process, fluctuations are seen in Figures 4.19 – 4.21. For the strength constraint and local buckling constraints together, the calculated optimum masses of the horizontal tail plane are tabulated in Table 4.10 for the discrete design variable case.

Table 4.10: Optimization results for the combined strength and local buckling constraints using discrete design variables

Initial Values	Mesh 1	Mesh 2	Mesh 3
MINIMUM	6.17 kg	6.58 kg	7.21 kg
MIDDLE	6.44 kg	6.81 kg	7.99 kg
MAXIMUM	6.97 kg	7.56 kg	8.39 kg

Comparison of the mass results obtained from optimizations given in Table 4.10 with those given in Table 4.9 reveals that discrete optimization produces higher optimum masses compared to the continuous optimization. This is an expected result because while the DOE selects next smaller discrete design variable for some variables, it may also select the next larger discrete design variables for some other. If the DOE results give lower value than the continuous optimization results, that would be infeasible. If round-up method were used rather than the DOE, that would give overweight results. Therefore, DOE is a very efficient method to get feasible and not too heavy results.

Again as in the continuous optimization, when the initial values are selected near the lower limit of the design variables, optimum masses are the lowest. For the Mesh 3 case, there is approximately 1 kg difference between the mass values obtained using the lower and upper limits of the design variables as initial values of the design variables. Based on the results of both continuous and discrete optimization, it is considered that global optimum is obtained when the initial values are selected near the lower limit of the design variables. Moreover, since Mesh 3 captures the stress gradients better, optimum mass of the aluminum horizontal tail is approximately 7.21 kg.

For the optimization which gives 7.21 kg optimum weight, thickness variation could be seen in Figures 4.22 and 4.23.

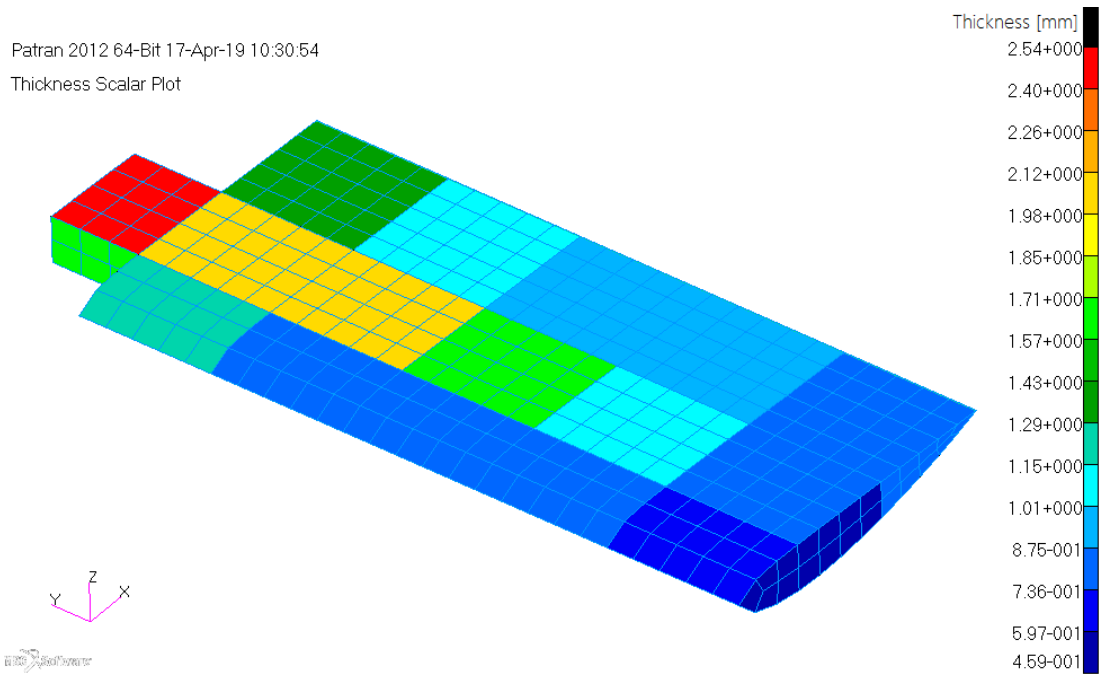


Figure 4.22: Optimum thickness variation for the Mesh 3 HTP with the upper skin /
Minimum initial values / Discrete design variables / Strength and buckling
constraints together

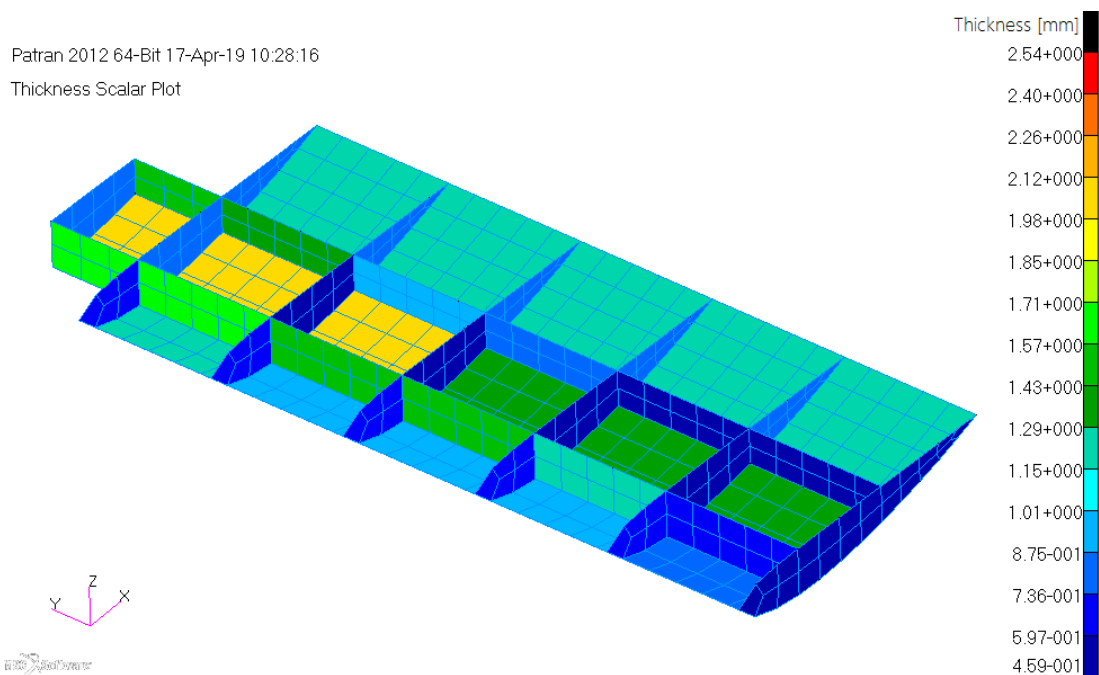


Figure 4.23: Optimum thickness variation for the Mesh 3 HTP without the upper skin
/ Minimum initial values / Discrete design variables / Strength and buckling
constraints together

In the present study, at the converged optimum, constraints are also checked whether they are violated or not. According to Figure 4.22 and 4.23, it is seen that thickness constraints did not violated. Constraint history of the optimization that gives 7.21 kg optimum weight is checked. Maximum value of constraint history of this optimization is shown in Figure 4.24.

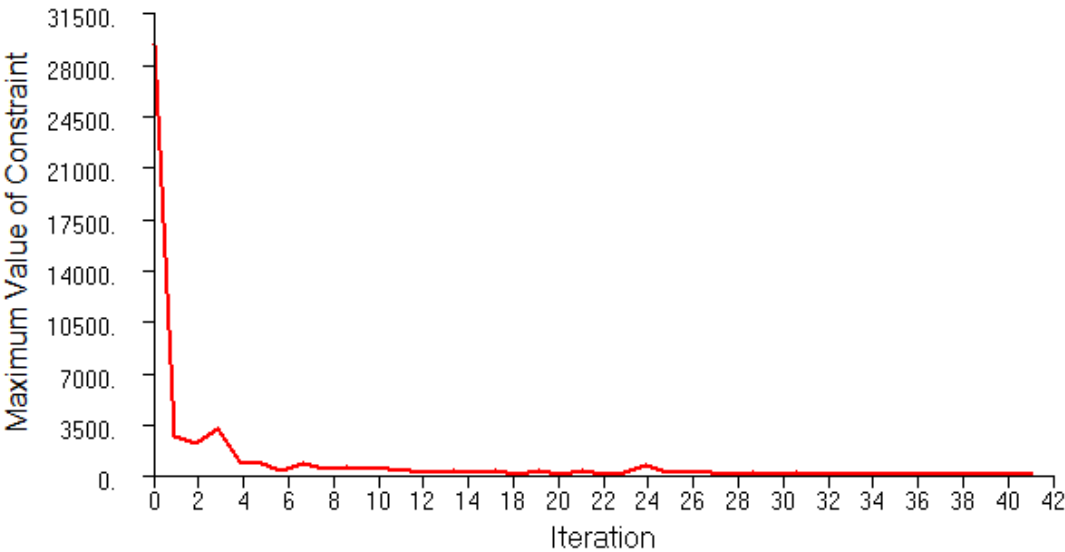


Figure 4.24: Maximum value of the constraint vs. iteration number of the optimization that gives 7.21 kg as the optimum mass

These constrain values refer to the unitless normalized constraints constructed internally in NASTRAN. The normalized constraints are especially useful since the dependence on the magnitude of the response quantity has been removed. Furthermore, the hard convergence decision logic checks the relative changes in properties and design variables if the limit on the maximum constraint value is not satisfied. The purpose of this check is to determine whether the design is changing for the case of violated constraints. If the design is still varying, optimization can continue in order to try to overcome the constraint violations. However, if the design is not changing, then we are at a point in the design space that represents a best compromise solution among the violated constraints [4]. In conclusion, NASTRAN allows slight constraint violations at the converged optimum.

In Figure 4.24, maximum value of constraint starts with a very high number, then decreases sharply and ends up with a value of 4.4. NASTRAN has a default 0.005 value for the maximum constraint violation at the converged optimum. Hence, the violated constraint is investigated by checking the NASTRAN result file (f06). It is observed that 6th zone of upper middle skin which has 2.54 mm thickness has a local buckling constraint violation. This panel is shown by the red thickness color at the root of the HTP in Figure 4.22. Afterwards, it is investigated that how much constraint violation has occurred and if it is acceptable or not.

As pointed out before, local buckling equation used in the skins is given by Equation 4.11. This equation needs shear stress, normal y stress and thickness of that region. At the optimum solution, thickness in the root panel is 2.54 mm according to optimization result. Figures 4.25 and 4.26 show the shear and the normal y stresses of 6th zone of upper middle skin respectively.

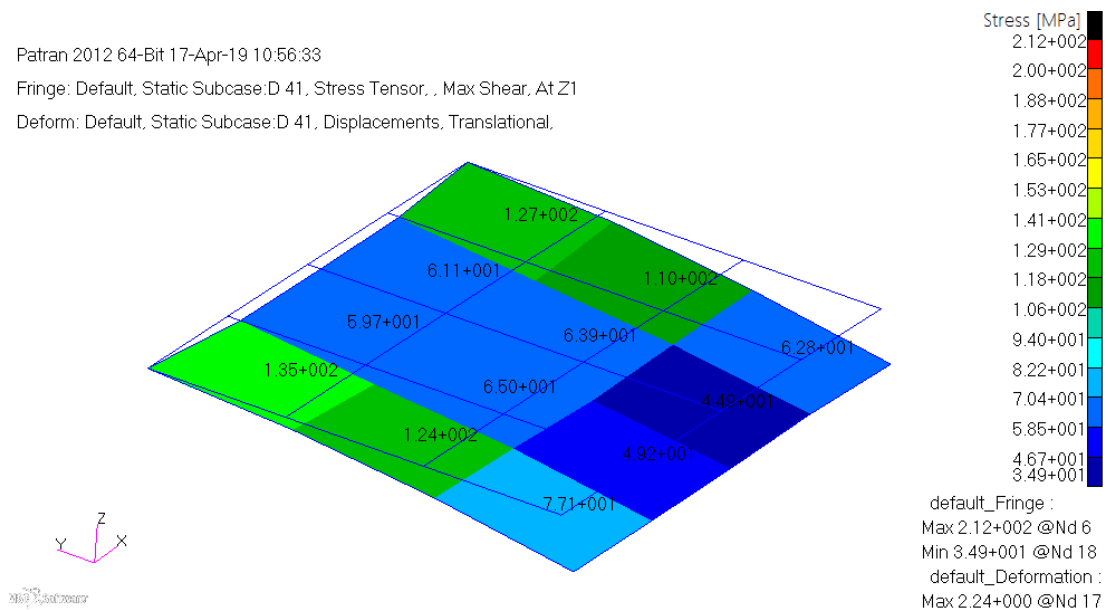


Figure 4.25: Shear stresses in the elements of the upper middle skin 6th region

The average shear stress of this region is calculated 53.74 MPa according to Figure 4.25.

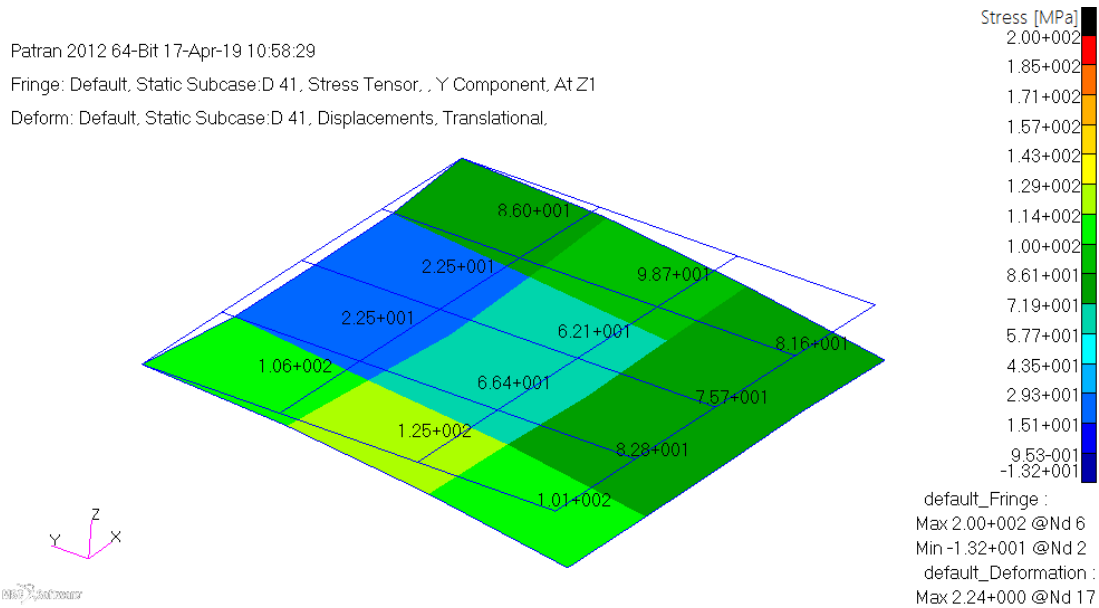


Figure 4.26: Normal y stresses in the elements of the upper middle skin 6th region

According to Figure 4.26, the average normal y stress of this region is 77.52 MPa. When these values are substituted to Equation 4.11, combined local buckling equation gives a value of 2.01. It is to be noted that the upper bound of the local buckling constraints is 1.01. Therefore, it is confirmed that constraint violation has occurred in this region. If the next discrete thickness design variable value, which is 3.56 mm, is used for that region without changing stress values, the Equation 4.11 gives a value of 0.97. Therefore, if 3.56 mm thickness is used, then average shear and normal y stresses in this region would decrease and combined local buckling equation would give a lower value than 0.97. It should be noted that for the region of interest, even though the upper limit of the discrete thickness has not been reached, since the objective function is not changing, even if there is constraint violation, a hard convergence with best compromise is reached. In the detail design phase of the project 3.56 mm thickness would be a better choice for this region since for the 3.56 mm thickness there would be no constraint violation.

It should also be noted that in the aerospace industry, to achieve further weight reduction, local skin buckling is allowed for the skin panels which are under pure compression. For the aluminum HTP, when the NASTRAN result file (f06) is investigated, local buckling of the related front and rear spar regions and the ribs has

not occurred. Therefore, the inner structure is still solid. Considering that this study is a preliminary design study, local buckling of the root panel at the converged optimum could be acceptable.

4.6. Optimization of the Aluminum HTP Using Line Distributed Load

As mentioned at the end of Chapter 3.3, an extra optimization study has been done in this section to confirm the conclusions that are made before related to the results obtained with different mesh densities and the captured stresses.

Total lift force measured from the CFD mesh is equal to 4978.26 N and front spar has 1415 mm length. Therefore, a downward 3.5182 N/mm line distributed load has been applied to the finite element models with different mesh densities as the helicopter HTP creates downward lift force. In Figures 4.27 – 4.29, load applications are shown on finite element models with mesh densities Mesh 1, 2 and 3.

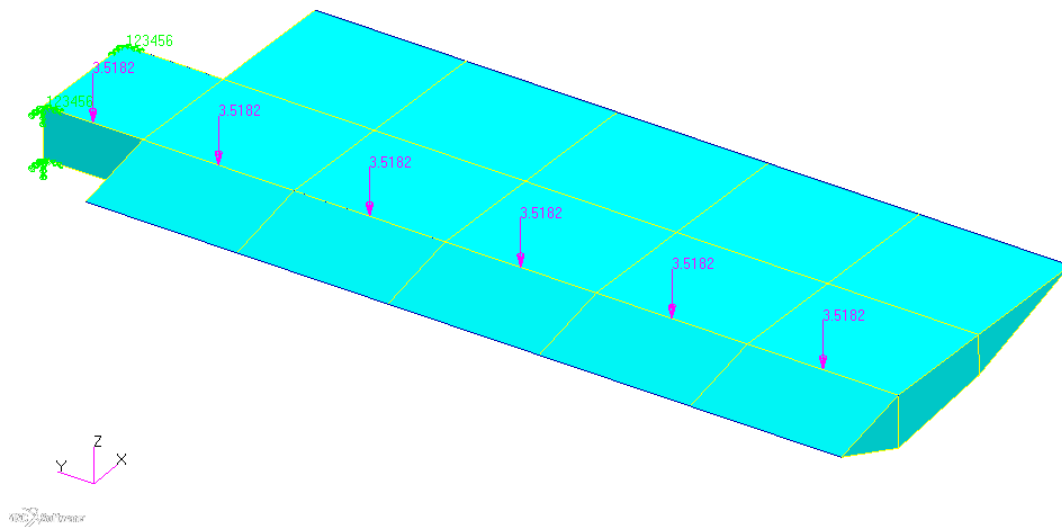


Figure 4.27: Line distributed load application on Mesh 1 through the front spar

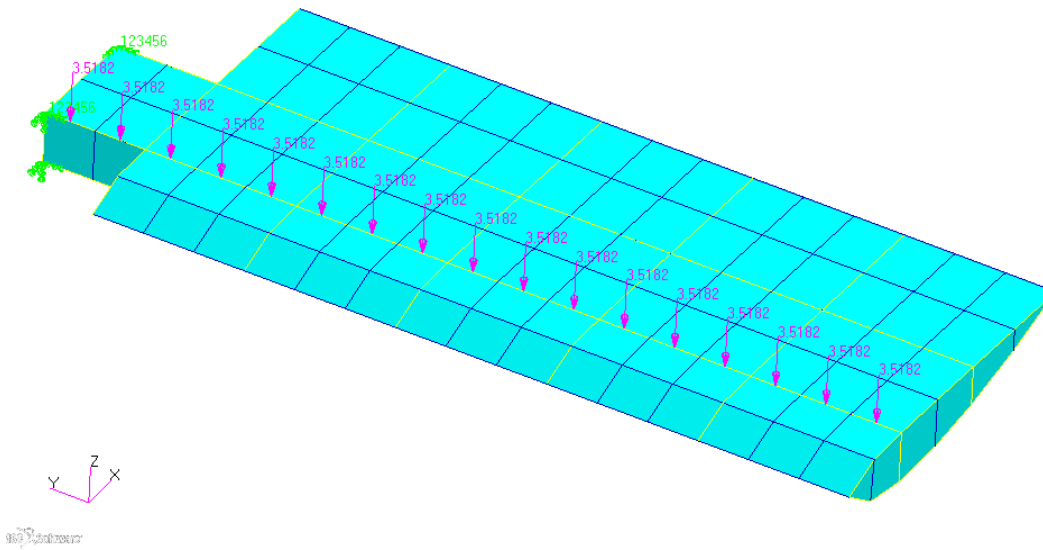


Figure 4.28: Line distributed load application on Mesh 2 through the front spar

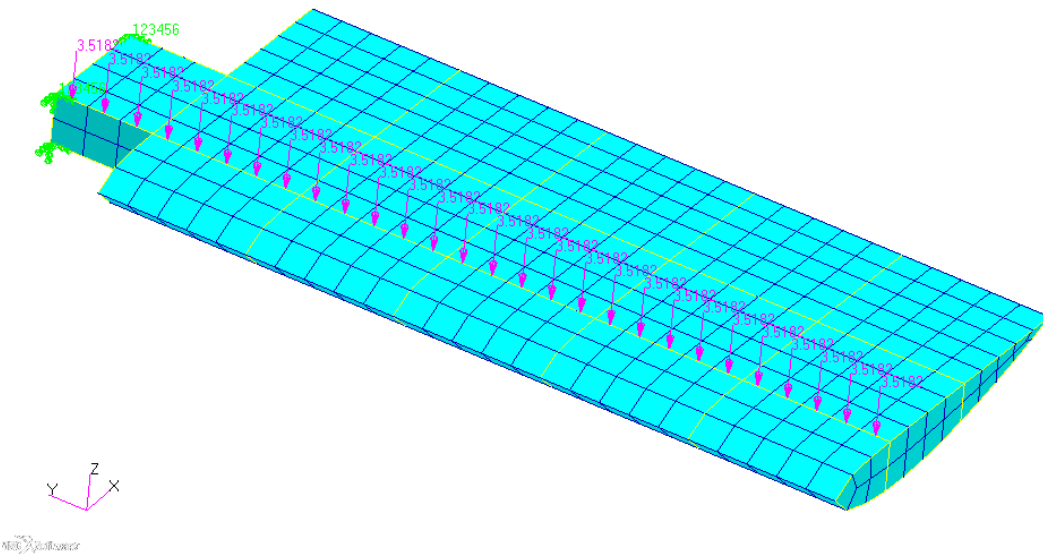


Figure 4.29: Line distributed load application on Mesh 3 through the front spar

For this optimization study, minimum initial values of the design variables are used, because in the previous analyses it is observed that minimum values give lighter HTP weight. As for the constraints, strength and local buckling constraints is used since the use of both constraints is more crucial for the optimum sizing of the HTP. In addition, discrete design variables are used to get results that are more realistic.

Utilizing the same design variables as before and the strength and local buckling constraints, minimum weight optimizations are done. In Figure 4.30, optimization iterations are shown for the Mesh 1, Mesh 2 and the Mesh 3.

In Table 4.11, the final calculated optimum masses of the horizontal tail plane for the Mesh 1, Mesh 2 and the Mesh 3 are tabulated.

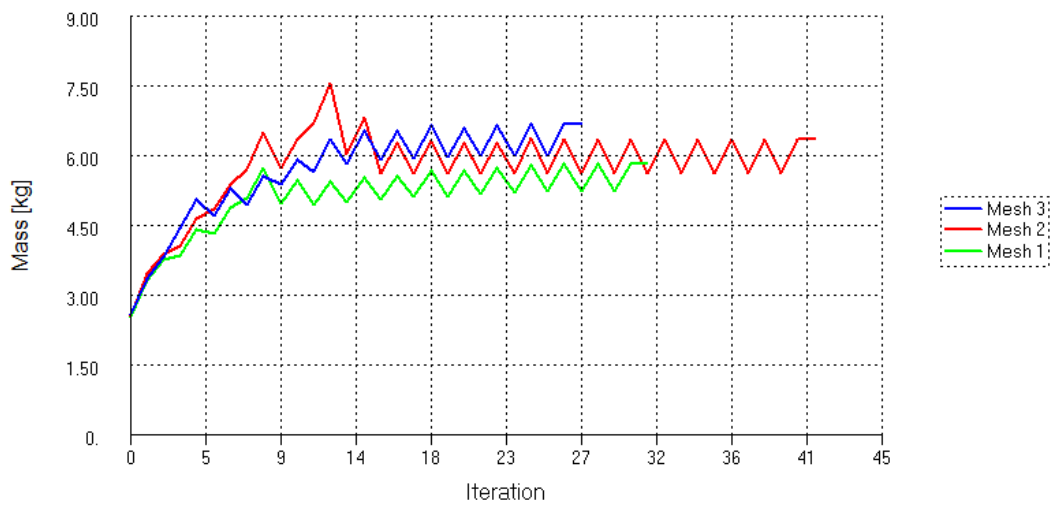


Figure 4.30: Discrete optimization iterations for the minimum initial value design variables / Three different mesh densities / Strength and local buckling constraints / line distributed load applied

Table 4.11: Optimization results for the combined strength and local buckling constraints using discrete design variables with line distributed load applied

Initial Values	Mesh 1	Mesh 2	Mesh 3
MINIMUM	5.81 kg	6.32 kg	6.68 kg

Previously, the applied load on the structural model was the interpolation of the CFD pressure. In this subsection, exactly the same line distributed load that is equal to the total lift force of the CFD pressure is applied to front spar of HTP that is meshed with Mesh 1, 2 and 3 densities. Figure 4.25 and Table 4.11 confirm that as the mesh

density increases, the optimum mass also increases when exactly the same load application is used in the finite element analyses with different mesh densities. As discussed before, because the finer mesh captures the stress gradients better, the optimum mass increases. Hence, with the same line load application, similar conclusion with regard to the effect of mesh density on the optimum HTP mass has been obtained.

CHAPTER 5

OPTIMIZATION OF THE COMPOSITE HTP

5.1. Introduction

In this chapter, material properties that are used for whole composite HTP structure are given. Then, application of the finite element method for composite structures and the composite optimization process are explained. At the end of the chapter, all optimization results for the composite optimization are given via tables and figures.

5.2. Material Properties

Main composite material that is used in aerospace industry is the carbon fiber reinforced plastic (CFRP) which consists of carbon fibers in a polymer matrix. CFRP plies could be unidirectional (UD) such that fibers are in one direction or woven such that fibers are in two directions. UD plies are thinner than woven plies and gives flexibility to the optimization problem, hence in the present study UD carbon prepreg material is chosen as the base material.

HexPly 8552 UD Carbon prepreps are commonly used UD CFRP composites in aerospace structures and are well known in TAI, so HexplyAS4/8552/RC34/AW134 UD prepreg material is chosen for the present optimization study. In all structural elements in this chapter, this prepreg is used. Material properties of the HexplyAS4/8552/RC34/AW134 are shown in Table 5.1. In Table 5.1, “1” denotes the fiber direction and “2” denotes the transverse direction.

Table 5.1: Material properties of HexplyAS4/8552/RC34/AW134

	Composite Material: HexPlyAS4/8552/RC34/AW134
Elastic Modulus 11, E_{11}	130000 N/mm ²
Elastic Modulus 22, E_{22}	8700 N/mm ²
Poisson's Ratio 12, ν_{12}	0.36
Shear Modulus 12, G_{12}	2900 N/mm ²
Tension Stress Limit 11, X_T	2280 N/mm ²
Tension Stress Limit 22, Y_T	35 N/mm ²
Compression Stress Limit 11, X_C	1360 N/mm ²
Compression Stress Limit 22, Y_C	223 N/mm ²
Shear Stress Limit, S	107 N/mm ²

5.3. FE Model Properties

Material properties are created as 2D orthotropic material in the PATRAN environment for the composite optimization problem. In the PATRAN GUI, linear elastic properties such as elastic modulus, Poisson's ratio, shear modulus and density values are entered along with the TSAI-WU stress failure limits such as tension, compression and shear strengths are defined.

Following the definition of the ply properties, composite laminates are created for all 63 design variable regions including 32 regions in the skins, 19 regions in the ribs and 12 regions in the spars. Initially, every laminated composite region has symmetric 4 ply stacking sequence with given thickness and orientations as design variables. In the optimization process, ply numbers change, hence thickness of the design regions change.

Four different coordinate axes are created for the skins, spars and the ribs to define the material orientation while creating the 2D shell properties. In all coordinate axes, fiber direction is the x direction, transverse direction is y, and out of plane direction is z.

For spars, local axis defined for the material orientation is shown in Figure 5.1.

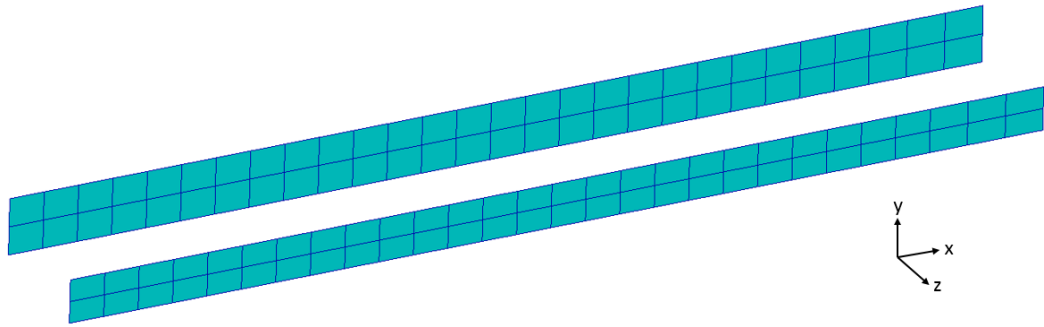


Figure 5.1: Material coordinate axis for spars

For the lower and upper skin, local axes defined for the material orientation are shown in Figures 5.2 and 5.3, respectively.

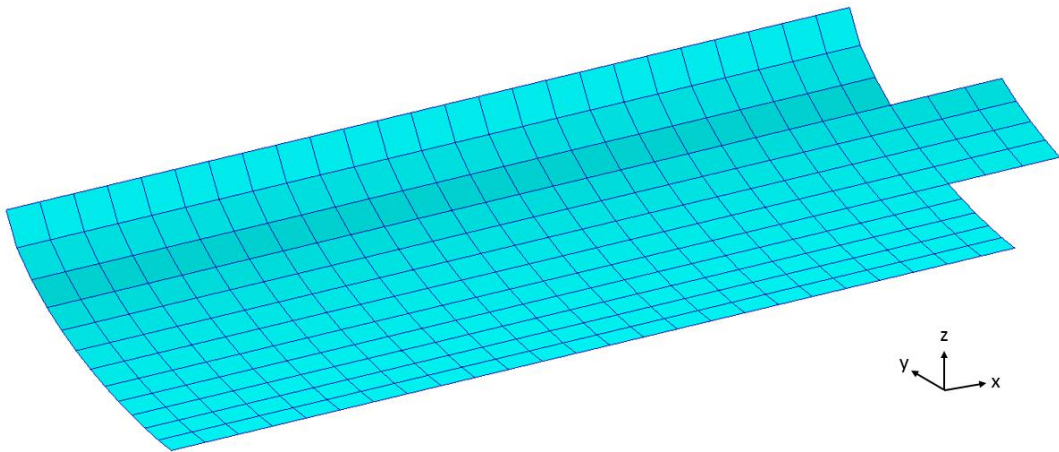


Figure 5.2: Material coordinate axis for lower skin

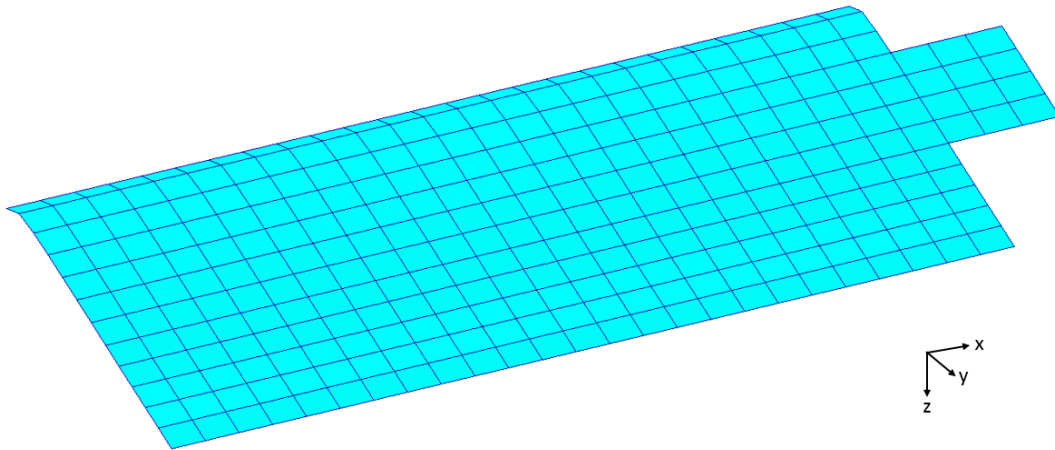


Figure 5.3: Material coordinate axis for upper skin

For the ribs, flight direction is taken as the zero direction. For the ribs, local axis defined for the material orientation is shown in Figure 5.4.

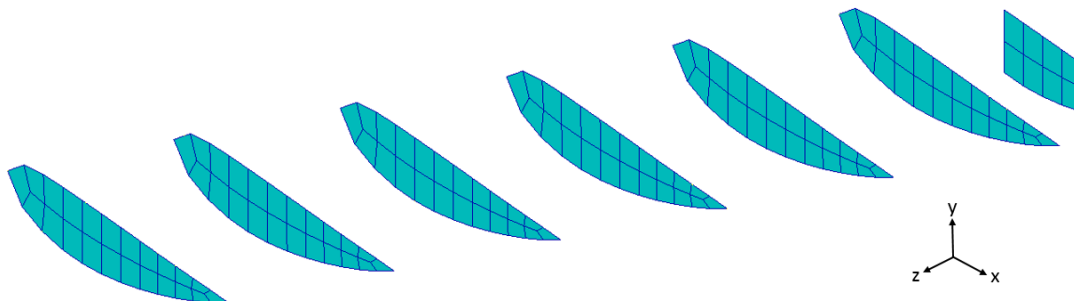


Figure 5.4: Material coordinate axis for ribs

With these material orientations and composite laminate stacking sequences, 2D shell material properties are defined for all design variable regions.

5.4. Formulation of the Optimization Problem for the Composite HTP

5.4.1. Design Variables

In composite optimization, unlike aluminum optimization, design variables are ply thicknesses and ply orientations in every design region. As mentioned before, symmetrical composite laminates are used in every design region. Thicknesses and ply orientations of the upper four plies of laminated composite plates are defined as design variables, and according to thickness of the plies, ply numbers change. Unlike aluminum optimization, no flange is modeled in composite optimization as design variables. In the composite optimization problem, there are 63 design regions like in aluminum optimization. Hence, there are 252 ply thickness design variables and 252 ply orientation design variables.

In composite HTP optimization problem, there are 16 skin design regions in the upper skin and 16 design regions in the lower skin named same with aluminum HTP optimization problem as shown in Figure 4.5 and 4.6. Figure 5.5 shows the design regions defined for the ribs, there are no flanges defined. In total, there are 19 design regions in the ribs.

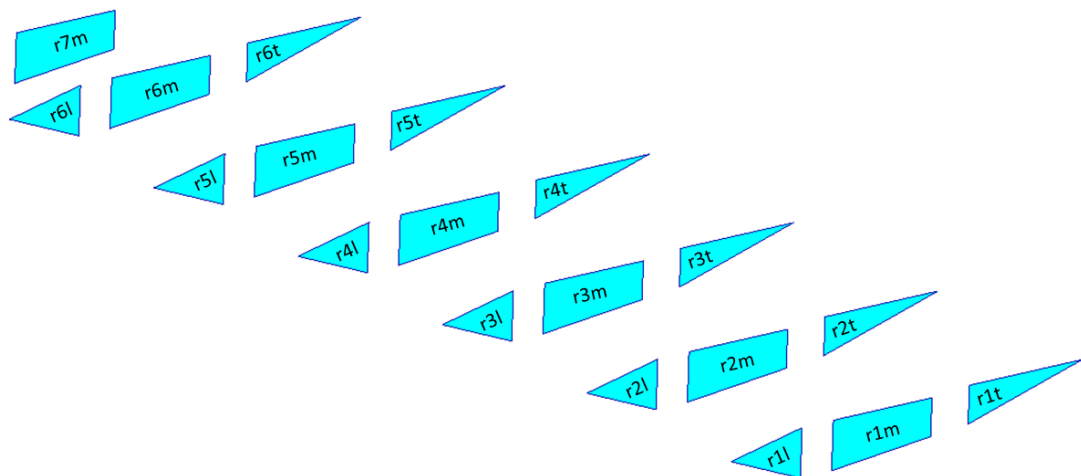


Figure 5.5: Rib design regions and design region names

Figure 5.6 shows the design regions defined for the spars. In total, there are 12 design regions in the spars, different from aluminum optimization there no flanges defined in the spars also.

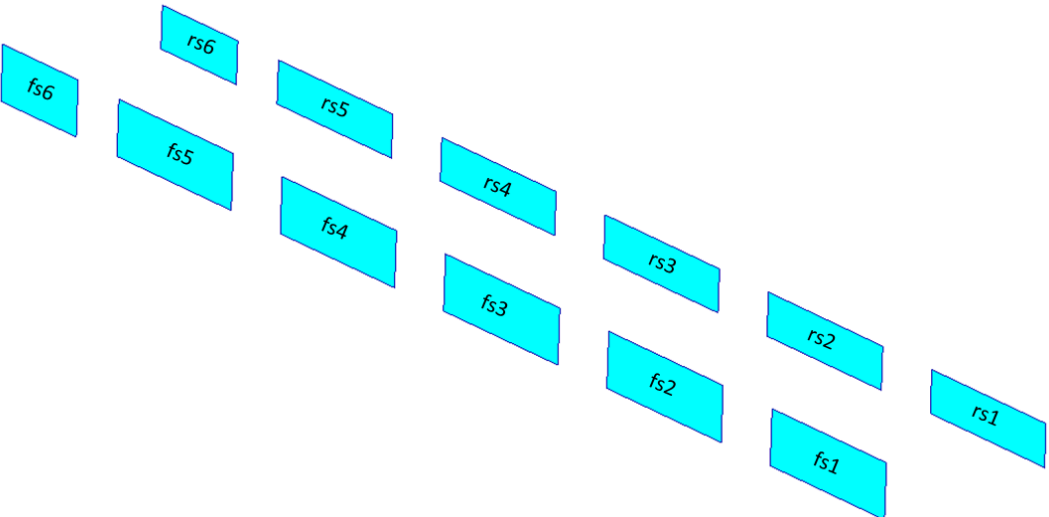


Figure 5.6: Spar design regions and design region names

Table 5.2 summarizes the design regions and the number of ply thicknesses and the fiber orientations used as the design variables.

Table 5.2: Design variables (ply thickness and orientation) for the composite HTP optimization

	Number of Design Regions	Number of Ply Thicknesses	Number of Ply Orientations
Upper Skin	16	64	64
Lower Skin	16	64	64
Leading Edge Ribs	6	24	24
Center Ribs	7	28	28
Trailing Edge Ribs	6	24	24
Front Spar	6	24	24
Rear Spar	6	24	24
Total	63	252	252

It should be noted that in composite optimization, firstly, only ply thickness optimization has been performed for a predefined ply orientation. Then, combined ply thickness and ply orientation optimization has been performed.

5.4.1.1. Discrete Design Variables

Ply thicknesses and ply orientation variables are continuous variables for the optimization problem when discrete design variables are not defined. However, in real life, a ply has a constant thickness and in this study for the composite material used, cured ply thickness is taken as 0.13 mm. Then, thickness is controlled with the number of plies. For a specified ply number, ply thickness is multiplied by the ply number and by doing this; thickness has been defined as a discrete design variable. Therefore, when the optimization results are investigated, resulting ply thicknesses allow one to calculate the number of plies used.

In addition to the ply thickness, ply orientations are defined as discrete design variables and 0° , 90° , 45° and -45° ply angles are commonly used as the base ply orientations. Discrete ply thicknesses and ply orientations that are used are tabulated in Table 5.3:

Table 5.3: Discrete design variables used for the composite HTP optimization

Ply Thicknesses	0.13 mm (for 1 ply)	0.26 mm (for 2 plies)	0.39 mm (for 3 plies)	0.52 mm (for 4 plies)
Ply Orientations	-45°	0°	45°	90°

5.4.1.2. Initial Values of the Design Variables

In the aluminum optimization, lower initial value gave minimum mass optimization results; so in the composite HTP optimization, minimum values of the design variables are used by taking 1 ply of each discrete ply orientation for each design variable. A symmetric and balanced laminate with $[-45/90/45/0]_s$ stacking sequence is given for every design region as input in the optimization of the composite HTP. Figure 5.7 shows the initial stacking sequence used in all design regions.

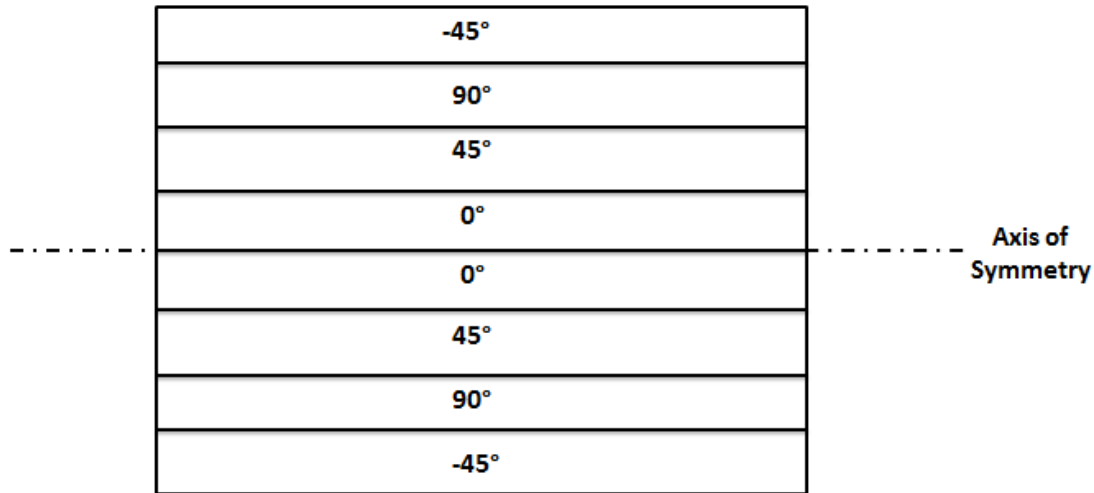


Figure 5.7: Initial stacking sequence for all design regions

5.4.2. Constraints

For the composite optimization, failure and local buckling are taken as constraints. For composite failure Tsai-Wu failure criterion has been taken as the failure criterion. In this thesis study, the effects of constraints are investigated in two steps. Firstly, only the strength constraint is applied, and then strength and local buckling constraints are applied together. In addition to these two constraints, there is an extra geometric constraint created to reach the global optimum.

5.4.2.1. Strength Constraints

In NASTRAN, there are more than one composite failure theories for the stress failure. These theories use ply allowable stresses and failure indices that are calculated at the ply level. In this work, Tsai-Wu failure theory is chosen. If failure indices are greater than 1.0, it means that a ply has failed. Tsai-Wu Failure theory equation [25] as a constraint is given by Equation 5.1.

$$\frac{\sigma_1^2}{X_T X_C} + \frac{\sigma_2^2}{Y_T Y_C} + 2F_{12}\sigma_1\sigma_2 + \frac{\tau_{12}^2}{S^2} + \sigma_1 \left[\frac{1}{X_T} - \frac{1}{X_C} \right] + \sigma_2 \left[\frac{1}{Y_T} - \frac{1}{Y_C} \right] \leq 1 \quad (5.1)$$

where,

σ_1 : Axial Stress in 1 direction

σ_2 : Axial Stress in 2 direction

τ_{12} : Shear Stress

X_T : Tension Stress Limit in 1 direction

Y_T : Tension Stress Limit in 2 direction

X_C : Compression Stress Limit in 1 direction

Y_C : Compression Stress Limit in 2 direction

S : Shear Stress Limit

F_{12} : Interaction Coefficient

The interaction coefficient F_{12} is experimentally determined from test specimens under biaxial loading [25]. Narayanaswami and Adelman [26] have suggested that this parameter could be set to zero and the uses of Hoffman's Theory or the Tsai-Wu theory with $F_{12} = 0$ are preferred alternatives [25]. Hence, in this study the interaction coefficient is taken as zero.

5.4.2.2. Local Buckling Constraints

In the aluminum HTP optimization, local buckling equations are written in the NASTRAN input file. For each iteration, the optimization code ensured the satisfaction of the local buckling constraints. For composite materials, there are many ways to derive local buckling equations in the literature; but all of them make symmetry and balanced laminate assumptions for the stacking sequence. A laminate is symmetric when the sequence of plies below the laminate's mid-plane is a mirror image of the stacking sequence above the mid-plane, and is balanced when all laminate at angles other than 0 degree and 90 degree occur in opposing pairs (not necessarily adjacent) that are symmetrical with respect to the centerline [27].

Since symmetry condition is an option in PATRAN, symmetry condition can be achieved in each iteration of the optimization, but there is no balanced laminate option in PATRAN for optimization problems. Hence, if ply orientations are taken as design variables, balanced laminate condition cannot be achieved in every iteration. Even if the orientations were not design variables and only the ply thicknesses are the design variables, again balanced laminate condition cannot be achieved because same number of plies with positive and negative ply angles could not be equal. Therefore, writing local buckling design equations in NASTRAN input file as constraints was not possible in composite optimization because of not being able to achieve balanced laminate during the optimization process.

Nevertheless, a buckling equation for a symmetric and balance plate that is available in the literature is checked whether it could be used for an unbalanced plate or not by comparing the results of the analytical formulation with the NASTRAN buckling analysis results.

Critical buckling load equation is investigated for a simply supported composite plate under axial compressive load. Figure 5.8 shows the plate under the compressive load.

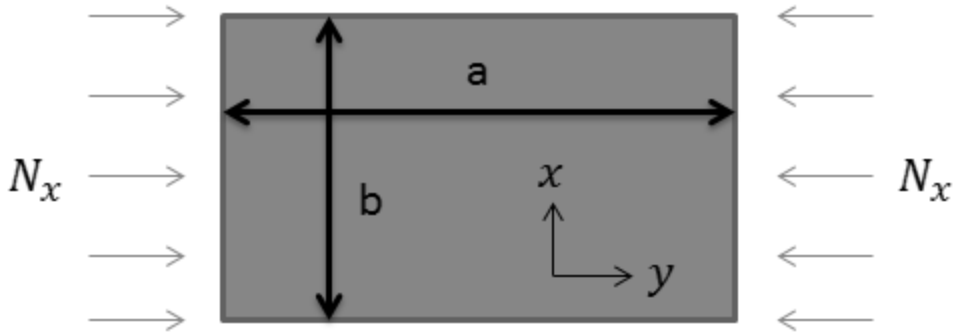


Figure 5.8: Plate with under compressive load

In the thesis of Qiao Jing Yang, for the simply supported composite plate, critical buckling load equation is given by [28],

$$N = D_{11} \left(\frac{m\pi}{a}\right)^2 + (2D_{12} + 4D_{66}) \left(\frac{n\pi}{b}\right)^2 + D_{22} \left(\frac{a\pi}{m}\right)^2 \left(\frac{n}{b}\right)^2 \quad (5.2)$$

where D_{ij} is the bending stiffness coefficient and m and n are positive integers representing the number of half sine waves in the axial and transverse directions, respectively. The critical buckling load is the smallest axial load N_x which can be obtained by setting $n=1$ and varying m .

Initially, for a symmetric and balance composite plate, critical buckling load is calculated with using Equation (5.2). Then a PATRAN model is created for that plate and the buckling load results are compared to check the agreement of the finite element solution and Equation (5.2) for the symmetric and balanced laminate condition.

A composite plate with simply supported boundary conditions, which has $[90/0/0/90]$ laminate sequence, and has a length of 250 mm ($a= 250$ mm) and width of 208 mm ($b=208$ mm) is investigated. A MATLAB code is written, ABD matrices are calculated and buckling load N versus m values are plotted to find the smallest buckling load. MATLAB code that is written to calculate load is given in Appendix D.

Figure 5.9 gives the variation of the critical buckling load versus the axial wave number m .

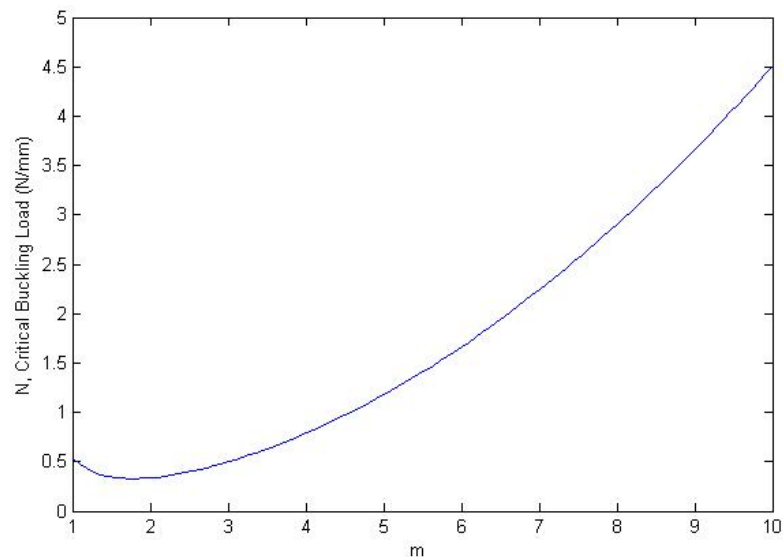


Figure 5.9: Critical buckling load variation versus the axial wave number m

According to Figure 5.9, Equation 5.2 gives the critical buckling load as 0.34 N/mm.

Then, the same simply supported plate is modeled in PATRAN and a unit-distributed load is applied to calculate the lowest eigenvalue corresponding to the critical buckling load. Figure 5.10 shows the simply supported composite plate subjected to unit distributed unit load.

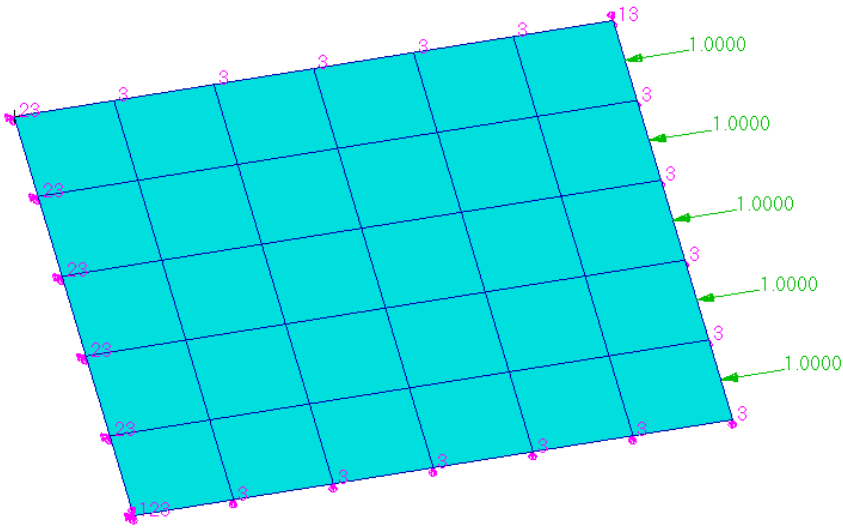


Figure 5.10: Simply supported composite plate subjected to unit distributed unit load

Then buckling analysis is run and eigenvalue is found as 0.356 N/mm. Figure 5.11 shows the buckling mode shape for the plate model for the relatively fine mesh.

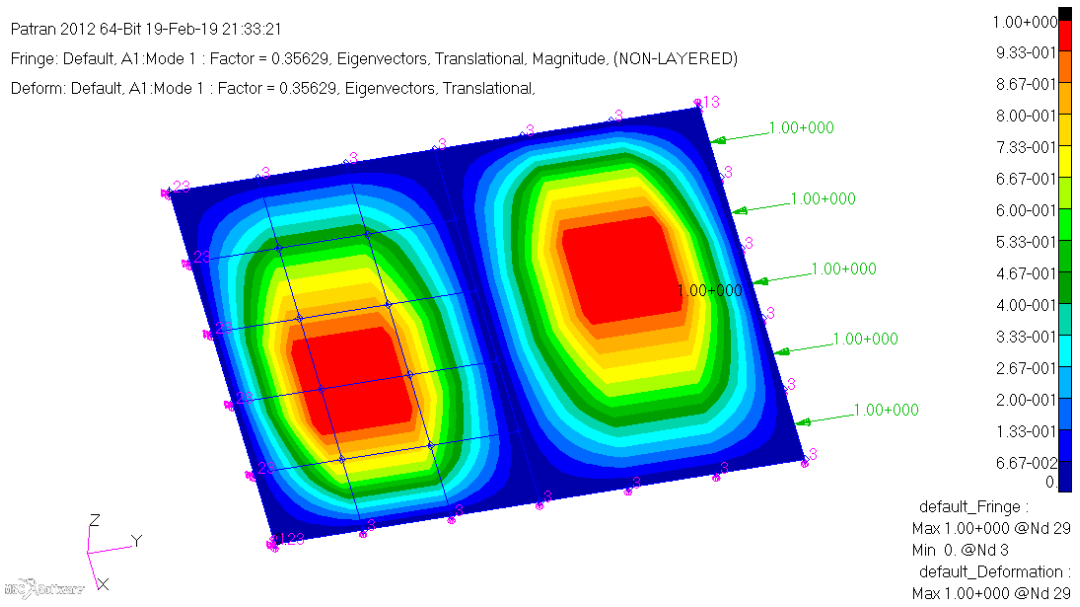


Figure 5.11: Buckling analysis result for relatively fine mesh

At this point, it is assumed that Equation (5.2) is useful and reliable for symmetric and balanced laminates. In addition, it is observed that buckling analysis gives accurate result when mesh density is relatively fine.

To check the effect of unbalanced plies on the buckling load, certain design regions in the wing are modeled in PATRAN with symmetric but unbalanced stacking sequence for buckling analysis, and eigenvalues are calculated by using NASTRAN. For the unbalanced laminate and with the corresponding “a” and “b” values, Equation (5.2) is also used to calculate the buckling load. Nevertheless, before checking the effect of unbalanced stacking sequence on the buckling load, a laminate with symmetric and balanced stacking sequence is checked to investigate the curvature effect of the skins on the buckling load. It should be noted that Equation (5.2) calculates critical buckling load for flat surfaces and curved surfaces have different critical buckling loads.

For instance, middle lower skin 3th zone is fine meshed as shown in Figure 5.12.

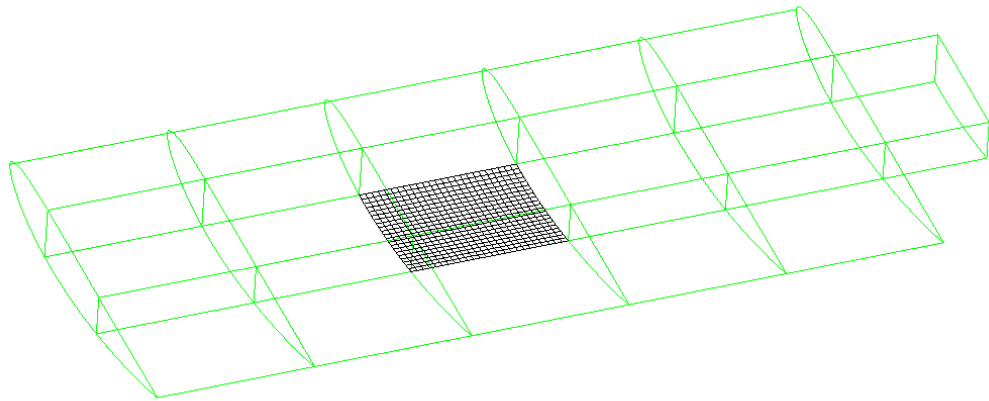


Figure 5.12: Fine meshed middle lower skin, 3th zone

As shown in Figure 5.13, unit distributed load is applied to the simply supported curved middle lower skin in the 3th zone design region which is made of balanced laminate with the $[-45/90/90/45/0/0]_s$ stacking sequence.

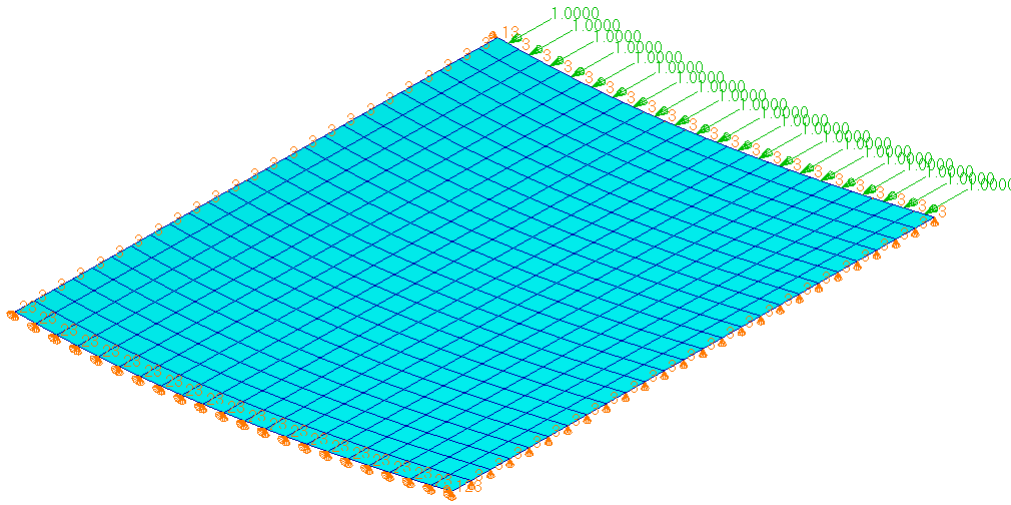


Figure 5.13: Simply supported panel with distributed unit load applied to the middle lower skin in the 3th zone

After the buckling analysis, critical buckling load is calculated as 9.04 N/mm, and Figure 5.14 shows the buckled mode shape for the particular panel.

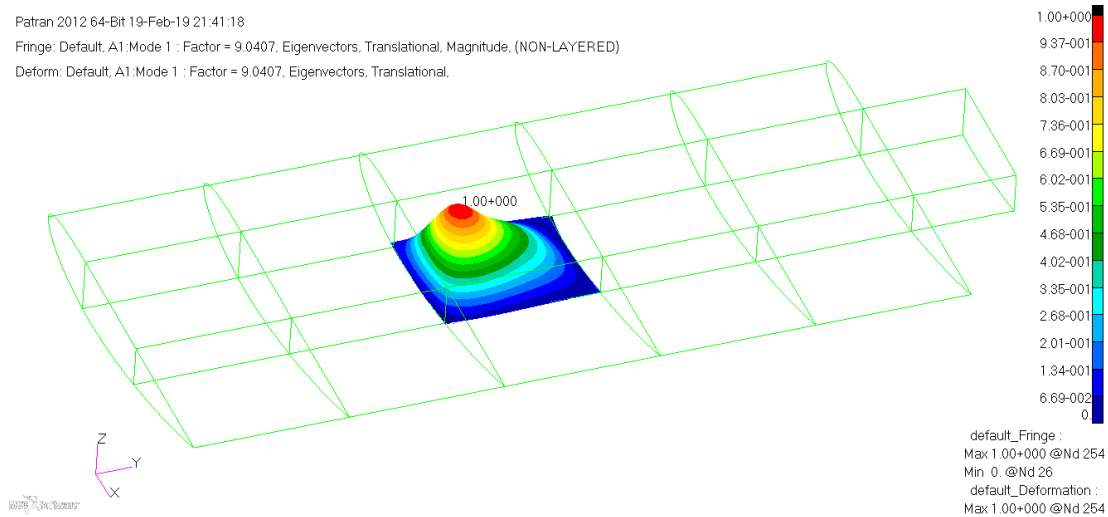


Figure 5.14: Buckling analysis result for the middle lower skin 3th zone with the $[-45/90/90/45/0/0]_s$ stacking sequence

Then, for the same panel a and b values are taken, but they are used in the flat surface buckling equation given by Equation (5.2) and the variation of the critical buckling load with the m value is obtained and this variation is given in Figure 5.15.

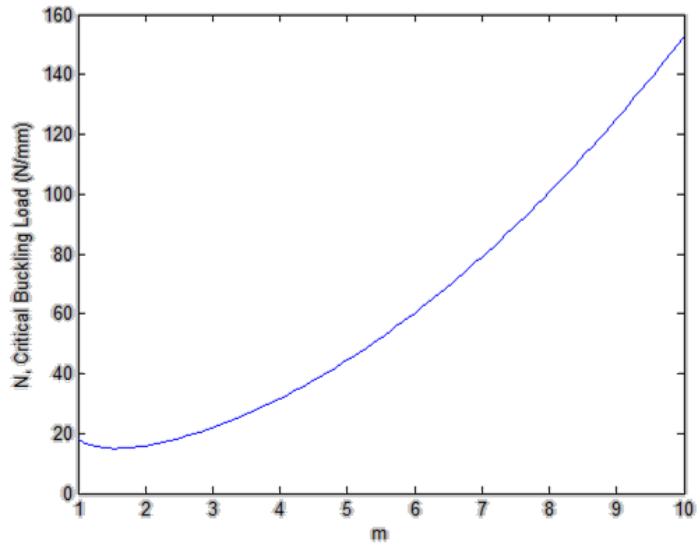


Figure 5.15: Variation of the critical buckling load with the m value for the middle lower skin, 3th zone

From Figure 5.15, critical buckling load is determined as 14.92 N/mm which is 65% higher than the finite element analysis result. Hence, Equation (5.2) cannot be used for design regions with curved surfaces assuming that they are flat surfaces.

After checking the curvature effect, unbalanced and symmetric stacking sequence is investigated for flat surfaces. For instance, front spar 4th zone is fine meshed and unit distributed load is applied to the unbalanced laminate with the stacking sequence $[-45/90/90/45/45/0/0]_s$, as shown in Figure 5.16.

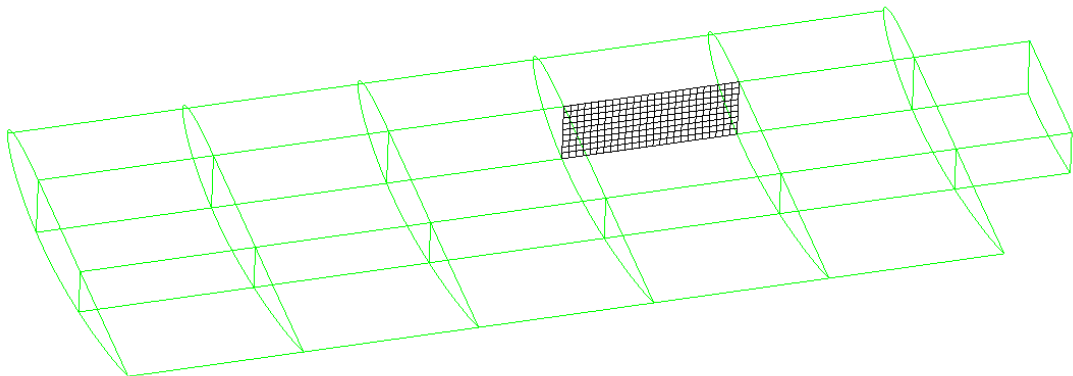


Figure 5.16: Simply supported flat panel with distributed unit load applied to the front spar web in the 4th zone

After the buckling analysis, critical buckling load is calculated as 28.82 N/mm, and Figure 5.17 shows the buckled mode shape for the particular panel.

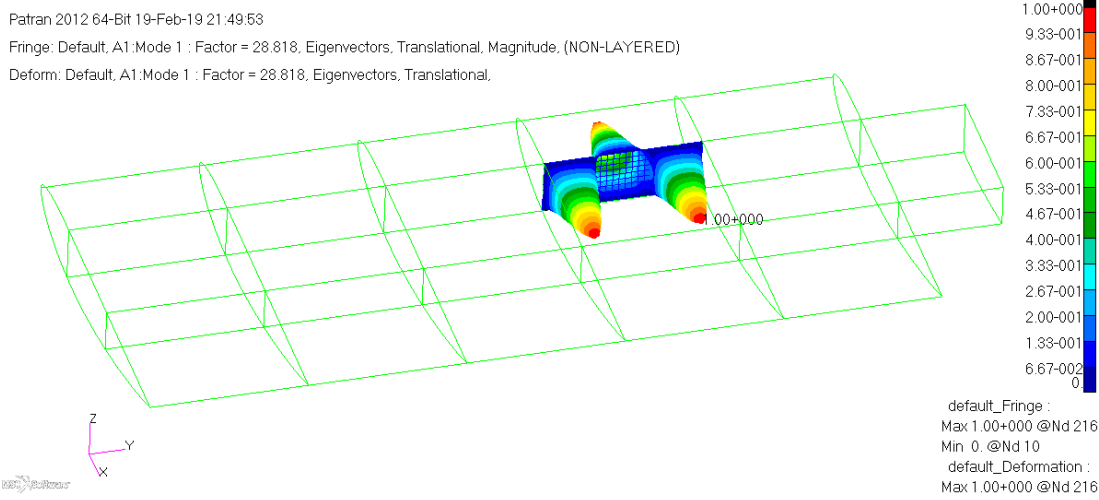


Figure 5.17: Buckling analysis result for the front spar 4th zone with the $[-45/90/90/45/45/0/0]_s$ stacking sequence

Then, for the same panel a and b values are taken, but they are used in the flat surface buckling equation given by Equation (5.2) and the variation of the critical buckling load with the m value is obtained and this variation is given in Figure 5.18.

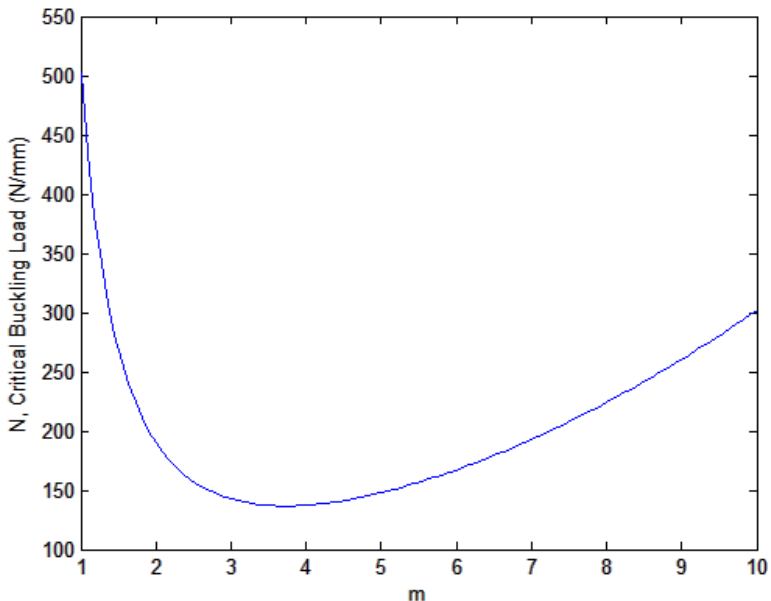


Figure 5.18: Variation of the critical buckling load with the m value for the front spar web in the 4th zone

From Figure 5.18, critical buckling load is determined as 136.73 N/mm which is way higher than the finite element analysis result.

This comparison approach is repeated for various design regions, and results are tabulated in Table 5.4. This table shows that for curved laminates and unbalanced laminates, Equation (5.2) cannot be used to approximate the critical buckling load and curvature of the laminates and the unbalanced laminate configuration significantly affects the critical load level to cause local buckling.

Table 5.4: Local buckling load comparison of NASTRAN and Equation (5.2) results for various design regions

	Stacking Sequence	Critical Buckling Load	
		Equation (5.2) [N/mm]	NASTRAN [N/mm]
Rear Spar Web 3 th Zone (flat panel)	[-45/90/45/45/0] _s	94.79	18.15
Upper Skin Middle 5 th Zone (curved panel)	[-45/-45/90/45/45/45/0] _s	29.25	5.44
Rib Middle 3 th Zone (flat panel)	[45/90/45/0/0] _s	55.06	12.6

Based on the analysis results presented so far, it is decided that the local buckling analysis of the skin panels can be performed by finite element analysis and using fine mesh. For every design region, local buckling analysis has to be done, and the calculated critical buckling load [N/mm] has to be given as stress constraint, which is calculated by dividing critical buckling load to thickness of that region. However, normally, stress constraints for local buckling should be known before the optimization, not afterwards. In addition, this constraint varies in each iteration, because during the optimization process laminate sequences and thicknesses change.

Therefore, a different approach needed to be used to include the local buckling constraint into the optimization process. For this aim, local buckling constraints for every design region could be calculated after an initial optimization has been performed, and the optimization could be started again utilizing the local buckling

constraint calculated in the previous optimization. Then, this process could be repeated until the optimization results converge.

In conclusion, in the present study, the described approach is used to include local buckling of wing regions in the optimization process. Firstly, an optimization with only strength constraint has been performed. Then, for every design region, a PATRAN model is created with a stacking sequence based on the result of previous optimization with only unit load and simply supported boundary conditions. Afterwards, buckling analysis is done and the critical buckling load is calculated. The critical buckling load is divided to the thickness that is calculated in the previous optimization, and the critical buckling stress is calculated. Then, this stress is used as the local buckling constraint for that region and next optimization is started using the stacking sequence which is the result of the previous optimization as the initial sequence. This process is repeated until mass change in every optimization becomes 0.1 kg as convergence criteria. Flowchart that is used for this process is given in Figure 5.19.

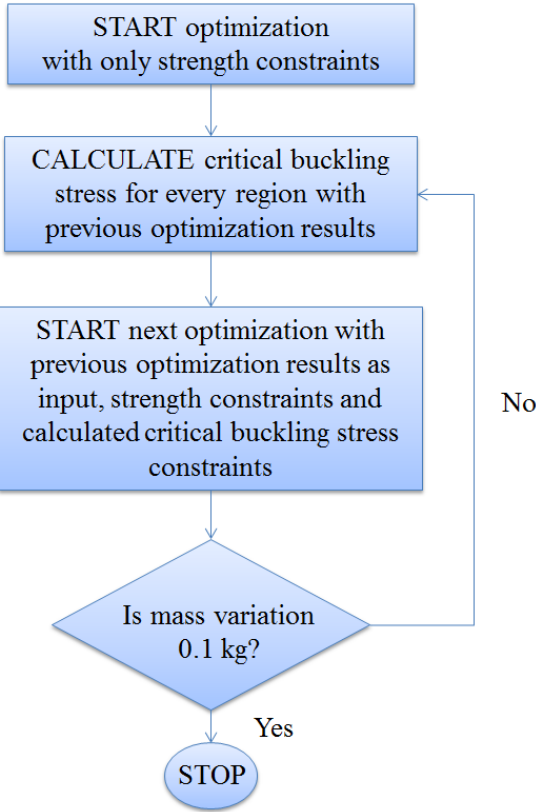


Figure 5.19: Implementation of the composite strength and local buckling constraints into the optimization process

Calculated local buckling constraints are given for average compression stresses in skins and ribs. In spars, local in-plane bending buckling should be constrained. So average compression stresses are calculated for lower line of spars because lower parts of spar webs capture compression as the nature of pressure disturbance that is used in this study, and calculated constraints given for them.

5.4.2.3. Thickness Constraints

As explained in the aluminum HTP optimization in Chapter 4.4.2.3, laminate thicknesses should be increased from tip to root of the horizontal tail plane. Therefore, to end up with expected laminate thickness variations along the span of the horizontal tail, thickness constraints are created in NASTRAN input file as design equations. For further information, these equations are written and explained in APPENDIX B. By creating equations, ply thickness summations are ordered from root to tip like aluminum HTP optimization as shown in Figure 4.12.

5.4.3. Objective Function of the Optimization

Objective function is same as the aluminum HTP optimization problem. Using the described design variables and constraints, the objective of the composite optimization problem is to reach the minimum weight of the structure.

5.5. Optimization Results

In the composite HTP optimization, there are three different mesh densities, which are identical with the aluminum HTP optimization as defined in Chapter 2.3, and two different constraints; only strength constraints, and local buckling and strength constraints together. In the optimization involving only the strength constraints, convergence criterion is NASTRAN SOL 200 solver's convergence criterion which is explained in Chapter 1.4. In local buckling and strength constraints together optimization, convergence criterion is explained in Chapter 5.4.2.2. In addition to these, there are two different design variable methods; thickness only, and thickness and fiber orientation angle together.

Figure 5.20 shows the optimization iterations for the Mesh 1 with the thickness as the only design variable and using strength constraint only. For this case, optimization stops in two iterations and the minimum mass is obtained as 5.1 kg for the HTP.

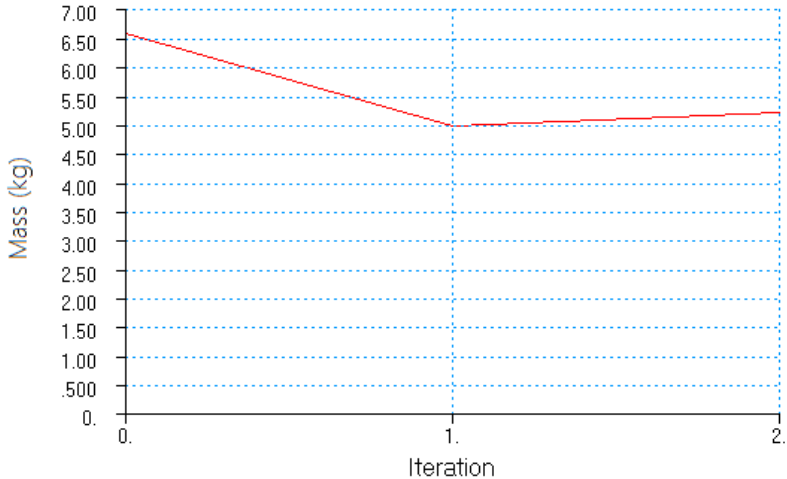


Figure 5.20: Optimization iterations for the Mesh 1 / Thickness as the only design variable / Strength constraint only

Optimum thickness variation for this case is shown in Figure 5.21 and 5.22. It is seen that thickness reduces from root to tip of the HTP by the virtue of the thickness constraints implemented.

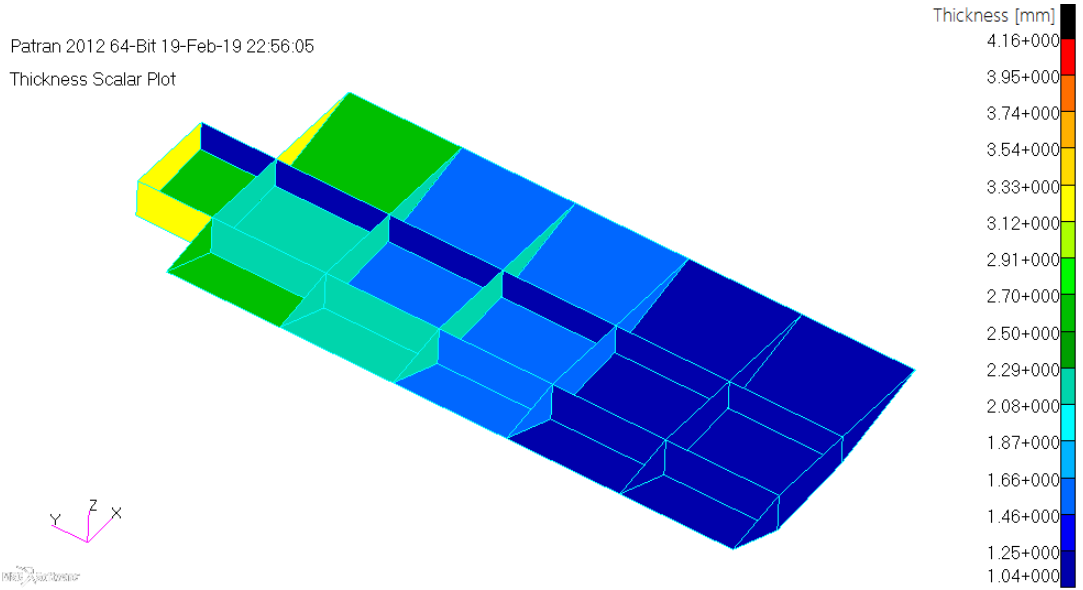


Figure 5.21: Optimum thickness variation for the Mesh 1 HTP without upper skin / Thickness as the only design variable / Strength constraint only

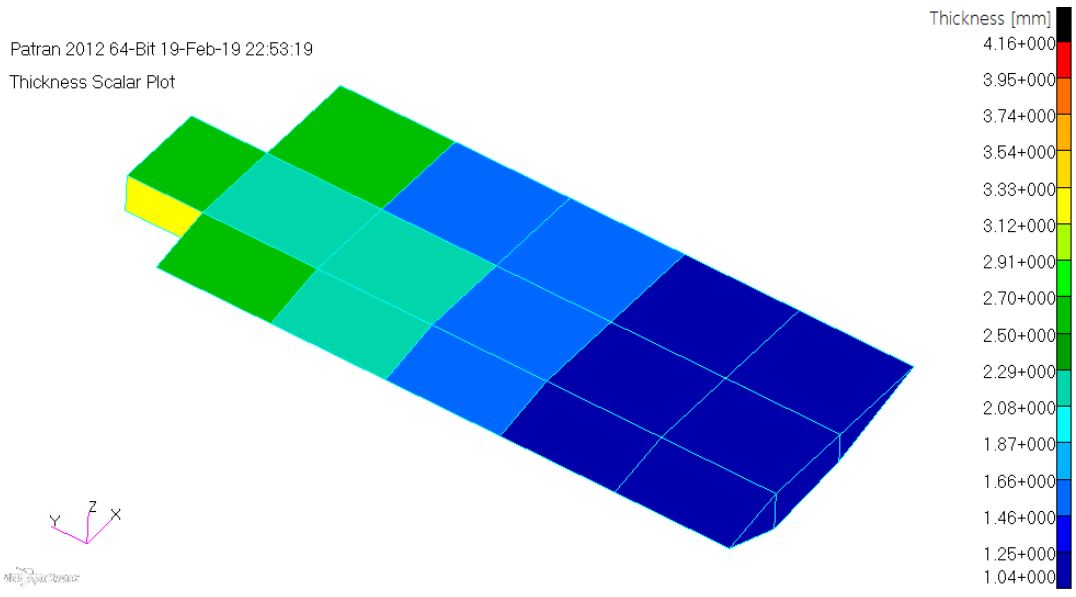


Figure 5.22: Optimum thickness variation for the Mesh 1 HTP with upper skin / Thickness as the only design variable / Strength constraint only

Figure 5.23 shows the optimization iterations for the Mesh 2 with the thickness as the only design variable and using strength constraint only. For this case, optimization stops in two iterations and the minimum mass is obtained as 5.19 kg for the HTP.

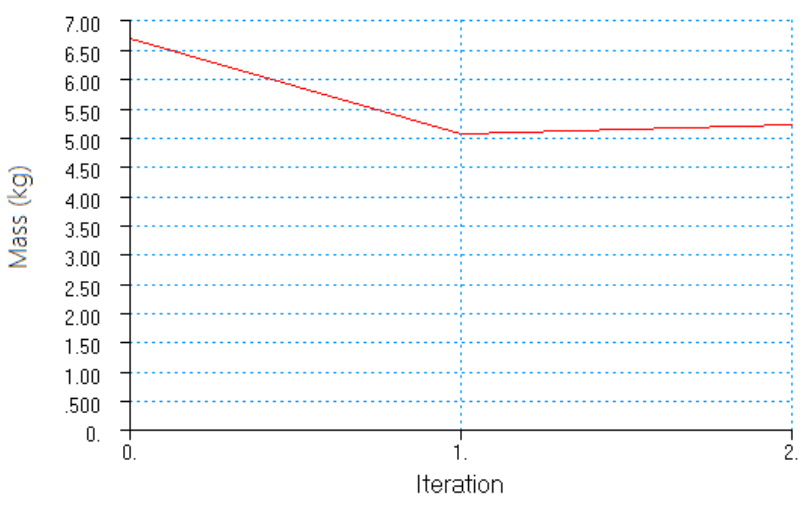


Figure 5.23: Optimization iterations for the Mesh 2 / Thickness as the only design variable / Strength constraint only

Optimum thickness variation for this case is shown in Figure 5.24 and 5.25. Again, thicknesses reduce from root to tip of the HTP.

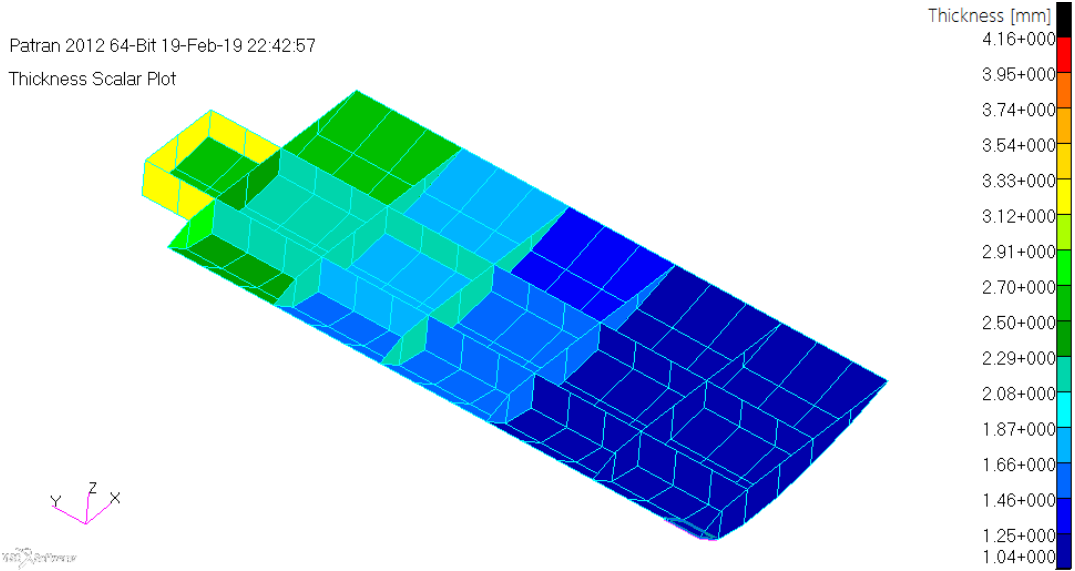


Figure 5.24: Optimum thickness variation for the Mesh 2 HTP without upper skin / Thickness as the only design variable / Strength constraint only

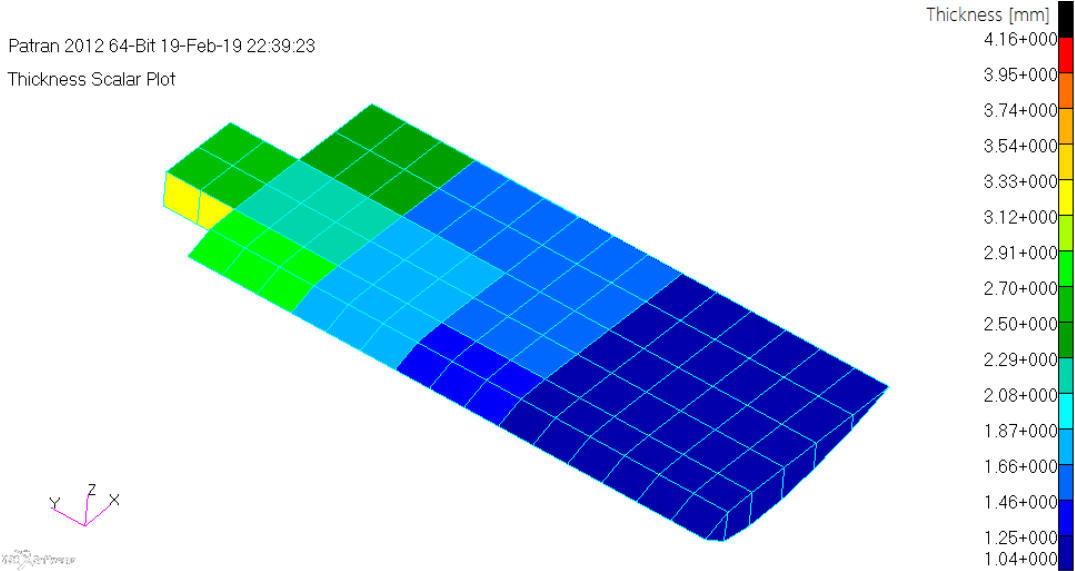


Figure 5.25: Optimum thickness variation for the Mesh 2 HTP with upper skin / Thickness as the only design variable / Strength constraint only

Figure 5.26 shows the optimization iterations for the Mesh 3 with the thickness as the only design variable and using strength constraint only. For this case, optimization stops in two iterations and the minimum mass is obtained as 5.31 kg for the HTP.

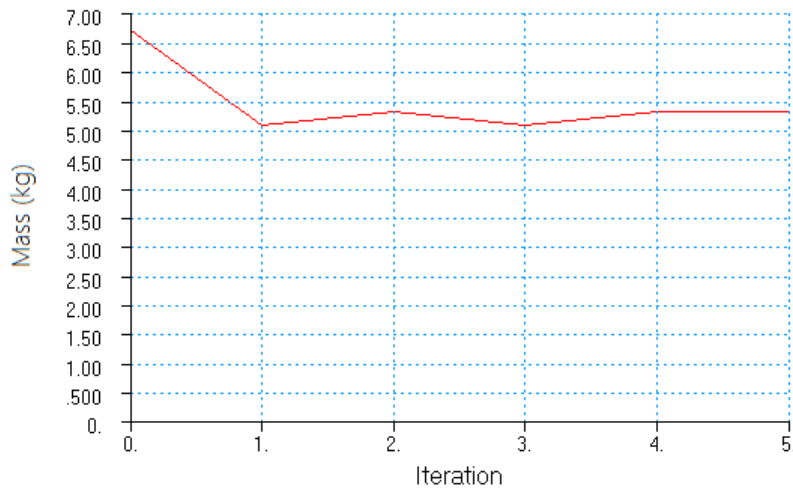


Figure 5.26: Optimization iterations for the Mesh 3 / Thickness as the only design variable / Strength constraint only

Optimum thickness variation for this case is shown in Figure 5.27 and 5.28. As planned in Chapter 5.4.2.3, thickness reduces smoothly span wise.

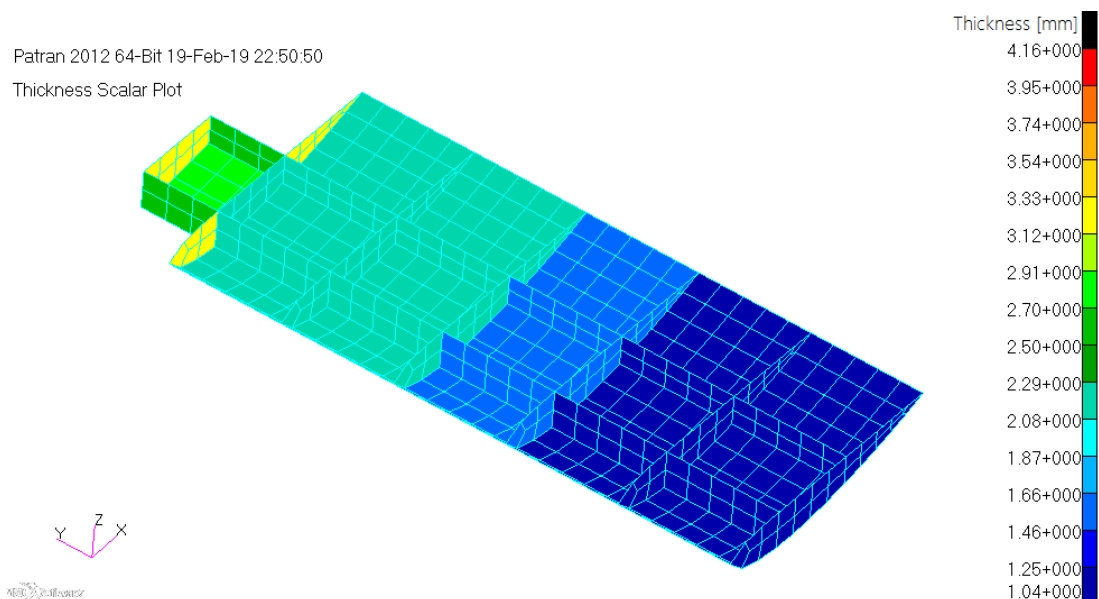


Figure 5.27: Optimum thickness variation for the Mesh 3 HTP without upper skin / Thickness as the only design variable / Strength constraint only

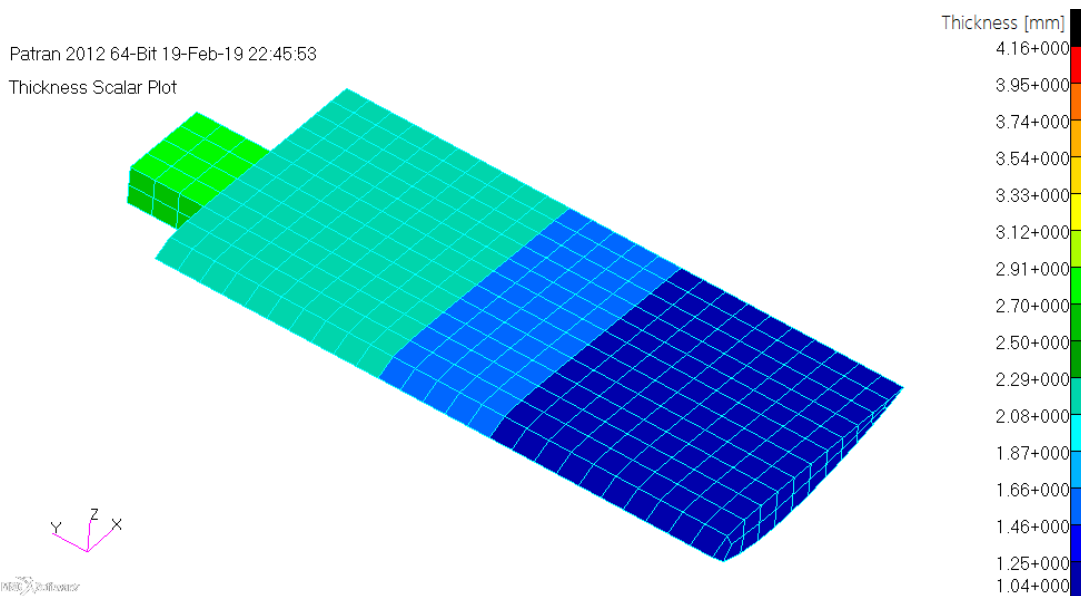


Figure 5.28: Optimum thickness variation for the Mesh 3 HTP with upper skin /
Thickness as the only design variable / Strength constraint only

In the second level of optimization, optimization results of the thickness optimization are used as the initial values for the thickness design variables, and thickness and fiber orientation angle are used together as design variables using strength constraint only in the optimization process.

Figure 5.29 shows the optimization iterations for the Mesh 1 with the thickness and fiber orientation angle as the design variables and using strength constraint only. For this case, optimization stops in ten iterations and the minimum mass is obtained as 4.9 kg for the HTP.

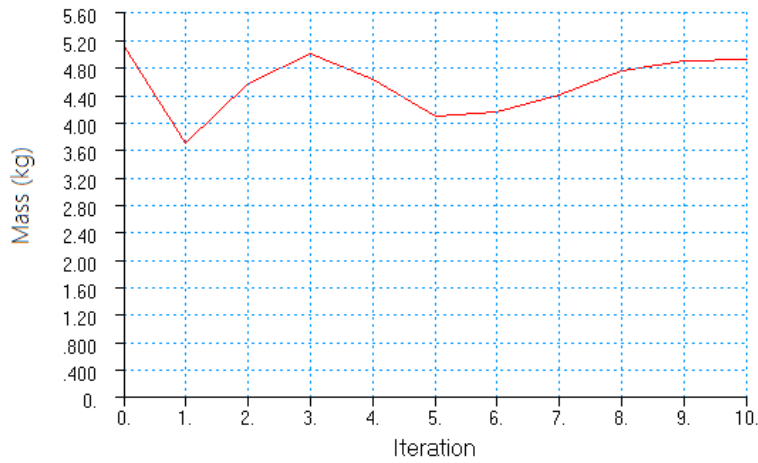


Figure 5.29: Optimization iterations for the Mesh 1 / Thickness and fiber orientation angle as design variables / Strength constraint only

Optimum thickness variation for this case is shown in Figure 5.30 and 5.31. Optimum stacking sequences obtained as a result of the optimization is reported in Appendix E.

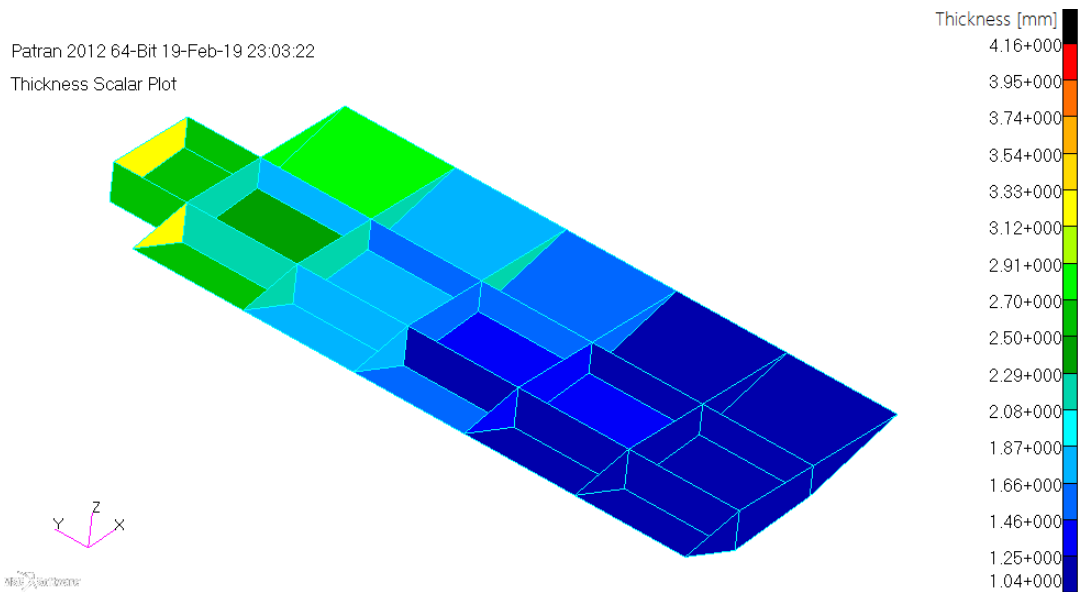


Figure 5.30: Optimum thickness variation for the Mesh 1 HTP without upper skin / Thickness and fiber orientation angle as design variables / Strength constraint only

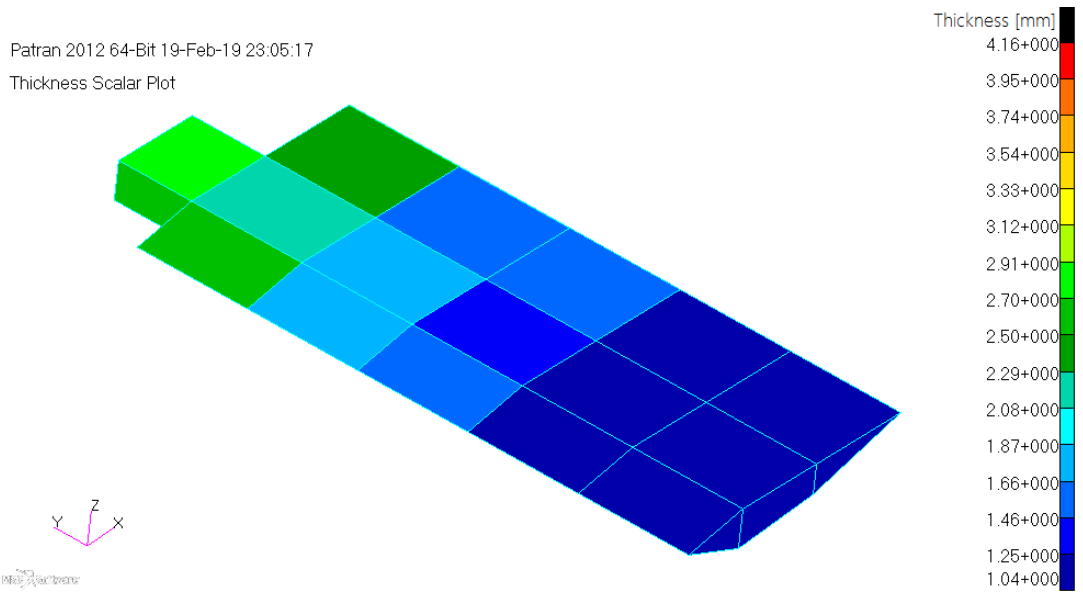


Figure 5.31: Optimum thickness variation for the Mesh 1 HTP with upper skin / Thickness and fiber orientation angle as design variables / Strength constraint only

Figure 5.32 shows the optimization iterations for the Mesh 2 with the thickness and fiber orientation angle as the design variables and using strength constraint only. For this case, optimization stops in ten iterations and the minimum mass is obtained as 5.10 kg for the HTP.

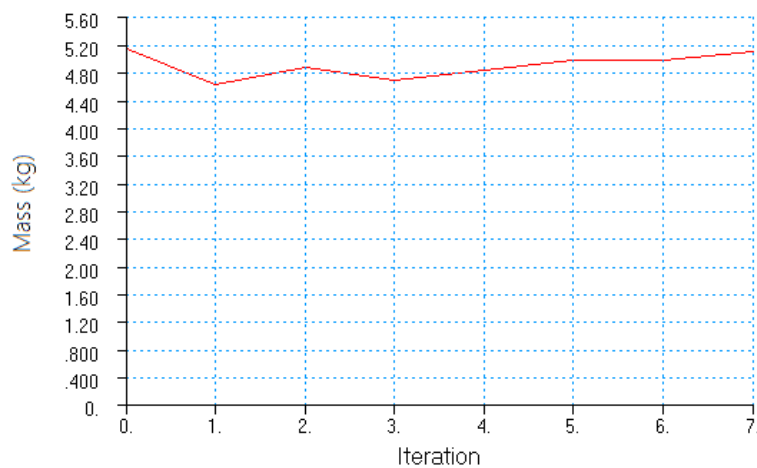


Figure 5.32: Optimization iterations for the Mesh 2 / Thickness and fiber orientation angle as design variables / Strength constraint only

Optimum thickness variation for this case is shown in Figure 5.33 and 5.34.

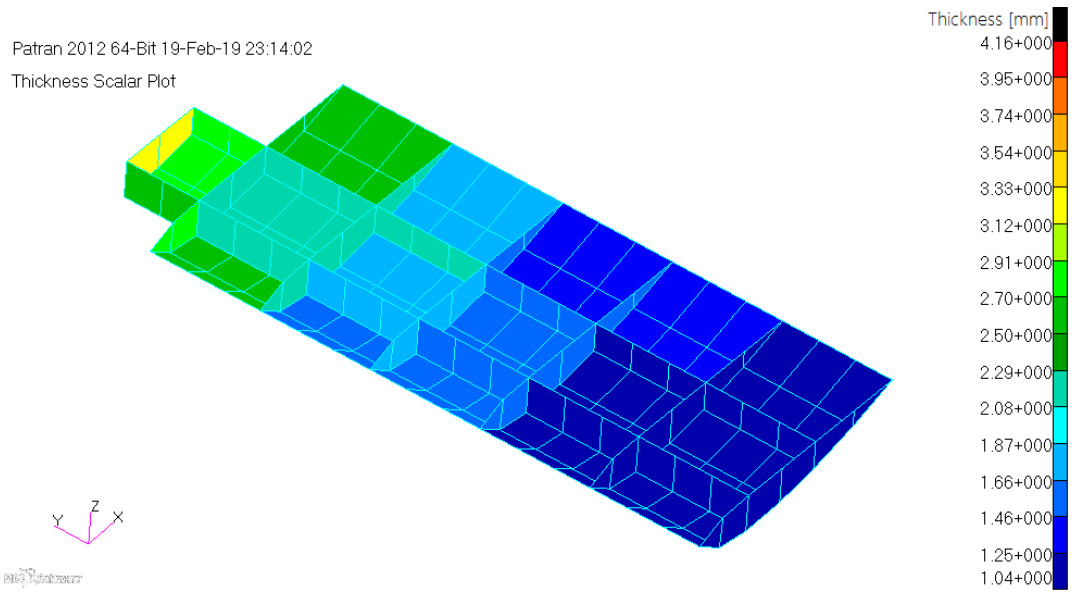


Figure 5.33: Optimum thickness variation for the Mesh 2 HTP without upper skin / Thickness and fiber orientation angle as design variables / Strength constraint only

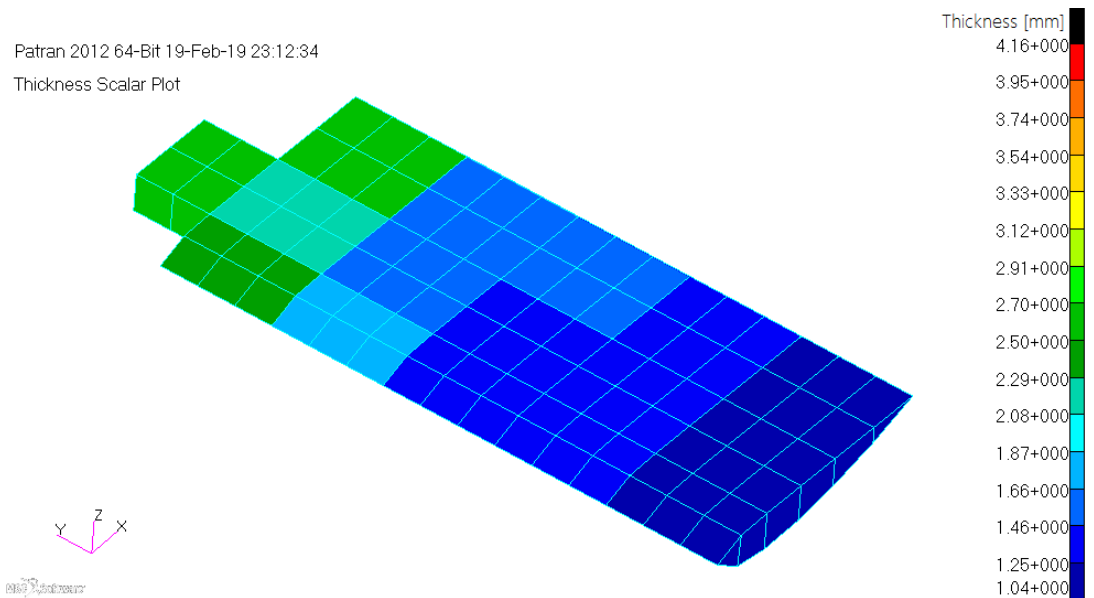


Figure 5.34: Optimum thickness variation for the Mesh 2 HTP with upper skin / Thickness and fiber orientation angle as design variables / Strength constraint only

Figure 5.35 shows the optimization iterations for the Mesh 3 with the thickness and fiber orientation angle as the design variables and using strength constraint only. For this case, optimization stops in ten iterations and the minimum mass is obtained as 5.17 kg for the HTP.

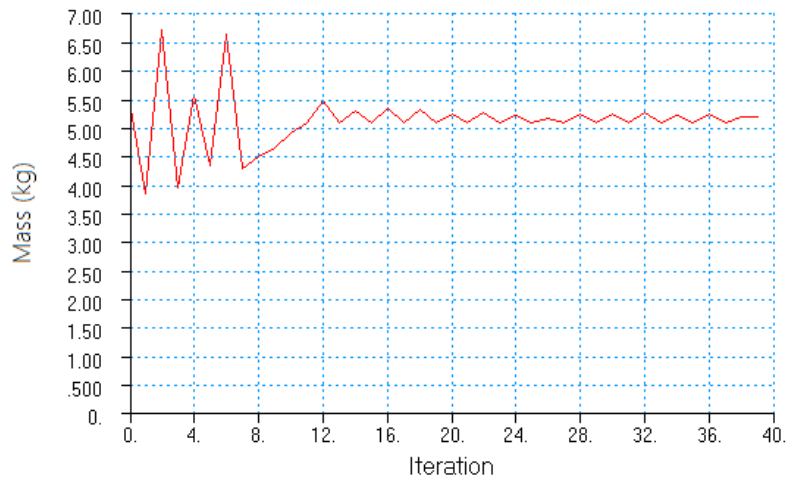


Figure 5.35: Optimization iterations for the Mesh 3 /Thickness and fiber orientation angle as design variables / Strength constraint only

Optimum thickness variation for this case is shown in Figure 5.36 and 5.37.

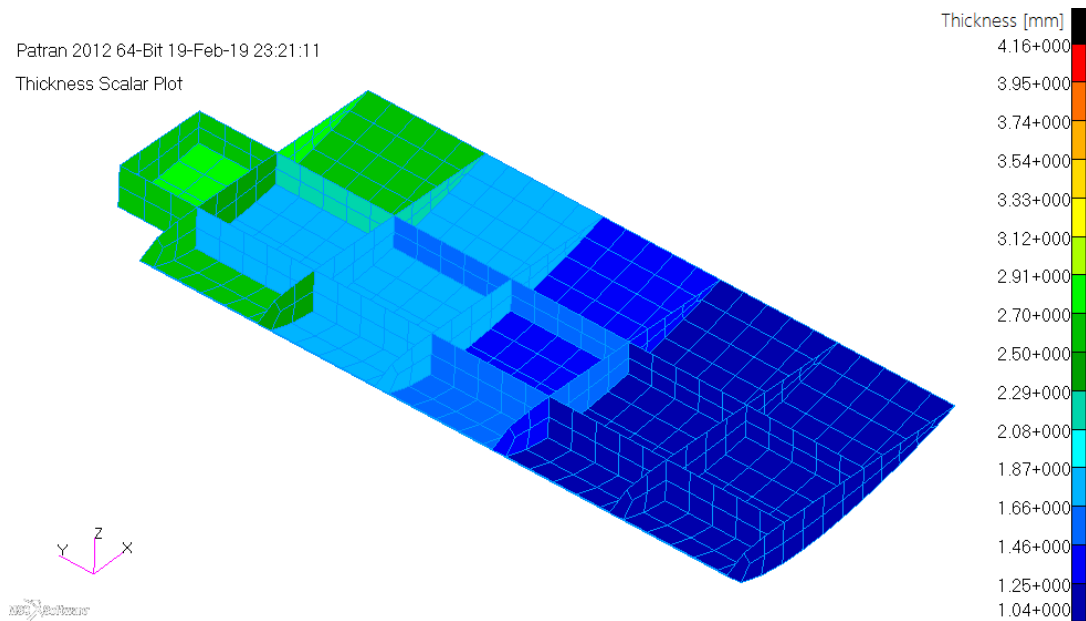


Figure 5.36: Optimum thickness variation for the Mesh 3 HTP without upper skin / Thickness and fiber orientation angle as design variables / Strength constraint only

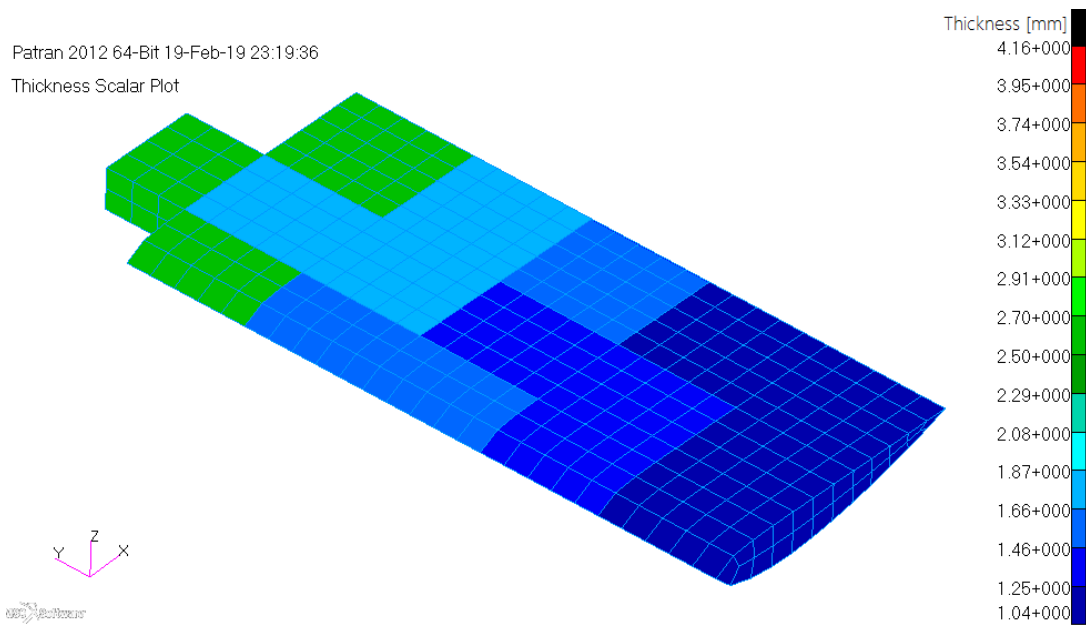


Figure 5.37: Optimum thickness variation for the Mesh 3 HTP with upper skin / Thickness and fiber orientation angle as design variables / Strength constraint only

Optimization results obtained from two different optimizations, which are with only thickness as design variables, and the thickness plus fiber orientation angle as design variables, are presented in Table 5.5.

Table 5.5: Optimization results for the strength constraint only with discrete design variables

MESH SIZE	ONLY THICKNESS OPTIMIZATION	THICKNESS + FIBER ORIENTATION OPTIMIZATION
MESH 1	5.10 kg	4.90 kg
MESH 2	5.20 kg	5.10 kg
MESH 3	5.31 kg	5.17 kg

Table 5.5 shows that as the mesh density is made finer, mass obtained by optimizations slightly increases since the Mesh 3 captures the stress gradients better and higher average stress occurs in the design zones. Figures 5.38 – 5.40 show the average y-direction normal stress in the skins of the HTP for the three different mesh densities. In these plots average stress of the 8 layers in HTP skins are shown. Average stress plots clearly show that, as the mesh becomes finer, average stress increases.

Patran 2012 64-Bit 20-Feb-19 00:01:05

Fringe: Default, Static Subcase:D 1, Stress Tensor, , Y Component, 8 of 8 layers (Average)

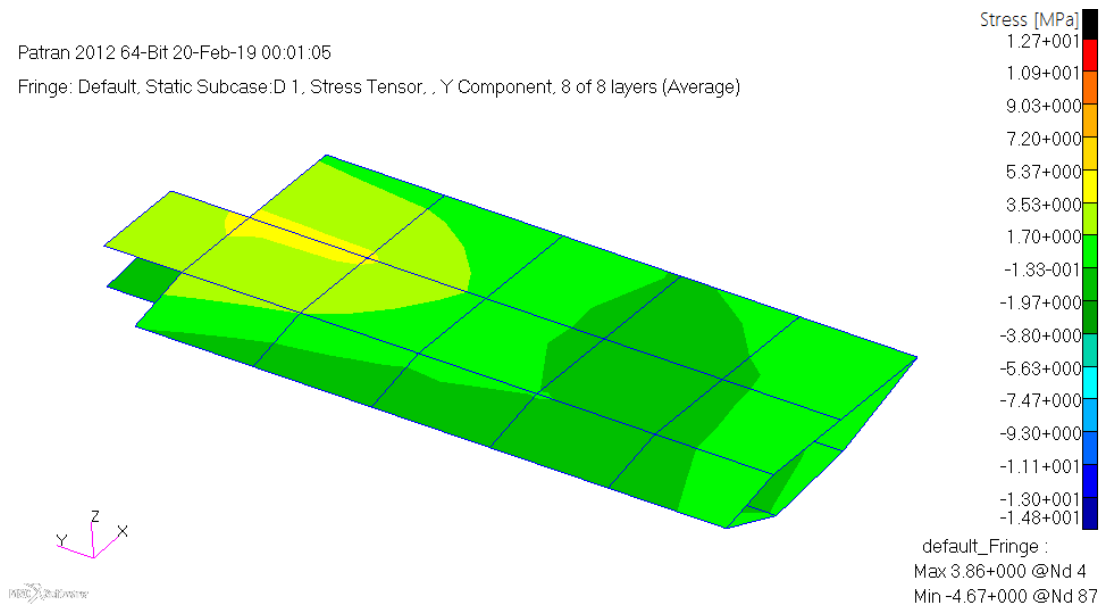


Figure 5.38: Average stress distribution for the Mesh 1 HTP in 1st iteration / Thickness and fiber orientation angle as design variables / Strength constraint only

Patran 2012 64-Bit 19-Feb-19 23:49:42

Fringe: Default, Static Subcase:D 1, Stress Tensor, , Y Component, 8 of 8 layers (Average)

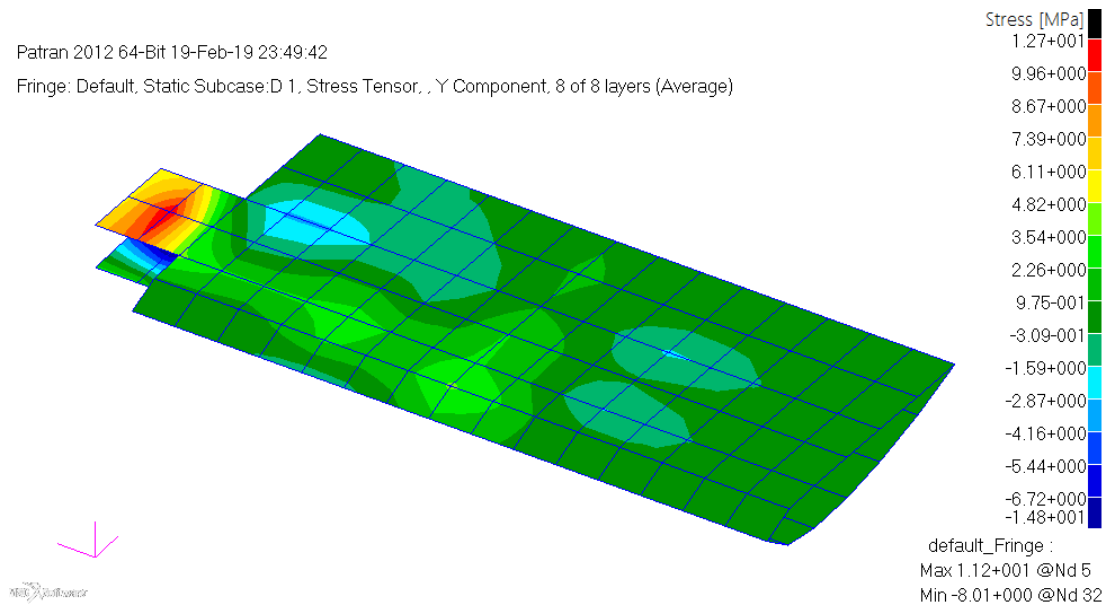


Figure 5.39: Average stress distribution for the Mesh 2 HTP in 1st iteration / Thickness and fiber orientation angle as design variables / Strength constraint only

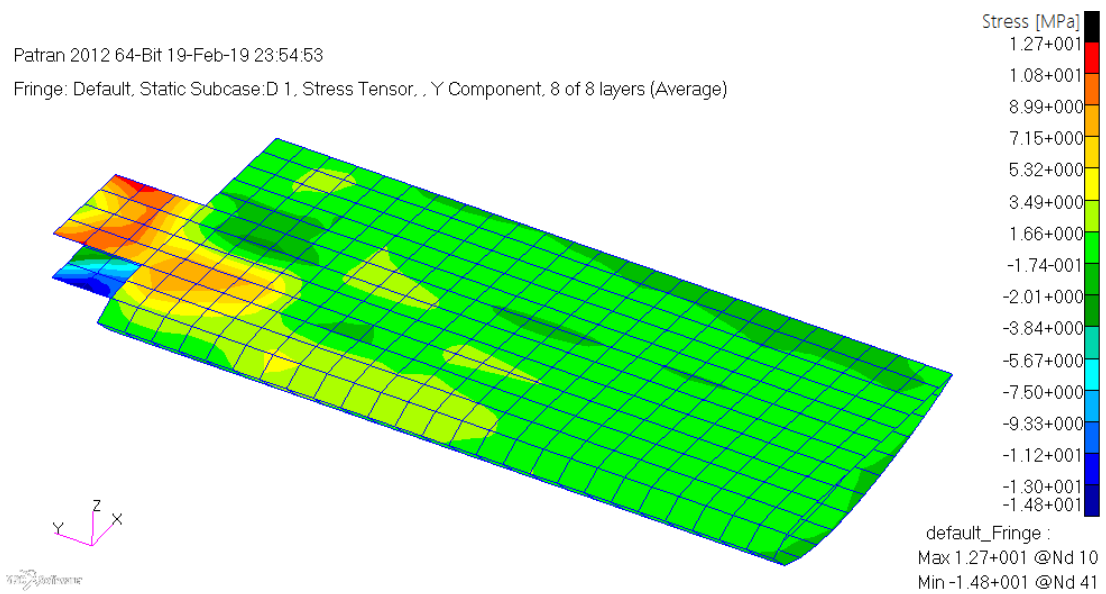


Figure 5.40: Average stress distribution for the Mesh 3 HTP in 1st iteration / Thickness and fiber orientation angle as design variables / Strength constraint only

Moreover, when the fiber orientation angle is added as the additional design variable, slightly lower optimum mass values are obtained. However, since the difference between the optimum HTP mass obtained as a result of the optimization runs utilizing the thickness and the thickness plus the fiber orientation angle as the design variables is very low, one can comment that fiber orientation angle is not very effective on optimum configuration when strength constraint is used as the sole constraint of the optimization problem.

In addition to the strength constraints, when local buckling constraint is also added to the definition of the optimization problem, instead of optimization iterations, mass versus optimization number variation should be traced to see the convergence behavior. For the Mesh 3 case, Figure 5.41 shows the mass versus optimization number plot when the thicknesses are used as the only design variable.

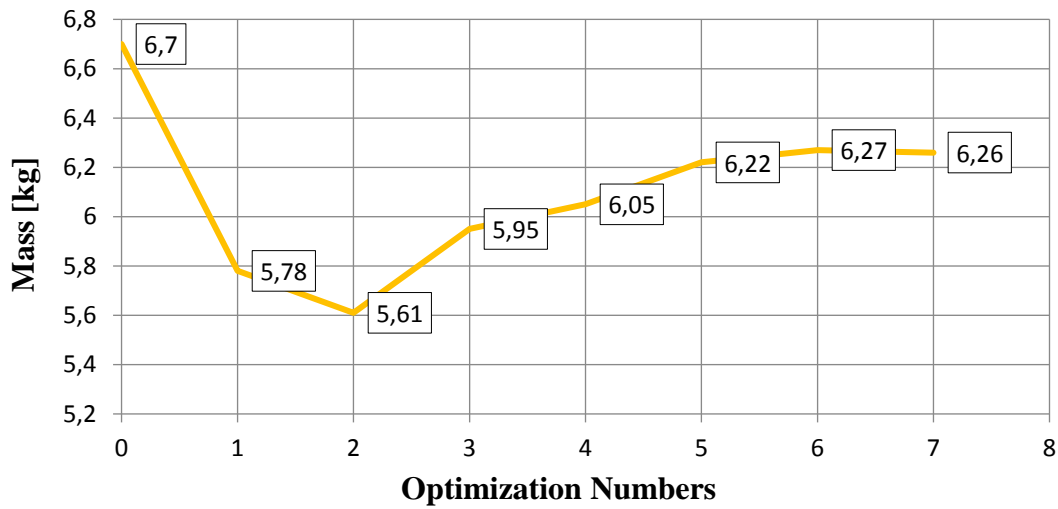


Figure 5.41: Optimization results for the Mesh 3 / Thickness as the only design variable / Strength and local buckling constraints

As it is explained before, optimization is terminated when the mass converges to a value as seen in Figure 5.41. It is seen that after six separate optimizations, variations in the mass is 0.1 kg at the seventh optimization, so calculations for local buckling constraints are terminated. When the thickness is used as the only design variable, optimum mass is obtained as 6.26 kg. Optimum thickness variation for this case is shown in Figure 5.42 and 5.43.

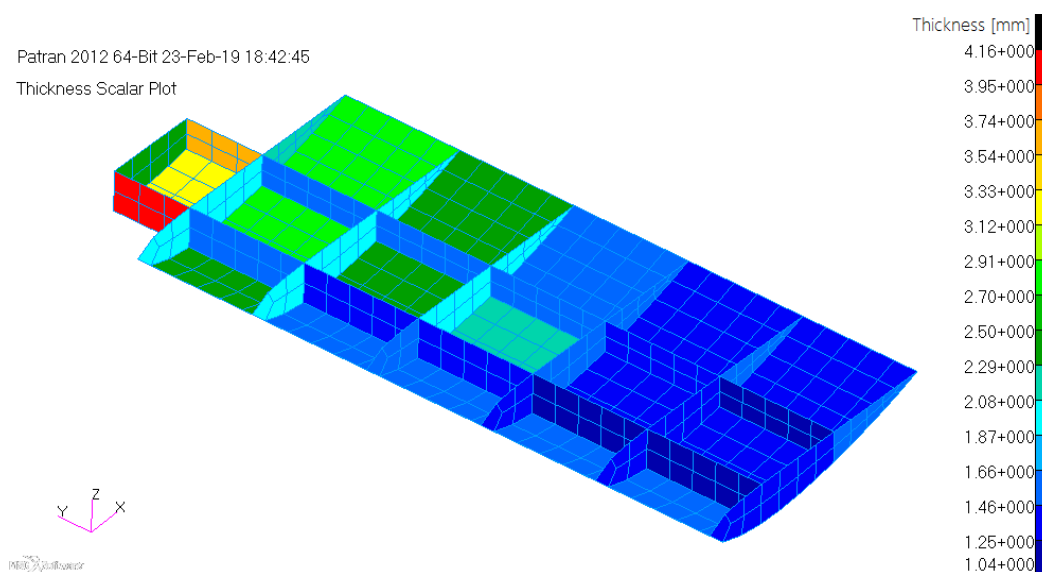


Figure 5.42: Optimum thickness variation for the Mesh 3 HTP without upper skin / Thickness as the only design variable / Strength and local buckling constraints

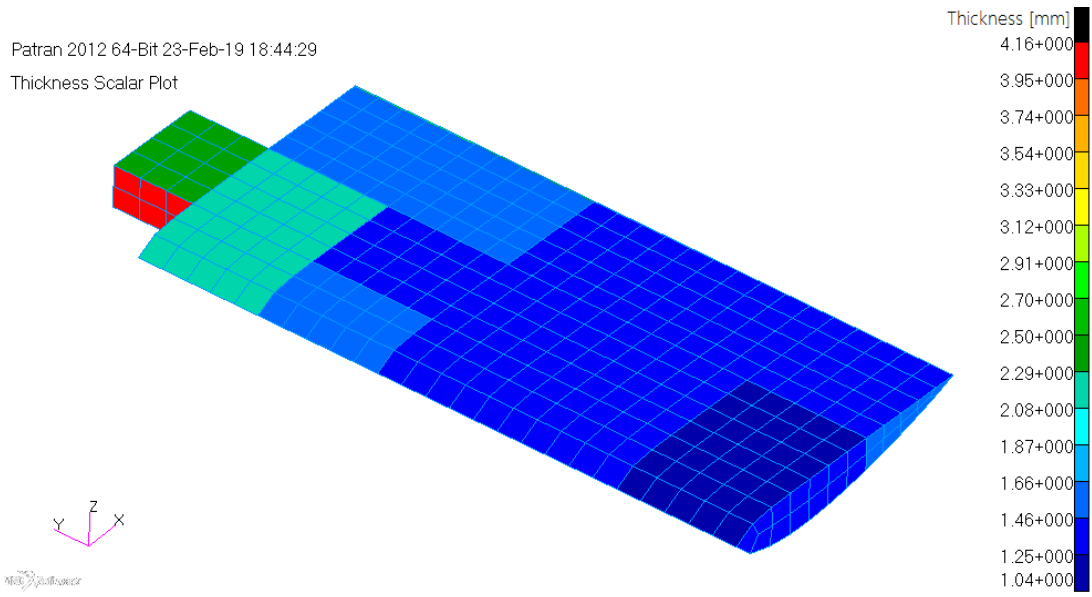


Figure 5.43: Optimum thickness variation for the Mesh 3 HTP with upper skin / Thickness as the only design variable / Strength and local buckling constraints

Following the thickness optimization, the second level of optimization is invoked by adding the fiber orientation angle as the other design variable.

For the Mesh 3 case, Figure 5.44 shows the mass versus optimization number plot when the thicknesses and the fiber orientation angles are used as the design variables.

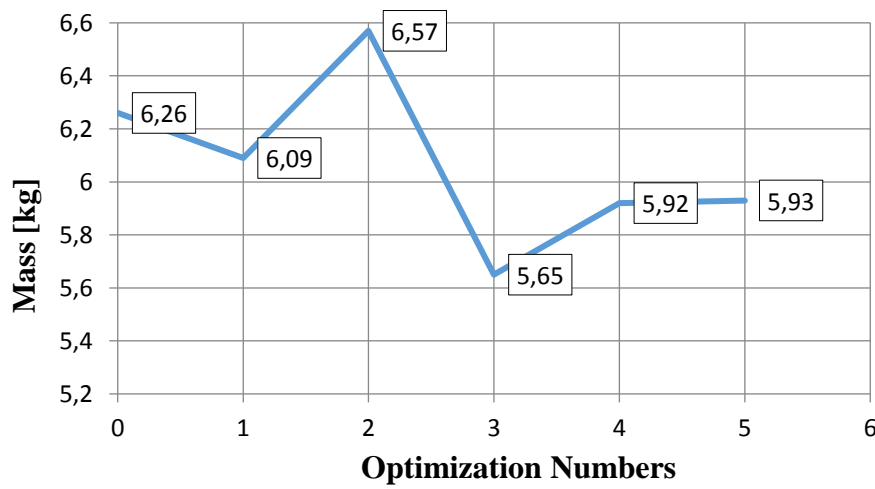


Figure 5.44: Optimization results for the Mesh 3 / Thickness and fiber orientation angle as design variables / Strength and local buckling constraints

In this case, optimization is terminated since convergence has been achieved. Optimum mass is obtained as 5.93 kg that is 0.33 kg lighter compared to the optimum mass obtained using thickness as the only design variable. Optimum thickness variation for this case is shown in Figures 5.45 and 5.46. It is seen that thickness reduces span wise as planned through the inclusion of thickness constraints. Optimum stacking sequences obtained as the result of the optimization are reported in Appendix E.

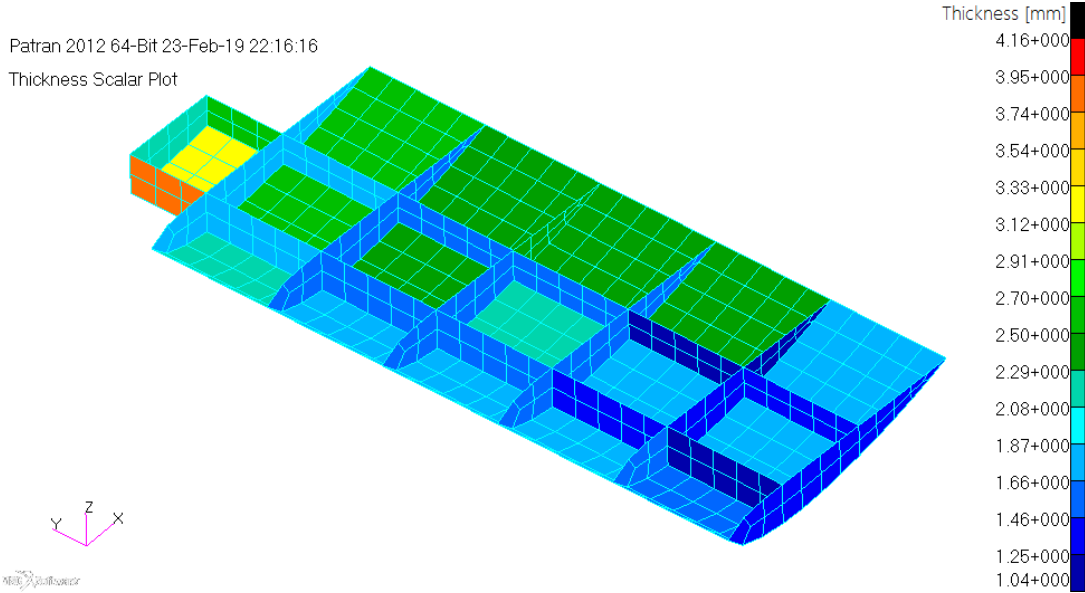


Figure 5.45: Optimum thickness variation for the Mesh 3 HTP without upper skin / Thickness and fiber orientation angle as design variables / Strength and local buckling constraints

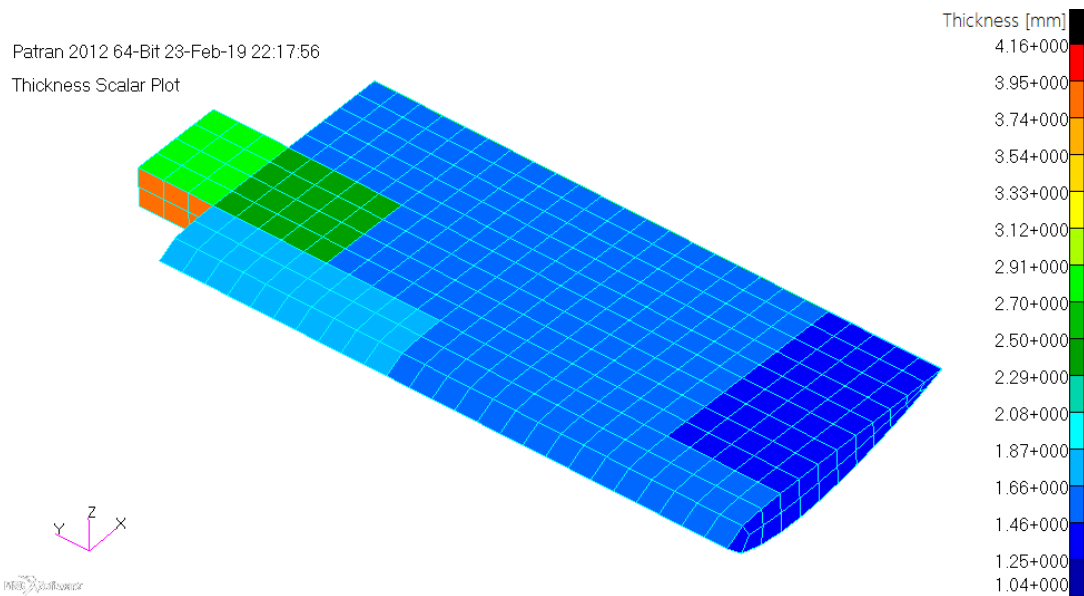


Figure 5.46: Optimum thickness variation for the Mesh 3 HTP with upper skin / Thickness and fiber orientation angle as design variables / Strength and local buckling constraints

Combined optimization history is given in Figure 5.47 where the orange line shows the mass history when thickness is used as the only design variable and the blue line shows the mass history when the thickness and the fiber orientation angles are used together as the design variables.

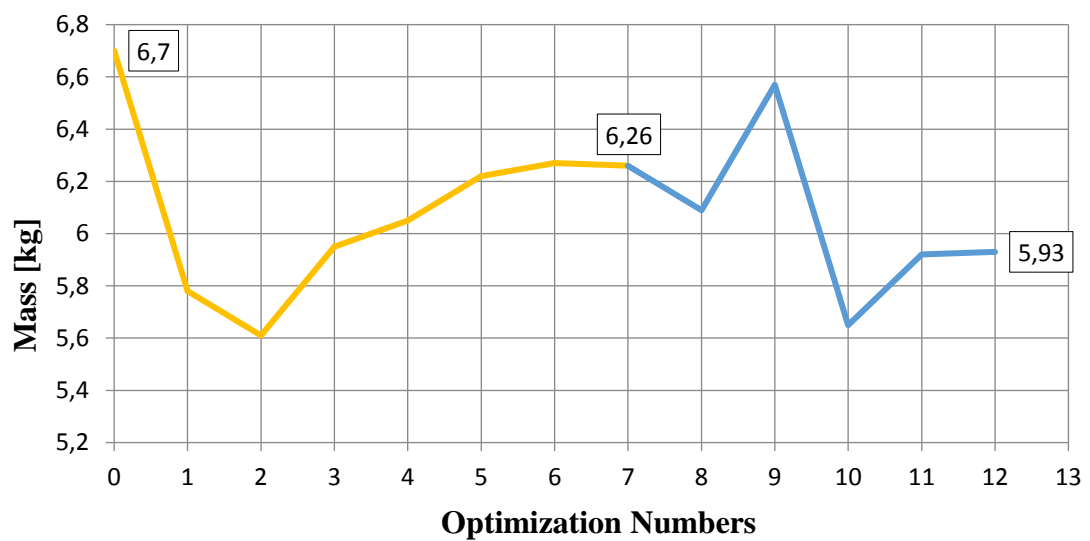


Figure 5.47: Combined optimization results for the Mesh 3 / Strength and local buckling constraints

It is noted that when local buckling constraint is added to the constraints, fiber orientation angle design variable becomes more effective on the optimum mass compared its effect when only strength constraint is employed in the optimization process. This is reasonable because fiber orientation angle changes the stiffness of the HTP panels and in turn the critical buckling stress.

CHAPTER 6

BENCHMARKING OF ALUMINIUM AND COMPOSITE MATERIALS AND COMPARISON OF OPTIMIZATION RESULTS

6.1. Introduction

Composites and aluminum have advantages and disadvantages. In this chapter, these pros and cons are discussed and at the end of the chapter optimization results obtained for the same mesh density and similar constraints are compared.

6.2. Advantages of Composites and Aluminum

Aluminum and composite materials play major roles in the aerospace industry. Aluminum is an overwhelming choice in aerospace industry for more than 80 years because of their well-known characteristics and production methods. For primary structures, critical fittings and supports, they are still widely used.

Aluminum is a lightweight material when compared to other metals. Unlike composites, aluminum is isotropic, which ensures the same properties in every direction. Aluminum is technically advanced in terms of forming and alloying. Some aluminum alloys are further strengthened and hardened by heat treatments. In addition, they are relatively low cost materials when compared to composites.

Aluminum alloys are used as electric conductors because of their high electrical conductivity. This is a plus when a lightning strike occurs.

Aluminum is not a brittle material; therefore, they are useful for out of plane loads such as bird impact.

Aluminum parts have more reliable inspection techniques and low cost repair and maintenance.

Nowadays, increasing composite parts' ratio is a new trend for aircraft structures. The most important design property of carbon composites is their high strength to weight and stiffness to weight ratios. With proper selection and placements of fibers, composites can be stronger, stiffer and lighter than aluminum parts.

Composites are excellent in highly tension-loaded applications and they absorb vibration more than aluminum. This helps decrease fatigue failure and maintenance cost. Therefore, they have a long life and they are durable. Composites are also very corrosion resistance when compared to aluminum parts.

Composites can be molded into complicated shapes more easily than most other materials. This gives the designers freedom to create almost any shape or form. In addition, with composites one can produce one-piece designs. Fabricating a product in one piece, or decreasing the number of parts in a component reduces the design, production and maintenance time. Furthermore, they require fewer fasteners.

The absence of electric conductivity makes composites electronic transparent which means that antennas could be kept inside of aircraft. They are usually radar transparent.

6.3. Disadvantages of Composites and Aluminum

Aluminum structures could be heavier than composite structures. Some parts cannot be produced with aluminum material because of their geometries while they could be produced with composite material. Because of that, they require more than one part apart from composites, and this situation result with more fasteners in structure also.

In highly tension loaded applications, aluminum is weaker then composites. This finding could also be made when tension strength limits of materials are compared.

Composite materials are relatively brittle like most stiff materials. They have no yield behavior, and resistance to impact is low.

Composite material properties are very dependent on the production quality whereas not so much for the aluminum. If they are produced with false production methods or wrong conditions, they cannot work as desired and that could be catastrophic. The fabrication process is usually labor intensive and complex, which further increases the cost.

Composites need extra plies for various situations. They need isolation to prevent the adjacent aluminum part from galvanic corrosion. Bronze mesh is required to conduct static current or lightning current. Since composites are often constructed by stacking different number of layers into a laminate structure, delamination may occur between the layers.

Composites' damage inspection is very hard. Delamination and cracks in composites are mostly internal and hence require complicated inspection techniques for detection.

Composites have higher material costs, and very expensive repair and maintenance costs.

6.4. Comparison of Optimization Results for the Aluminum and Composite HTP

In composite optimization, Mesh 3 had to be used for local buckling constraints and only discrete variables are used because of the nature of composites. Therefore, analysis results of the Mesh 3 finite element model with strength and local buckling constraints and discrete design variables are compared for the aluminum and the composite HTP.

In the aluminum HTP optimization, there are three different starting masses for three different initial values of the design variables. Hence, initial masses are 2.52 kg, 16.06 kg and 29.59 kg for the minimum, middle, and maximum initial values of the design variables, respectively. Optimum weight solutions determined using the

minimum, middle and maximum initial values of the design variable inputs are 7.21 kg, 7.99 kg and 8.39 kg as respectively. Their arithmetic mean is 7.86 kg, but the optimum mass is 7.21 kg that is obtained using the minimum initial values of the design variables, so this value is compared with the optimum mass obtained for the composite HTP optimization.

In the composite HTP optimization, optimum mass is determined using the ply thickness and fiber orientation angle design variables together utilizing both strength and local buckling constraints. Starting mass for the composite HTP optimization was 6.7 kg and optimization result was 5.93 kg.

Figure 6.1 compares the optimization history for the aluminum and composite HTP optimization. For the aluminum optimization, from continuous and discrete design iterations, only the discrete iteration values are used to produce the plot given in Figure 6.1.

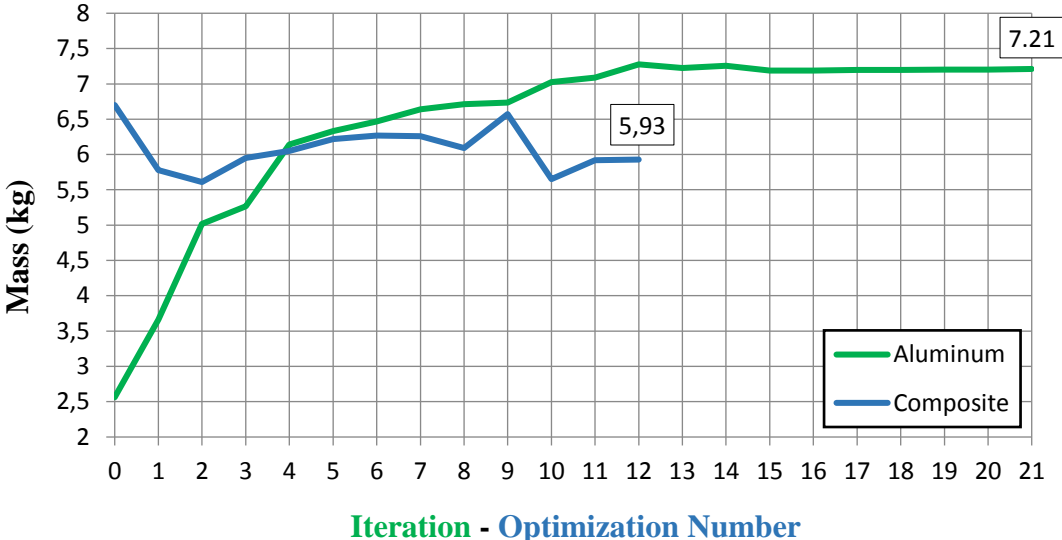


Figure 6.1: Comparison of optimization results for aluminum and composite HTP

In conclusion, optimized composite HTP structure is 1.28 kg lighter than the optimized aluminum HTP structure with chosen material properties, design variables and constraints. This mass reduction amounts to 17.75% weight reduction which is significant in aerospace structures.

CHAPTER 7

CONCLUSION

7.1. General Conclusion

In the aerospace industry, structural design processes usually take quite a long time. Because of this reason, starting a design by using near optimum dimensions in the analysis process is timesaving manner to reach an optimum structure. As shown in the present study, if optimization is incorporated early in the design phase, not only weight saving can be achieved but also the dimensions determined could be used as the initial values to be used in the detailed design phase. It should be noted that the application of present optimization study should only be considered in the preliminary design phase, not in the detailed design phase.

In the aluminum HTP optimization, it is observed that the strength constraint itself is not solely enough to size the horizontal tail plane. Depending on the mesh densities, mass values obtained from optimization results are in between 2.6 – 2.8 kg for the continuous design variable case and these figures could be accepted as very low figures. However, after adding the local buckling constraints to the strength constraints, and by utilizing discrete design variables, as would be the case in a real application, it is seen that optimum HTP mass is 7.21 kg for the Mesh 3 finite element model. These results clearly show that local buckling constraint is more influential on the sizing of the HTP structure, as expected. Moreover, with the use of discrete design variables, standard stock sizes of aluminum material can be chosen, and this causes increase in the final optimum weight since the resolution is coarse.

The present study also showed that optimum mass is affected by the mesh size. For example, when design variables start from the minimum values, 6.17 kg, 6.58 kg and 7.21 kg optimum mass results are achieved for Mesh 1, 2 and 3 respectively. These results show that optimum weight result obtained from optimizations increases without convergence. This could be acceptable considering that this study was done only for the preliminary design phase, as pointed out before. In addition, when the mesh density increases, stress gradients are captured better and this situation causes slight increase in the optimum mass values. Hence, in the benchmarking study, Mesh 3 results are compared for the aluminum and the composite HTP.

For the optimization of both the aluminum and the composite HTP, optimization results obtained by utilizing the strength and the local buckling constraints are used in the benchmarking study of the HTPs.

In the aluminum optimization, three different initial values are used for the design variables. Initial values are selected close to the lower and upper limits of the design variables and also from the middle of lower and upper limits. Results showed that consequently final mass values obtained from optimizations turn out to be close to each other, and when the initial values are selected from the lower limits of the design variables, the lowest HTP masses are obtained.

In the composite optimization, because of the nature of the laminates, only discrete design variables are used. Moreover, since the aluminum HTP optimization study has revealed that minimum HTP mass is obtained when the initial values of the design variables are selected as the lower limits of the design variables, in the composite HTP optimization lower limit of the ply thicknesses are used as the initial values of the design variables. It is noted that by adding fiber orientation angle to the design variables on top of the thickness design variables, optimum HTP mass can be reduced even further. For instance, in the Mesh 3 density, HTP with strength and local buckling constraints together, while using only the ply thickness variable results in an optimum mass of 6.26 kg, by adding the fiber orientation angle as the design variable, optimum HTP mass reduces to 5.93 kg. The reduction in the mass value is approximately 5.3% when fiber orientation angles are added to the design variable list.

It should be noted that in the present study, fiber orientation angles are selected from the discrete values of $\pm 45^\circ$, 0° and 90° . If the fiber orientation angle were made to vary continuously, higher reduction in the optimum HTP mass could have been obtained. This study has shown that fiber orientation angle is an additional design variable which is at the disposal of the designer, and it can be exploited to further improve the design, something which is not possible for structures made of isotropic materials.

It is a known fact that aluminum and composite materials are frequently used in aerospace structures, and each has advantages and disadvantages respectively when compared with each other. However when it comes to optimizing structures, it is clear that composites have more to offer. In this study, with similar design constraints and aerodynamic loads, optimum composite HTP is obtained as approximately 18% lighter than the optimum aluminum HTP.

7.2. Recommendation for Future Work

For the aluminum optimization, spar flanges are modeled as 1D rod. As an improvement for further studies, spar flanges can be modeled as beams, hence design variables could be extended. In addition, in this study for design variables having flanges, flange areas are kept as same. As a future study, flange areas could be different for every flange of a web.

For the composite optimization, calculation method of local buckling constraint used in this work is quite time consuming. If this method to be used, a code that would modify the NASTRAN input file, and run NASTRAN automatically could be written for iterations. In this way, different inputs could be entered and compared for the composite optimization.

Furthermore, the local buckling constraint method used in composite optimization is not proper for combined local buckling. This method is used only for local compression and in-plane bending buckling as local buckling constraints. For combined local buckling constraint, a different method needs to be developed. For the present study, unit load for compression is given and the critical compression

local buckling stress is calculated for every design region. For example, to combine shear loading with compression, percentages of unit shear and compression loads could be applied for a chosen design region. For various percentages of unit shear and compression loading, new critical buckling stresses could be calculated. When all critical buckling stress calculation is completed for various percentages of unit shear and compression loads, a 3D surface of critical combined buckling stresses with respect to various percentages of unit shear and compression loading could be plotted. Then according to the ratios of captured shear and compression stress, this 3D surface could be used as a constraint. As before, this method is needed to be done for every design region because every design region would have different critical buckling stresses. To this extent, writing a code for this method would be better as well.

For both optimizations, more design constraints could be added such as dynamic constraints like flutter or frequency. Besides, different materials could give lighter optimization results, hence different materials, different aluminum alloys and composite materials could be used to see their effect on the optimum HTP structure.

In this thesis, optimizations are performed only for one load case and it should be kept in mind that different load cases could have an effect of sizing different parts of the structure. Therefore, to obtain a preferably better optimization more load cases can be added to the study for the future work.

REFERENCES

- [1] Maxwell, C. (1869), Scientific Papers, Vol. 2, 175-177.
- [2] Barker, D., Johnson, E., Johnson, J., & Layfield, D. (2002), Design of Practical Composite Structure Using Enhancements to MSC.Nastran Structural Analysis and Optimization, 43rd AIAA/ASME/ASCE/AHS/ASC Structures, Structural Dynamics, and Materials Conference.
- [3] Vanderplaats, G.N. (1999), Numerical Optimization Techniques for Engineering Design, 3rd edition, McGraw-Hill Book Company.
- [4] MSC.NASTRAN® (2011), MSC.Nastran 2012 Design Sensitivity and Optimization User's Guide, MSC Software Corp.
- [5] Sevastyanov, V. (2010), Gradient-Based Multi-Objective Optimization Technology, 13th AIAA/ISSMO Multidisciplinary Analysis Optimization Conference, Multidisciplinary Analysis Optimization Conferences.
- [6] Kennedy, G., Martins, J. (2012), A Regularized Discrete Laminate Parametrization Technique with Applications to Wing-Box Design Optimization, 53rd AIAA/ASME/ASCE/AHS/ASC Structures, Structural Dynamics and Materials Conference, Structures, Structural Dynamics, and Materials and Co-located Conferences, Retrieved from <https://doi.org/10.2514/6.2012-1519>.
- [7] Butler, R. (1998), The optimisation of wing structures - theory or practice?, Aircraft Engineering and Aerospace Technology, Vol. 70, Iss. 1, 4-8.
- [8] Shabeer K.P., and Murtaza M. A. (2013), Optimization of Aircraft Wing with Composite Material, International Journal of Innovative Research in Science, Engineering and Technology, vol. 2, Iss. 6, 2471-2477.

- [9] Muralikrishna, P., Koteswara, U., and Vijayakumar, R. (2014), Design Optimization of Rotor Craft Horizontal Tail Plane using Fea, International Journal of Engineering Research and Technology (IJERT), vol. 3, Iss. 12, 165-172.
- [10] Liu, B. (2001), Two Level Optimization of Composite Wing Structures Based on the Panel Genetic Optimization (Doctoral dissertation), University of Florida, United States.
- [11] Engelstad, S., Barker, D., Ellsworth, C., and Proctor, L. (2003), Optimization Strategies for the F/A-22 Horizontal Stabilator, 44th AIAA/ASME/ASCE/AHS/ASC Structures, Structural Dynamics, and Materials Conference, Structures, Structural Dynamics, and Materials and Co-located Conferences, Retrieved from <https://doi.org/10.2514/6.2003-1456>.
- [12] Dababneh, O., Kipouros, T., and Whidborne. J. (2018), Application of an Efficient Gradient-Based Optimization Strategy for Aircraft Wing Structures. Aerospace 5:1, 3, Online publication date: 1-Mar-2018. Retrieved from <https://www.mdpi.com/2226-4310/5/1/3>.
- [13] Rongxin, X. (2012), Optimal Design of a Composite Wing Structure for a Flying-Wing Aircraft Subject to Multi-constraint. Unpublished master's thesis, Cranfield University, United Kingdom.
- [14] MSC.NASTRAN Version: 2012.2 (2012), MSC Software Corporation.
- [15] MSC.NASTRAN® (2011), MSC.Nastran 2012 Design Sensitivity and Optimization User's Guide, MSC Software Corp., 118.
- [16] MSC.NASTRAN® (2011), MSC.Nastran 2012 Design Sensitivity and Optimization User's Guide, MSC Software Corp., 442.
- [17] Leishman, G. J. (2006), Principles of Helicopter Aerodynamics with CD Extra, Cambridge University Press.
- [18] CATIA Version: V5 R21_X64 (2011), Dassault Systems.

- [19] MSC.Patran Version: x64 2012.2 (2012), MSC Software Corporation.
- [20] Chick, J. B. (2002), "Structural Optimization of Helicopter Empennage Using MSC.Nastran", In MSC.Software Corporation's Worldwide Aerospace Conference and Technology Showcase.
- [21] Hoffmann, M.J., Reuss Ramsay, R., and Gregorek, G.M. (1996), Effects of grit roughness and pitch oscillations on the NACA 4415 airfoil. NREL/TP-442-7815. National Renewable Energy Lab.
- [22] (2013), Metallic materials properties development and standardization (MMPDS): MMPDS-08, April 2013. Washington, D.C.: Federal Aviation Administration; Battelle Memorial Institute.
- [23] Yu, X., Johnson, E.H., Zhang, S. (2001), Discrete Optimization in MSC.Nastran, MSC Software Corporation.
- [24] MSC.NASTRAN® (2011), MSC.Nastran 2012 Design Sensitivity and Optimization User's Guide, MSC Software Corp., 105.
- [25] MSC.NASTRAN® (2004), MSC.Nastran 2004 Reference Manuel, MSC Software Corp., 548.
- [26] Narayanaswami, R., and Adelman, H. M. (1977), Evaluation of the Tensor Polynomial and Hoffman Strength Theories for Composite Materials, Journal of Composite Materials, Vol. II, 366.
- [27] Lee, D. G., Suh, N. P. (2005), Axiomatic Design and Fabrication of Composite Structures: Applications in Robots, Machine Tools, and Automobiles, Oxford University Press.
- [28] Yang, Q. J. (2009), Simplified Approaches to Buckling of Composite Plate. Master's thesis, University of Oslo, Norway.
- [29] Abbott, I.H., von Doenhoff, A.I. (1959), Theory of Wing Sections: Including a Summary of Airfoil Data, Dover Publications, Mineola.

[30] MSC.NASTRAN® (2011), MSC.NASTRAN 2012.2 Quick Reference Guide,
MSC Software Corporation.

APPENDICES

APPENDIX A

NACA 4415 C_L vs. ALPHA, AND C_D vs. C_L GRAPHS

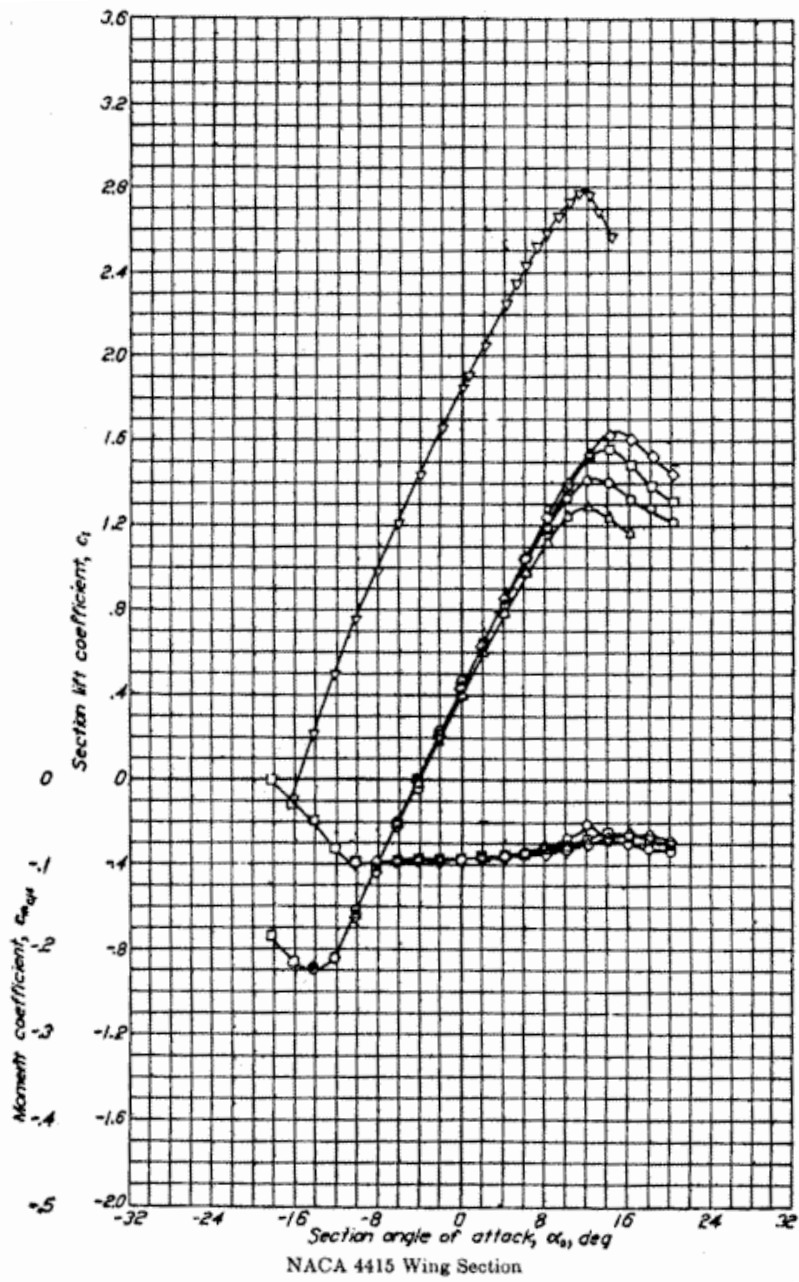


Figure A.1: NACA 4415 C_L vs alpha graph [29]

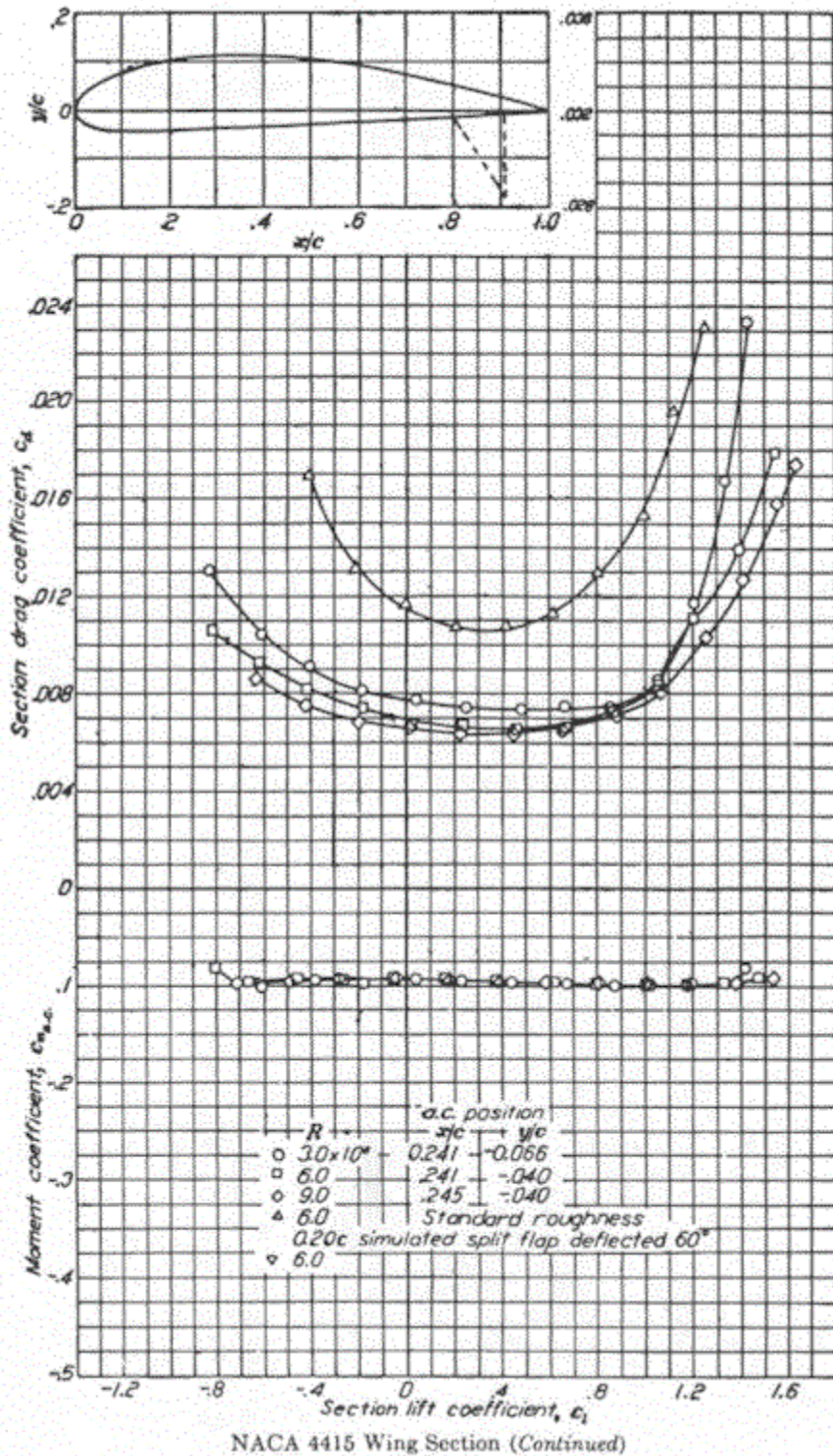


Figure A.2: NACA 4415 C_d vs. C_l graph [29]

APPENDIX B

DESCRIPTION OF NASTRAN INPUT FILES USED FOR OPTIMIZATION PROBLEMS

In this section, descriptions are taken from “MSC.NASTRAN 2012.2 Quick Reference Guide” [30]. Additional BDF codes (that could not be written using MSC.PATRAN) are written and explained. Descriptions are written in *italic* and explanations are written in **bold and italic**. Repetitive lines are removed.

For the aluminum optimization problem, every card and additional BDF codes are explained. For the composite optimization problem, only new cards and additional BDF codes are explained to avoid repetition.

ALUMINIUM OPTIMIZATION PROBLEM NASTRAN INPUT FILE

\$ Direct Text Input for Executive Control

\$ Design Sensitivity and Optimization Analysis

-SOL specifies solution sequence to be executed. In this case SOL 200 executes “Design Optimization” solution sequence.

SOL 200

-TIME sets the maximum CPU and I/O time. TIME 600 designates a runtime of 10 hours.

TIME 600

-CEND designates the end of the Executive Control Selection, it is an optional statement.

CEND

\$ Direct Text Input for Global Case Control Data

-TITLE defines a character string to appear on the first heading line of each page of MSC Nastran output.

TITLE = MSC.Nastran job created on 09-Apr-16 at 18:22:41

-ECHO controls echo (i.e., printout) of the Bulk Data.

ECHO = NONE

-MAXLINES sets the maximum number of output lines.

MAXLINES = 999999999

-DESOBJ selects the DRESP1 or DRESP2 entry to be used as the design objective. MIN specifies that the objective is to be minimized.

DESOBJ(MIN) = 1

-ANALYSIS specifies the type of analysis being performed for the current subcase. STATICS is used for Linear Static Analysis.

ANALYSIS = STATICS

-SUBCASE delimits and identifies a subcase.

SUBCASE 1

\$ Subcase name : Default

-SUBTITLE defines a subtitle that will appear on the second heading line of each page of printer output.

SUBTITLE=Default

-SPC selects a single point constraint set to be applied.

SPC = 2

**LOAD selects an external static load set.*

LOAD = 2

-DISPLACEMENT requests the form and type of displacement or pressure vector output. SORT1 means that output will be presented as a tabular listing of grid points for each load, frequency, eigenvalue, or time, depending on the solution sequence. REAL, requests real rectangular format of complex output.

DISPLACEMENT(SORT1,REAL)=ALL

-GPFORCE requests grid point force balance at selected grid points. ALL means that grid point force balance for all grid points will be output.

GPFORCE=ALL

-SPCFORCES requests the form and type of single point force of constraint vector output. SORT1, REAL and ALL are explained above.

SPCFORCES(SORT1,REAL)=ALL

-STRESS requests the form and type of element stress output. VONMISES requests von Mises stresses. BILIN Requests CQUAD4, CQUADR, and CTRIAR element stresses at center and grid points using bilinear extrapolation. SORT1, REAL and ALL are explained above.

STRESS(SORT1,REAL,VONMISES,BILIN)=ALL

-DESSUB selects the design constraints to be used in a design optimization task for the current subcase.

DESSUB = 22

\$ Direct Text Input for this Subcase

-Designates the beginning of a Bulk Data Section.

BEGIN BULK

\$ Direct Text Input for Bulk Data

-PARAM specifies values for parameters. POST -1 outputs the appropriate files for the MSC.PATRAN program. PRTMAXIM controls the printout of the maximums of applied loads, single-point forces of constraint, multipoint forces of constraint, and displacements. NASPRT specifies how often data recovery is performed and printed in SOL 200. Data recovery operations are performed at the first design cycle; at every design cycle that is a multiple of NASPRT; and the last design cycle.

PARAM POST -1

PARAM PRTMAXIM YES

PARAM NASPRT 1

\$ Elements and Element Properties for region : us11

-For every 2D design region a PSHELL is created, us11 means that first bay of upper skin leading edge.us11 is a user defined label for PSHELL 1.

-Defines the membrane, bending, transverse shear, and coupling properties of thin shell elements.0.41mm is initial thickness for this PSHELL.

PSHELL 1 1 0.41 1 1

\$ Pset: "us11" will be imported as: "pshell.1"

-CQUAD4 card defines an isoparametric membrane-bending or plane strain quadrilateral plate element. These CQUAD4 elements use PSHELL 1 as the element property and also include the connectivity information.

CQUAD4 486 1 706 750 756 712 90.

CQUAD4 487 1 750 751 757 756 90.

:

\$ Elements and Element Properties for region : fs1f

-For every 1D design region a PROD is created, fs1f means that first bay of front spar flanges. fs1f is a user defined label for PROD 64.

-PROD defines the properties of a rod element (CROD entry). 5 mm² is the initial area for this PROD.

PROD 64 3 5.

\$ Pset: "fs1f" will be imported as: "prod.64"

-CROD defines a tension-compression-torsion element. CROD cards reference the property identification cards (PROD) and also include the connectivity information.

CROD 877 64 85 84

CROD 878 64 84 83

:

\$ Referenced Material Records

\$ Material Record : Al_2024_T3_Clad_Sheet

\$ Description of Material : Date: 23-Jan-16 Time: 14:10:04

-MAT1 card defines the material properties for linear isotropic materials.

MAT1* 1 73773.9 .33

* 2.76799-6

\$ Material Record : Al_2024_T42_Clad_Sheet

\$ Description of Material : Date: 23-Jan-16 Time: 14:10:04

MAT1* 2 73773.9 .33

* 2.76799-6

\$ Material Record : Al_7050_T7451_Plate

\$ Description of Material : Date: 23-Jan-16 Time: 14:10:04

MAT1* 3 73084.4 .33

* 2.82335-6

\$ Nodes of the Entire Model

-GRID defines the location of a geometric grid point.

GRID 1 12691.5 -85. 2464.54

GRID 2 12743.6 -85. 2462.06

⋮

\$ Loads for Load Case : Default

-Defines a single-point constraint set as a union of single-point constraint sets defined on SPC or SPC1 entries.

SPCADD 2 1

-LOAD selects an external static load set.

LOAD 2 1. 1. 1 1.5 3

\$ Displacement Constraints of the Load Set : Fix_nodes

-SPC1 defines a set of single-point constraints.

SPC1 1 123456 1 5 32 44

\$ Pressure Loads of the Load Set : pressureonstructure

-PLOAD4 defines a pressure load on a face of a CTRIA3, CQUAD4 elements.

PLOAD4 3 45 -.00147

PLOAD4 3 46 -.0013313

:

\$...DESIGN VARIABLE DEFINITION

-DESVAR defines a design variable for design optimization. It gives their id, label, initial value, lower bound, upper bound, etc. and ddval card id which provides a set of allowable discrete values.

\$ fs1f_Area

DESVAR 1 fs1f_Are5. 5. 80. .5

\$ fs2f_Area

DESVAR 2 fs2f_Are5. 5. 80. .5

:

\$ r1lf_Area

DESVAR 7 r1lf_Are5. 5. 40. .5 7

\$ r1mf_Area

DESVAR 8 r1mf_Are5. 5. 40. .5 8

:

\$ ls1l_Thickness

DESVAR 38 ls1l_Thi0.41 .41 4.83 .5 38

\$ ls1m_Thickness

DESVAR 39 ls1m_Thi0.41 .41 4.83 .5 39

⋮

-As an example, DESVAR 39 has a used defined label “ls1m_Thi”, right next to it 0.41 implies its initial value as 0.41 mm. Then, it has a lower bound such as 0.41 mm and has an upper bound such as 4.83 mm. 0.5 is its fractional change allowed and 39 is its ddval card id. For every variable that needs ddval card, their ids are added by hand.

\$STANDARD AREAS

-DDVAL card defines real, discrete design variable values for discrete variable optimization. These ddval cards are added by hand.

```
ddval 7 4.88 8.2 12.8 16.2 18.2 20.4 25.4
      28.4 32 40.6
```

```
ddval 8 4.88 8.2 12.8 16.2 18.2 20.4 25.4
      28.4 32 40.6
```

⋮

\$STANDARD THICKNESSES

```
ddval 38 .41 .51 .64 .81 .91 1.02 1.27
      1.42 1.6 2.03 2.54 3.56 4.06 4.57 4.826
```

```
ddval 39 .41 .51 .64 .81 .91 1.02 1.27
      1.42 1.6 2.03 2.54 3.56 4.06 4.57 4.826
```

⋮

\$...DEFINITION OF THE RELATION BETWEEN THE DESIGN VARIABLES AND ANALYSIS MODEL PARAMETERS

-DVPREL1 defines the relation between an analysis model property and design variables.

DVPREL1 64 PROD 64 A

1 1.

DVPREL1 65 PROD 65 A

2 1.

⋮

-For example, DVPREL1 64 relates PROD 64 with DESVAR 1 with coefficient of 1. This coefficient defines the relation between a connectivity property and design variables. "A" is property name of the property entry.

DVPREL1 1 PSHELL 1 T

79 1.

DVPREL1 2 PSHELL 2 T

80 1.

⋮

- DVPREL1 with an id number 1 relates PSHELL 1 with DESVAR 79 with coefficient of 1. "T" is property name of the property entry.

\$...STRUCTURAL RESPONSE IDENTIFICATION

-DRESP1 defines a set of structural responses that is used in the design either as constraints or as an objective. Structural responses such as weight, displacements at grid points, element stresses etc. are available from directly MSC NASTRAN analysis.

DRESP1 1 min_w WEIGHT

-For example, DRESP1 1 has user defined label “min_w” and WEIGHT defines response available directly from MSC NASTRAN.

\$ DCONADD22

-DCONADD defines the design constraints for a subcase as a union of DCONSTR entries. Here, these set of constraints are associated with the objective, and constraints need equations. Equations are explained below. An important reminder: additional constraints that are written by hand should be added to DCONADD card to be associated with the objective function.

```
DCONADD  22   1   2   3   4   5   6   7
          8   9  10  11  12  13  14  15
          16  17  18  19  20  21  22  23
          24  25  26  27  28  29  30  31
:
:
```

\$ fs1f_axial

```
DRESP1  2   STR2  STRESS PROD      2      64
```

\$ fs2f_axial

```
DRESP1  3   STR3  STRESS PROD      2      65
```

:

-Above, DRESP1 with an id number 3 has a label STR3. Its structural response is STRESS and PROD is element property name. 2 is region identifier for constraint screening and 65 is response attributes. So, DRESP1 card (ID=2) takes axial stresses of PROD 64.

\$ fs1w_shear

```
DRESP1  28  STR28  STRESS PSHELL    24      37
```

DRESP1	29	STR29	STRESS	PSHELL	41	37
DRESP1	30	STR30	STRESS	PSHELL	58	37
DRESP1	31	STR31	STRESS	PSHELL	75	37
DRESP1	32	STR32	STRESS	PSHELL	32	37
DRESP1	33	STR33	STRESS	PSHELL	49	37
DRESP1	34	STR34	STRESS	PSHELL	66	37
DRESP1	35	STR35	STRESS	PSHELL	83	37

-Above, DRESP1 with id numbers 28 to 35 has labels STR28 to STR35, respectively. Their structural response is STRESS and PSHELL is their element property name. 37 is their response attributes. Therefore, DRESP1 cards with ID numbers 28 to 35 take shear stresses of each CQUAD4 elements of PSHELL 37.

-DRESP2 defines equation responses that are used in the design, either as constraints, as design variable or as an objective.

DRESP2 36 AVG36 1

DRESP1 28 29 30 31 32 33 34

35

-Here DRESP2 defines equation responses that are used as stress constraints as explained in Chapter 4.4.2.1. In this example DRESP2 card (ID=36) relates DRESP1 cards from 28 - 35 to the DEQATN card (ID=1).

-DEQATN defines one or more equations to use in the analysis.

DEQATN 1 AVGSTR (STR28 , STR29 , STR30 , STR31 , STR32 , STR33
, STR34 , STR35) = AVG (STR28 , STR29 , STR30 , STR31 , STR32
, STR33 , STR34 , STR35)

⋮

-In the above example, DEQATN 1 card takes the average stress defined by DRSEP1 cards for the front spar web 1. DRESP2 36 card is related to the proper constraint definition in constraints part.

-Until here, BDF file is written through the Patran GUI. Some relations cannot be defined in MSC.PATRAN GUI such as thickness or area reduction from root to tip and local buckling equations. It is mentioned in Chapter 4.4.2.3 that design variable relations should be controlled to reach the global optimum.

\$...Order of Front Spar Flange Areas (defined by the user)

\$ ac defines the area control (defined by the user)

\$ bf:bigger flange area, sf:smaller flange area (defined by the user)

\$ fs6f > fs5f

-All flange area relations are written by hand; in here, front spar flange area in region 6 should be bigger than front spar flange area in region 5.

-In this example, DRESP2 card defines equation responses that are used as design variables. It is seen that DRESP2 card (ID=2000) relates DESVAR 95 and 5 with DEQATN card (ID=500). Here, 95 and 5 are ID numbers of design variables.

```
DRESP2 2000 ac 500
```

```
DESVAR 95 5
```

```
DEQATN 500 ac(bf,sf)=bf-sf
```

-DEQATN 500 card is an equation which defines the relation between DESVAR 95 which is bf and DESVAR 5 which is sf. They are written as bf (bigger flange area) and sf (smaller flange area) by user, but that would be accurate when constraint definitions are given. DRESP2 2000 card is related to the proper constraint definition and explained in constraints part later.

\$...front spar webs order (defined by the user)

\$ tc defines the thickness control (defined by the user)

\$ bw:bigger web thickness, sw:smaller web thickness (defined by the user)

\$ fs6w > fs5w

-All web thickness relations are written by hand; here, front spar web thickness in region 6 should be bigger than the front spar web thickness in region 5.

DRESP2 2026 tc 526

DESVAR 37 36

DEQATN 526 tc(bw,sw)=bw-sw

-In this example DRESP2 card (ID=2026) relates design variables DESVAR 37 and 36 in a design equation card DEQATN (ID=526). In this example DESVAR 37 is the design variable of the front spar web thickness in region 6 and DESVAR 36 is the design variable of the front spar web thickness in region 5. DEQATN 526 card is a design equation which defines the relation between the DESVAR 37 which refers to bw and DESVAR 36 which refers to sw. They are written as bw (bigger web thickness) and sw (smaller web thickness) by user, but that would be accurate when constraint definitions are given. DRESP2 2026 card is related to the proper constraint definition in constraints part.

\$...LOCAL BUCKLING EQUATIONS

\$FS1W

-All local buckling equations are written by hand. In this example front spar web region 1 is examined. As explained in Chapter 4.4.2.2 combined local buckling equations are used. According to loading of webs; firstly, their shear, bending and compression buckling equations are written and then they are related with interaction equations. As a reminder the combined buckling equation under compression and shear stress for spar webs is defined as:

$$R_s^2 + R_b^2 \leq 1 \quad \Rightarrow \quad \left(\frac{\tau}{K_s E \left(\frac{t}{b}\right)^2} \right)^2 + \left(\frac{\sigma_{\text{comp}}}{K_b E \left(\frac{t}{b}\right)^2} \right)^2 \leq 1 \quad \text{B.1}$$

\$shear loading

DRESP2 3000 BS 1000

 DESVAR 32

 DRESP2 36

DEQATN 1000 BS(vrb,str)=str/(5.232*73084.43*(vrb/87.233)**2)

-In this example, DRESP2 card (ID=3000) relates DESVAR 32 and DRESP2 36 in design equation card DEQATN (ID=1000). DESVAR 32 is the design variable which refers to the front spar web thickness in region 1 and DRESP2 36 is the average shear stress of the front spar web in region 1. DEQATN 1000 card is an equation which defines the local shear buckling relation. It takes DESVAR 32 and DRESP2 36 as inputs. 'vrb' stands for the variable (DESVAR 32), and 'str' stands for the average stress (DRESP2 36). BS(vrb,str) equation is the first part of the Equation B.1, and K_s is the shear buckling coefficient with a value of 5.232, the modulus of elasticity E value is 73084.43 and 87.233 is the b dimension of front spar web plate in region 1 for shear buckling equation.

\$bending loading

DRESP2 5000 BB 1800

 DESVAR 32

 DRESP2 594

DEQATN 1800 BB(vrb,str)=str/(21.8*73084.43*(vrb/250.00)**2)

-In this example, DRESP2 card (ID= 5000) relates DESVAR 32 and DRESP2 594 in design equation card DEQATN (ID= 1800). DESVAR 32 is the design variable

which refers to the front spar web thickness in region 1 and DRESP2 594 is the average bending stress of the front spar web in region 1. DEQATN 1800 card is an equation which defines the local bending buckling relation. It takes DESVAR 32 and DRESP2 594 as inputs. 'vrb' stands for the variable (DESVAR 32), and 'str' stands for the average stress (DRESP2 594). BB(vrb,str) equation is the second part of the Equation B.1, and K_b is the bending buckling coefficient with a value of 21.8, the modulus of elasticity E value is 73084.43 and 250.00 is the b dimension of front spar web plate in region 1 for bending buckling equation.

\$combined local buckling equation

DRESP2 6000 CB 7000

 DRESP2 3000 5000

DEQATN 7000 CB(BS,BB)=BS*BS+BB*BB

-Above, DRESP2 card whose id is 6000 relates DRESP2 3000 and 5000 (just described) with DEQATN card whose id is 7000. DEQATN 7000 card is an equation which defines the combined local buckling relation. It takes DRESP2 3000 and 5000 as inputs. 'BS' stands for buckling shear (DRESP2 3000), and 'BB' stands for buckling bending (DRESP2 5000).

⋮

\$...CONSTRAINTS

-DCONSTR defines design constraints.

DCONSTR 1 2 -441. 455.

DCONSTR 2 3 -441. 455.

-Here, these constraints are strength constraints. They are defined in the MSC.PATRAN GUI and written to the BDF file by MSC.PATRAN. The first DCONSTR 1 card relates the DRESP1 with an id 2 and the constraint equation has a lower limit of -441 and an upper limit of 455.

⋮

DCONSTR 139 2000 .1e-10

DCONSTR 140 2001 .1e-10

-These constraints are the flange area and thickness order constraints. They are included in the Nastran input file by the user and these relate written equations with the design objective via the DCONADD card. These constraints have a lower limit of .1e-10 and no upper limit which guarantees that design equation 500 is always positive. 2000 stands for the DRESP2 2000 card explained before.

⋮

DCONSTR 217 6000 1.01

DCONSTR 218 6001 1.01

- Constraints 217 and 218 are local buckling constraints. They are included in the Nastran input file by the user and these relate written equations with the design objective via the DCONADD card. These constraints have an upper limit of 1.01 which is upper limit of the local buckling equations. 6000 stands for the DRESP2 6000 card explained before.

⋮

\$...OPTIMIZATION CONTROL

-DOPTPRM overrides default values of parameters used in design optimization.

-DESMAX is maximum number of design cycles to be performed.

-FSDMAX specifies the number of Fully Stressed Design Cycles that are to be performed. (Default = 0)

- P1 and P2 are some of the design cycle print controls, P1 controls the frequency of the output and P2 provides a first level control of which design quantities are printed. P1 = 0 is the default value and it gives the output for initial and optimal

designs and $P1 = n$ gives the output for every n -th design cycle. $P2$ can take different values depending on which output is needed, $P2 = 0$ gives no output, $P2 = 1$ gives the output of the objective function and design variables and $P2 = 2$ outputs the designed properties. $P2 = 15$ prints out all available design data, this value gives also violated constraints if there are any.

-*METHOD* is optimization method; 0 is automatic selection for a better performance based on number of design variables, number of constraints, number of active/violated constraints and computer memory. If it is 1, it is for Modified Method of Feasible Directions for MSCADS. **The Modified Method of Feasible Directions (MMFD) is a direct numeric optimization technique used to solve constrained optimization problems. In this work, 1 is selected.** If it is 2, it is for Sequential Linear Programming for MSCADS. If it is 3, it is for Sequential Quadratic Programming for MSCADS. If it is 4, it is for SUMT method for MSCADS.

- *OPTCOD* specifies which optimization code to be used in SOL 200. If “MSCADS” is written, MSCADS is used. If “IPOPT” is written, IPOPT is used.

-*CONV1* is relative criterion to detect convergence. If the relative change in objective between two optimization cycles is less than *CONV1*, then optimization is terminated.

-*CONV2* is absolute criterion to detect convergence. If the absolute change in objective between two optimization cycles is less than *CONV2*, then optimization is terminated.

-*CONVDV* is relative convergence criterion on design variables. (Real > 0.0; Default = 0.001 for non-topology; Default = 0.0001 for topology optimization)

-*CONVPR* is relative convergence criterion on properties.

-*DELP* is fractional change allowed in each property during any optimization design cycle. This provides constraints on property moves.

-DELX is fractional change allowed in each design variable during any optimization cycle. (Real > 0.0; Default = .5 for sizing/shape/topometry optimization; Default = 0.2 for topology and topography optimization)

-DPMIN is minimum move limit imposed.

-DXMIN is minimum design variable move limit. (Real > 0.0; Default = 0.05 for sizing/shape/topometry optimization; Default = 1.0E-5 for topology and topography optimization)

-CT is constraint tolerance.

-GMAX is maximum constraint violation allowed at the converged optimum.

-CTMIN: Constraint is considered violated if current value is greater than CTMIN.

-DISCOD is Discrete Processing Method. If it is 0, then No Discrete Optimization method is used. If it is 1, then Design of Experiments method is used. If it is 2, then Conservative Discrete Design method is used. If it is 3, then Round up to the nearest design variable method is used. If it is 4, then Round off to the nearest design variable method is used.

-DISBEG Design cycle ID for discrete variable processing initiation. Discrete variable processing analysis is carried out for every design cycle after DISBEG.

```
DOPTPRM DESMAX 5000 FSDMAX 0 P1 1 P2 15
METHOD 1 OPTCOD MSCADS CONV1 .001 CONV2 1.-20
CONVDV .001 CONVPR .01 DELP .2 DELX .5
DPMIN .01 DXMIN .05 CT -.03 GMAX .005
CTMIN .003 DISCOD 1 DISBEG 1
```

\$ Referenced Coordinate Frames

-ENDDATA designates the end of the Bulk Data Section.

```
ENDDATA 4bdb540c
```

COMPOSITE OPTIMIZATION SAMPLE NASTRAN INPUT FILE

SOL 200

TIME 600

CEND

\$ Direct Text Input for Global Case Control Data

TITLE = MSC.Nastran job created on 01-Apr-17 at 15:32:39

ECHO = SORT,PUNCH (NEWBULK)

MAXLINES = 999999999

DESOBJ(MIN) = 1

ANALYSIS = STATICS

SUBCASE 1

\$ Subcase name : Default

SUBTITLE=Default

SPC = 2

LOAD = 2

DISPLACEMENT(SORT1,REAL)=ALL

SPCFORCES(SORT1,REAL)=ALL

STRESS(SORT1,REAL,VONMISES,BILIN)=ALL

DESSUB = 22

BEGIN BULK

\$ Direct Text Input for Bulk Data

PARAM POST -1

PARAM PRTMAXIM YES

\$ Elements and Element Properties for region : fs1_shell

\$ Composite Property Record created from material record : fs1

\$ Composite Material Description :

-PCOMP defines the properties of an n-ply composite material laminate. "TSAI" is for the Tsai-Wu failure theory. "SYM": Only plies on one side of the element centerline are specified. The plies are numbered starting with 1 for the bottom layer. If an odd number of plies are desired, the center ply thickness (T1) should be half the actual thickness.

PCOMP	1		79.	TSAI			SYM	
	1	.26	-45.	YES	1	.26	90.	YES
	1	.26	45.	YES	1	.26	0.	YES

\$ Pset: "fs1_shell" will be imported as: "pcomp.1"

CQUAD4 721 1 85 111 1123 84 1

CQUAD4 722 1 111 112 153 1123 1

:

\$ Referenced Material Records

\$ Material Record : HexPlyAS4_8552_RC34_AW134

\$ Description of Material : Date: 11-Mar-17 Time: 13:36:05

-MAT8 defines the material property for an orthotropic material for isoparametric shell elements.

MAT8 1 130000. 8700. .36 2900. 2900. 2900. 1.58-6
2280. 1360. 35. 223. 107.

\$ Nodes of Group : ALL_FEM

GRID 1 12691.5 -85. 2464.54

GRID 2 12743.6 -85. 2462.06

:

\$ Loads for Load Case : Default

SPCADD 2 1

LOAD 2 1. 1.5 1

\$ Displacement Constraints of Load Set : Fix_nodes

SPC1 1 123456 1 5 32 44

\$ Pressure Loads of Load Set : pressureonstructure

PLOAD4 1 45 -.00147

PLOAD4 1 46 -.0013313

PLOAD4 1 47 -.0011

:

\$...DESIGN VARIABLE DEFINITION

\$ fs1_T1

DESVAR 1FS1_T1:1 .13 .13 .52 1

\$ fs1_T2

DESVAR 2FS1_T2:2 .13 .13 .52 2

\$ fs1_T3

DESVAR 3FS1_T3:3 .13 .13 .52 3

\$ fs1_T4

DESVAR 4FS1_T4:4 .13 .13 .52 4

⋮

\$ fs1_O1

DESVAR 253FS1_O1:2 0.0 -45. 90. 1.863-9 253

\$ fs1_O2

DESVAR 254FS1_O2:2 90. -45. 90. 1.863-9 254

\$ fs1_O3

DESVAR 255FS1_O3:2 90. -45. 90. 1.863-9 255

\$ fs1_O4

DESVAR 256FS1_O4:2 0.0 -45. 90. 1.863-9 256

⋮

-As seen above, for front spar web region 1 there are 8 design variables. (In every web region there are 8 plies and 8 design variables because of the symmetry.) Four of them are discrete ply thicknesses, and four of them are discrete orientations.

-As an example, DESVAR 256 has a user defined label “FS1_O4:2”, right next to it 0.00 implies its initial value as 0 degree orientation. Then, it has a lower limit such as -45 degree and has an upper limit such as 90 degree. 1.863-9 comes

automatically from PATRAN and it is its fractional change allowed. Finally, 256 is its dval card id. For every variable that needs dval card, their ids are added by hand.

\$...STANDART PLY THICKNESSES

DDVAL 1 0.13 0.26 0.39 0.52

DDVAL 2 0.13 0.26 0.39 0.52

DDVAL 3 0.13 0.26 0.39 0.52

DDVAL 4 0.13 0.26 0.39 0.52

⋮

\$...STANDART AREAS

DDVAL 253 -45 0 45 90

DDVAL 254 -45 0 45 90

DDVAL 255 -45 0 45 90

DDVAL 256 -45 0 45 90

⋮

-DDVAL cards are added by hand, these cards define discrete values for DESVAR cards. For every region, they are written by hand. For example, DDVAL 256 has four discrete values such as -45, 0, 45 and 90 degrees.

**\$...DEFINITION OF DESIGN VARIABLE TO ANALYSIS MODEL
PARAMETER RELATIONS**

DVPREL1 2 PCOMP 1 THETA1

+ 253 1.

DVPREL1 1 PCOMP 1 T1

+ 1 1.

DVPREL1 4 PCOMP 1 THETA2

+ 254 1.

DVPREL1 3 PCOMP 1 T2

+ 2 1.

DVPREL1 6 PCOMP 1 THETA3

+ 255 1.

DVPREL1 5 PCOMP 1 T3

+ 3 1.

DVPREL1 8 PCOMP 1 THETA4

+ 256 1.

⋮

-For example, DVPREL1 8 relates PCOMP 1 with DESVAR 256 with coefficient of 1. This coefficient defines the relation between a connectivity property and design variables. "THETA4" is property name of the property entry.

\$...STRUCTURAL RESPONSE IDENTIFICATION

DRESP1 1 min_w WEIGHT

\$ DCONADD22

-DCONADD defines the design constraints for a subcase as a union of DCONSTR entries. Here, these set of constraints are associated with the objective, and constraints need equations. Equations are explained below. An important

reminder: additional constraints that are written by hand should be added to DCONADD card to be associated with the objective function.

```
DCONADD  22    1    2    3    4    5    6    7
          8    100  101  102  103  104  105  106
          107  108  109  110  111  112  113  114
          :
```

\$ FI_Ply1

```
DRESP1  2    CFI2  CFAILURE PCOMP    5    1    1
          2    3    4    5    6    7    8    9
          10   11   12   13   14   15   16   17
          :
```

-Above, DRESP1 card defines Tsai-Wu failures indices that are explained in Chapter 5.4.2.1 and these are generated in MSC.PATRAN interface.

-DRESP1 with an id number 2 has a label CFI2. Its structural response is CFAILURE and PCOMP is element property name. 5 is region identifier for constraint screening and 1 is Failure Criterion Item Code for CFAILURE. Next 1 is lamina number (Default=1). Next numbers are element id numbers.

\$...LOCAL AVERAGE STRESSES FOR BUCKLING

-Here, front spar web region 1 average laminate stress calculation is explained as an example. The average laminate stress is constrained with the calculated critical local buckling stress as explained in Chapter 5.4.2.2.

\$ fs1_1_str

```
DRESP1  10    CST10  CSTRESS PCOMP    3    1    1
```

\$ fs1_2_str

DRESP1 11 CST11 CSTRESS PCOMP 3 2 1

\$ fs1_3_str

DRESP1 12 CST12 CSTRESS PCOMP 3 3 1

\$ fs1_4_str

DRESP1 13 CST13 CSTRESS PCOMP 3 4 1

\$ fs1_5_str

DRESP1 14 CST14 CSTRESS PCOMP 3 5 1

\$ fs1_6_str

DRESP1 15 CST15 CSTRESS PCOMP 3 6 1

\$ fs1_7_str

DRESP1 16 CST16 CSTRESS PCOMP 3 7 1

\$ fs1_8_str

DRESP1 17 CST17 CSTRESS PCOMP 3 8 1

-For every ply of the front spar web region 1 (8 ply in total), composite laminate compressive stresses are taken with DRESP1 cards above.

-DRESP1 with an id number 17 has a label CST17. Its structural response is CSTRESS and PCOMP is element property name. 3 is region identifier for constraint screening and 8 is Stress Item Code for CSTRESS. Next 1 is lamina number (Default=1).

DRESP2 4000 AVG 2000

DRESP1 10 11 12 13 14 15 16

```

DEQATN 2000  AVGSTR ( CST10 , CST11 , CST12 , CST13 , CST14 , CST15
, CST16 , CST17 ) = AVG ( CST10 , CST11 , CST12 , CST13 , CST14
, CST15 , CST16 , CST17 )

```

-Above, DRESP2 defines equation responses that are used as stresses. It is seen that DRESP2 card whose id is 4000 relates DRESP1 cards from 10 to 17 with the DEQATN card whose id is 2000. DEQATN 2000 card takes average laminate stresses of DRSEPI cards for front spar web 1. Then DRESP2 card is related with constraints below.

⋮

\$...Front Spar Webs Order (defined by the user)

- It is mentioned in Chapter 5.4.2.3 that design variable relations with each other should be controlled to reach global optimum. Laminate thicknesses should be increased from tip to root of the horizontal tail plane.

\$ tc defines thickness control (defined by the user)

\$ e+f+g+h:bigger web, a+b+c+d:smaller web (defined by the user)

\$ fs2 > fs1 (defined by the user)

-All flange area relations are written by hand; in here, front spar laminate thickness region 2 should be bigger than front spar flange laminate thickness 1.

```

DRESP2      3000  tc      1000

```

```

      DESVAR      1      2      3      4

```

```

           5      6      7      8

```

```

DEQATN      1000  tc(a,b,c,d,e,f,g,h)=(e+f+g+h)-(a+b+c+d)

```

- Above, DRESP2 defines equation responses that are used as design variables. It is seen that DRESP2 card whose id is 3000 relates DESVAR cards from 1 to 8 with DEQATN card whose id is 1000. DESVAR cards from 1 to 4 are ply thicknesses of front spar web region 1 and DESVAR cards from 5 to 8 are ply thicknesses of front spar web region 2. DEQATN 1000 card is an equation which defines the relation between front spar laminate thickness region 1 and 2. Then DRESP2 card is related with constraints below.

⋮

\$...CONSTRAINTS

DCONSTR 1 2 1.

DCONSTR 2 3 1.

-These constraints are strength constraints. They are given in MSC.PATRAN GUI and written to the Nastran input (BDF) file by MSC.PATRAN. The first DCONSTR 1 card relates the DRESP1 which has an id 2 which has an upper limit 1 which is the limit of failure index.

⋮

DCONSTR 100 3000 .11

DCONSTR 101 3001 .11

-These constraints are laminate thickness order constraints. They are written by hand and these relate DRESP2 equations added by the user above with the design objective, by adding the DCONSTR id to DCONADD card. These constraints have a lower limit of 0.11 which guarantees that every laminated web at least one more ply from root to tip as ply thickness is equal to 0.13 mm. 100 is the id of DCONSTR card and 3000 is the id of DRESP2 card that is explained above.

⋮

DCONSTR 200 4000 4.939

```

DCONSTR  201  4001      4.939
DCONSTR  202  4002     11.1037

```

-And these constraints are critical local buckling stress constraints. They are written by hand these relate DRESP2 equations added by the user above with the design objective, by adding the DCONSTR id to DCONADD card. These constraints are calculated critical buckling stress limits and they are explained in Chapter 5.4.2.2. 200 is the id of DCONSTR card and 4000 is the id of DRESP2 card that is explained above.

⋮

\$...OPTIMIZATION CONTROL

```

DOPTPRM DESMAX 500  FSDMAX 0  P1  0  P2  15

METHOD 1  OPTCOD MSCADS CONV1 .001  CONV2 1.-20

CONVDV .001  CONVPR .01  DELP .2  DELX .5

DPMIN .01  DXMIN .05  CT  -.03  GMAX .005

CTMIN .003  DISCOD 1  DISBEG 0

```

\$ Referenced Coordinate Frames

-CORD2R defines a rectangular coordinate system using the coordinates of three points. These are used as material coordinate systems.

```

CORD2R  1      12691.5 -1500. 2464.54 25706.9 -1500. 2464.54
          12691.5 11515.3 2464.54

CORD2R  2      12542.9 -1500. 2441.24 12542.9 -14366. 2441.24
          25408.9 -1500. 2441.24

CORD2R  3      12691.5 -85. 2464.54 12691.5 -85. -10464.3

```

12691.5 12843.9 2464.54

CORD2R 4 12899.6 -85. 2386.53 12899.6 -85. 15505.3

12899.6 13033.8 2386.53

ENDDATA 8b074705

APPENDIX C

BUCKLING COEFFICIENT CALCULATION

Buckling coefficients depend on the plate aspect ratio and boundary conditions. For the in-plane bending loading Figure C.1 gives the in-plane buckling coefficients for different plate aspect ratios and for the simply supported edge conditions. For K_b , b is the loaded edge.

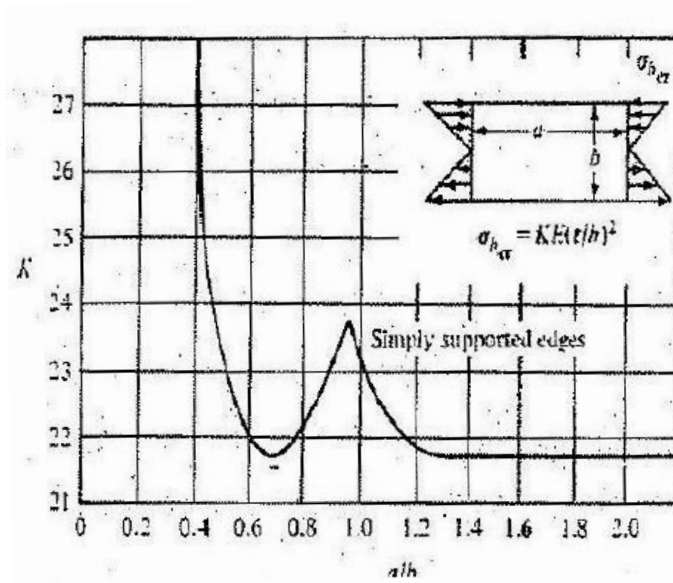


Figure C.1: In-plane bending buckling coefficient K_b versus plate aspect ratio

In-plane bending buckling coefficient curve is formularized by means of curve fitting using Microsoft Excel, and used in the buckling constraint equations. Equations C.1 and C.2 give the in-plane bending local buckling coefficients in two different regions.

For $\frac{a}{b} = x \leq 1.3$;

$$K_b = -231.72 x^6 + 1471.7 x^5 - 3586.3 x^4 + 4285.9 x^3 - 2623.1 x^2 + 762.95 x - 56.102 \quad \text{C.1}$$

For $\frac{a}{b} = x > 1.3$;

$$K_b = 21.8 \quad \text{C.2}$$

Figure C.2 gives the shear buckling coefficients for different plate aspect ratios and different edge conditions. For K_s , b is always the shorter dimension of the plate as all edges carry shear.

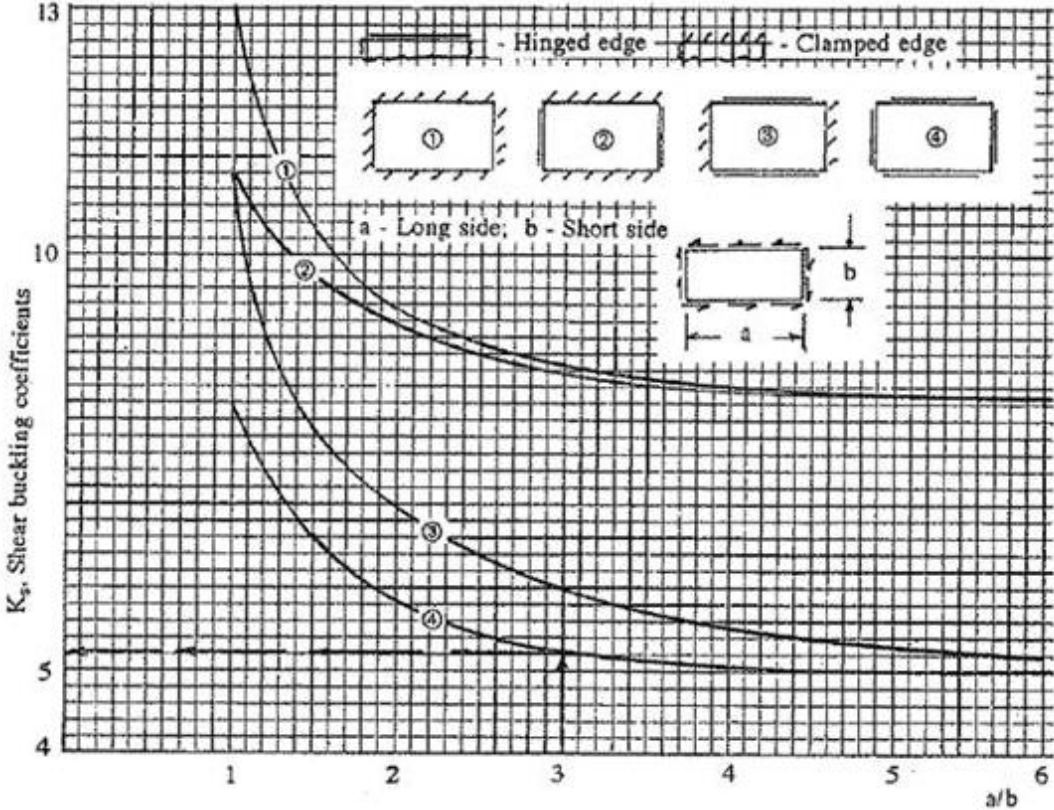


Figure C.2: Shear buckling coefficient K_s plate aspect ratio for different edge conditions

Shear buckling coefficient curve is formularized by means of curve fitting using Microsoft Excel, and used in the buckling constraint equations. Equations C.3 and C.4 give the shear local buckling coefficients in two different regions.

For $\frac{a}{b} = x \leq 4.4$; C.3

$$K_s = -0.0234 x^5 + 0.3669 x^4 - 2.3717 x^3 + 8.0599 x^2 - 14.757 x + 16.925$$

For $\frac{a}{b} = x > 4.4$; C.4

$$K_s = 6.0$$

Figure C.3 gives the compression buckling coefficients for different plate aspect ratios and different edge conditions. For K_c , b is the loaded edge of the plate.

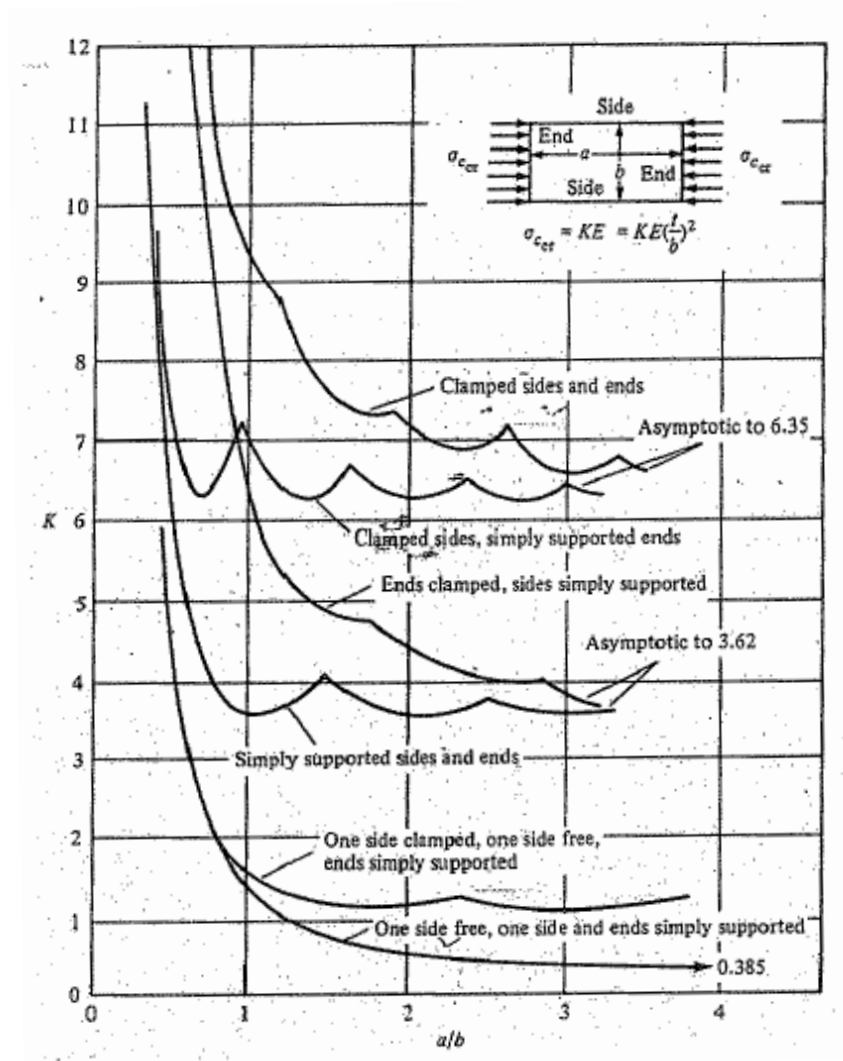


Figure C.3: Compression buckling coefficient K_c versus plate aspect ratio for different edge conditions

Compression buckling coefficient curve is formularized by means of curve fitting using Microsoft Excel, and used in the buckling constraint equations. Equations C.5 and C.6 give the compression buckling coefficients in two different regions.

For $\frac{a}{b} = x \leq 2.7$; C.5

$$K_c = -1.8939 x^6 + 16.69 x^5 - 55.609 x^4 + 84.987 x^3 - 54.093 x^2 + 3.4296 x + 10.144$$

For $\frac{a}{b} = x > 2.7$; C.6

$$K_c = 3.62$$

For the spar web regions, edge 1 and edge 2 dimensions are shown in Figure C.4. Then, the spar web regions' shear and in-plane bending buckling coefficients are given in Table C.1. For K_s , b is selected as shorter dimension and for K_b ; b is the loaded edge of the plates.

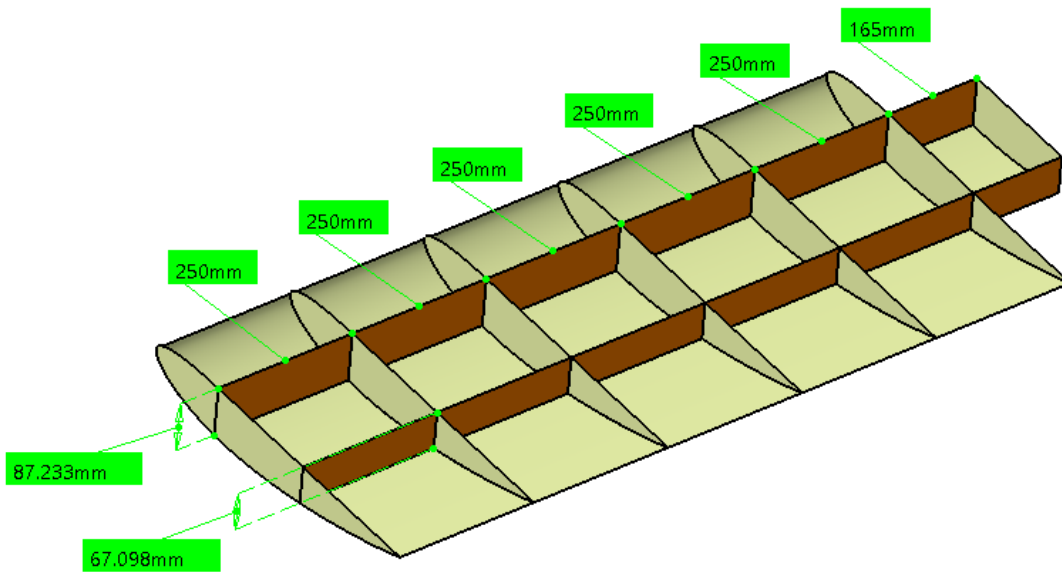


Figure C.4: Front and rear spar edge 1 and edge 2 dimensions

Table C.1: Shear and compression buckling coefficients for the spar web regions

Variable	edge 1	edge 2	a/b for K_s	K_s	a/b for K_b	K_b
fs1w	250.000	87.233	2.866	5.232	2.866	21.800
fs2w	250.000	87.233	2.866	5.232	2.866	21.800
fs3w	250.000	87.233	2.866	5.232	2.866	21.800
fs4w	250.000	87.233	2.866	5.232	2.866	21.800
fs5w	250.000	87.233	2.866	5.232	2.866	21.800
fs6w	165.000	87.233	1.891	5.928	1.891	21.800

rs1w	250.000	67.098	3.726	5.064	3.726	21.800
rs2w	250.000	67.098	3.726	5.064	3.726	21.800
rs3w	250.000	67.098	3.726	5.064	3.726	21.800
rs4w	250.000	67.098	3.726	5.064	3.726	21.800
rs5w	250.000	67.098	3.726	5.064	3.726	21.800
rs6w	165.000	67.098	2.459	5.420	2.459	21.800

For the lower and upper skin regions, edge 1 and edge 2 dimensions are shown in Figure C.5 and C.6. Then, the lower and upper skin regions' shear and in-plane bending buckling coefficients are given in Table C.2 and C.3. For K_s , b is selected as shorter dimension and for K_c ; b is the loaded edge of the plates.

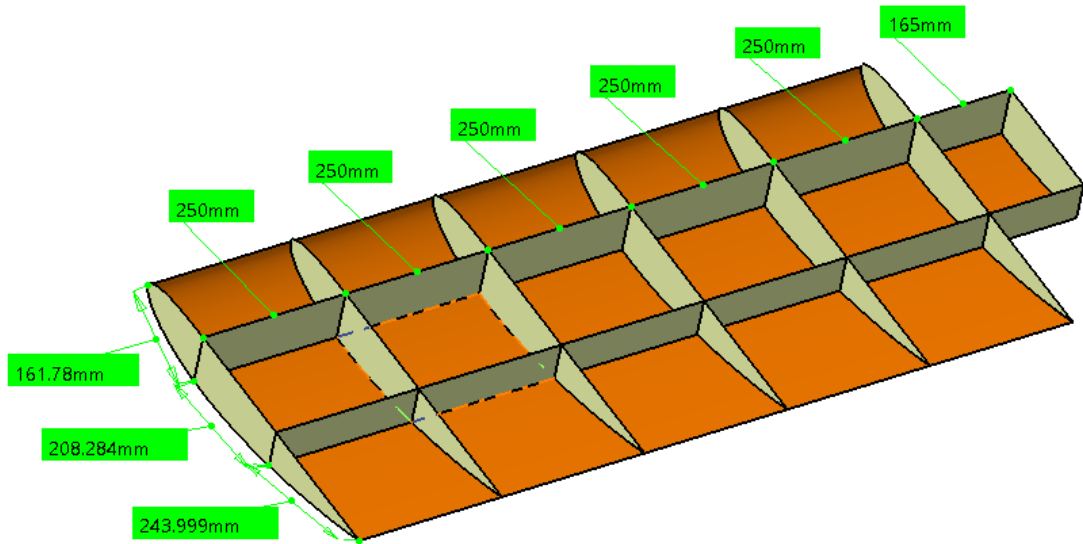


Figure C.5: Lower skin edge 1 and edge 2 dimensions

Table C.2: Shear and compression buckling coefficients for the lower skin regions

variable	edge 1	edge 2	a/b for K_s	K_s	a/b for K_c	K_c
ls1l	250.000	161.780	1.545	6.502	0.647	4.745
ls1m	250.000	208.284	1.200	7.426	0.833	3.876
ls1t	250.000	243.999	1.025	8.093	0.976	3.662
ls2l	250.000	161.780	1.545	6.502	0.647	4.745
ls2m	250.000	208.284	1.200	7.426	0.833	3.876
ls2t	250.000	243.999	1.025	8.093	0.976	3.662
ls3l	250.000	161.780	1.545	6.502	0.647	4.745
ls3m	250.000	208.284	1.200	7.426	0.833	3.876
ls3t	250.000	243.999	1.025	8.093	0.976	3.662

ls4l	250.000	161.780	1.545	6.502	0.647	4.745
ls4m	250.000	208.284	1.200	7.426	0.833	3.876
ls4t	250.000	243.999	1.025	8.093	0.976	3.662
ls5l	250.000	161.780	1.545	6.502	0.647	4.745
ls5m	250.000	208.284	1.200	7.426	0.833	3.876
ls5t	250.000	243.999	1.025	8.093	0.976	3.662
ls6m	165.000	208.284	1.262	7.226	1.262	3.861

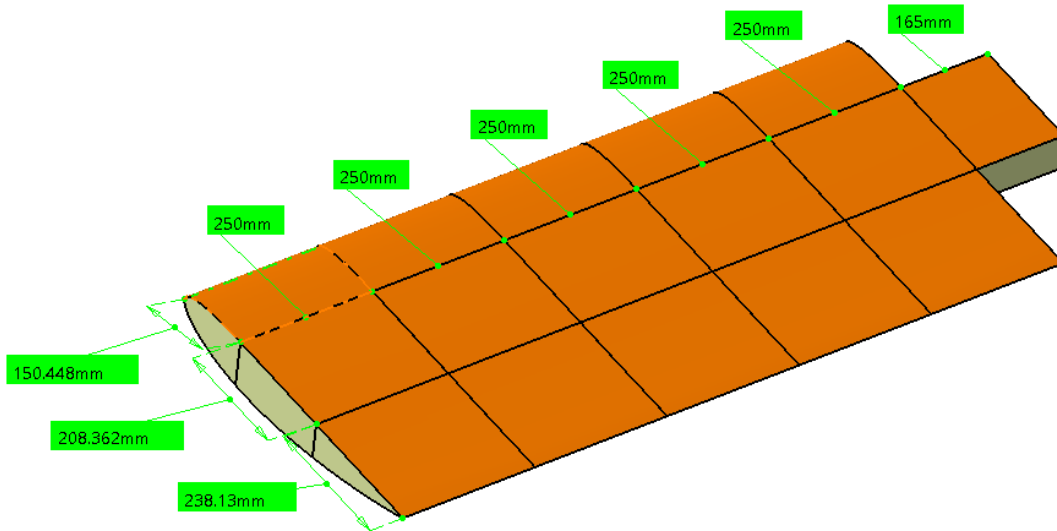


Figure C.6: Upper skin edge 1 and edge 2 dimensions

Table C.3: Shear and compression buckling coefficients for the upper skin regions

variable	edge 1	edge 2	a/b for K_s	K_s	a/b for K_c	K_c
us1l	250.000	150.448	1.662	6.277	0.602	5.074
us1m	250.000	208.362	1.200	7.428	0.833	3.875
us1t	250.000	238.130	1.050	7.987	0.953	3.675
us2l	250.000	150.448	1.662	6.277	0.602	5.074
us2m	250.000	208.362	1.200	7.428	0.833	3.875
us2t	250.000	238.130	1.050	7.987	0.953	3.675
us3l	250.000	150.448	1.662	6.277	0.602	5.074
us3m	250.000	208.362	1.200	7.428	0.833	3.875
us3t	250.000	238.130	1.050	7.987	0.953	3.675
us4l	250.000	150.448	1.662	6.277	0.602	5.074
us4m	250.000	208.362	1.200	7.428	0.833	3.875
us4t	250.000	238.130	1.050	7.987	0.953	3.675
us5l	250.000	150.448	1.662	6.277	0.602	5.074
us5m	250.000	208.362	1.200	7.428	0.833	3.875
us5t	250.000	238.130	1.050	7.987	0.953	3.675
us6m	165.000	208.362	1.263	7.225	1.263	3.861

For the rib regions, edge 1 and edge 2 dimensions are shown in Figure C.7. Then, the rib regions' shear coefficients are given in Table C.4. For K_s , b is selected as shorter dimension.

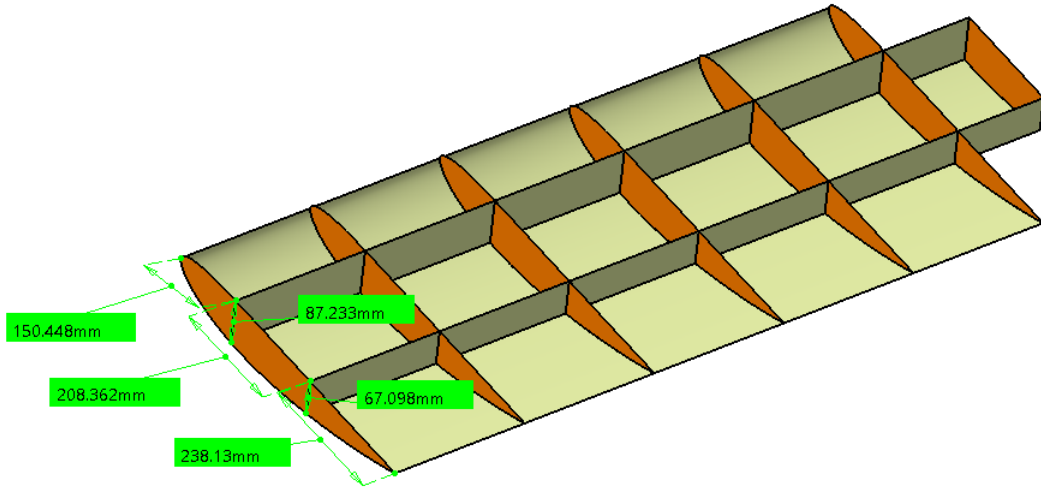


Figure C.7: Ribs edge 1 and edge 2 dimensions

Table C.4: Shear buckling coefficients for the rib regions

variable	edge 1	edge 2	a/b for K_s	K_s
r1lw	150.448	87.233	1.725	6.170
r1mw	208.362	87.233	2.389	5.464
r1tw	238.130	67.098	3.549	5.084
r2lw	150.448	87.233	1.725	6.170
r2mw	208.362	87.233	2.389	5.464
r2tw	238.130	67.098	3.549	5.084
r3lw	150.448	87.233	1.725	6.170
r3mw	208.362	87.233	2.389	5.464
r3tw	238.130	67.098	3.549	5.084
r4lw	150.448	87.233	1.725	6.170
r4mw	208.362	87.233	2.389	5.464
r4tw	238.130	67.098	3.549	5.084
r5lw	150.448	87.233	1.725	6.170
r5mw	208.362	87.233	2.389	5.464
r5tw	238.130	67.098	3.549	5.084
r6lw	150.448	87.233	1.725	6.170
r6mw	208.362	87.233	2.389	5.464
r6tw	238.130	67.098	3.549	5.084
r7mw	208.362	87.233	2.389	5.464

APPENDIX D

MATLAB CODE FOR CRITICAL BUCLING LOAD CALCULATION

```
% Laminate definition (plies of equal thickness)
upper = [-45 90 90 45 0 0]; % input: ply angles (in degrees), bottom to symmetry
plane
lower = fliplr(upper);
thetadt = [upper,lower];
Nplies = numel(thetadt);

% Aspect Ratio a/b
% _____ a _____
% |                   |
% |                   | b
% |_____ |

a=250; b=208; %upper&lower skin middle (except zone 6)
a=165; b=208.32; %upper&lower skin middle (zone 6) a<b
a=250; b=150.448; %upper skin leading edge
a=250; b=161.78; %lower skin leading edge
a=250; b=238.13; %upper skin trailing edge
a=250; b=244; %lower skin trailing edge
a=250; b=87.233; %front spar (except zone 6)
a=165; b=87.233; %front spar (zone 6)
a=250; b=67.097; %rear spar (except zone 6)
a=165; b=67.097; %rear spar (zone 6)
a=208.362; b=87.233; %rib middle

% Ply properties
E1 = 130.e3 ; % Pa
nu12 = 0.36 ;
E2 = 8.7e3 ; % Pa
G12 = 2.9e3 ; % Pa
G13 = 2.9e3 ; % Pa
G23 = 2.9e3 ; % Pa
h_ply = 0.13 ; % SI units, mm

thetadb = fliplr(thetadt); % ply angles in degrees, from bottom
h = Nplies * h_ply ;

for i = 1:Nplies;
    zbar(i) = - (h + h_ply)/2 + i*h_ply;
end;

nu21 = nu12 * E2 / E1 ;
```

```
% Q matrix (material coordinates)
```

```
Q11 = E1 / (1 - nu12 * nu21) ;  
Q12 = nu12 * E2 / (1 - nu12 * nu21) ;  
Q22 = E2 / (1 - nu12 * nu21) ;  
Q66 = G12 ;  
Q44 = G23 ;  
Q55 = G13 ;
```

```
Q = [ Q11 Q12 0 0 0 0 ;  
      Q12 Q22 0 0 0 0 ;  
      0 0 0 0 0 0 ;  
      0 0 0 Q44 0 0 ;  
      0 0 0 0 Q55 0 ;  
      0 0 0 0 0 Q66] ;
```

```
% Qbar matrices (laminate coordinates) and contributions to ABD matrices
```

```
A = zeros(6,6);  
B = zeros(6,6);  
D = zeros(6,6);
```

```
for i = 1:Nplies;
```

```
theta = thetadb(i) * pi / 180; % ply i angle in radians, from bottom
```

```
m = cos(theta) ;
```

```
n = sin(theta) ;
```

```
T = [ m^2 n^2 0 0 0 2*m*n;  
      n^2 m^2 0 0 0 -2*m*n;  
      0 0 1 0 0 0;  
      0 0 0 m -n 0;  
      0 0 0 n m 0;  
      -m*n m*n 0 0 0 (m^2 - n^2)];
```

```
Qbar = inv(T) * Q * (inv(T))' ;
```

```
A = A + Qbar * h_ply;
```

```
B = B + Qbar * h_ply * zbar(i);
```

```
D = D + Qbar * (h_ply * zbar(i)^2 + h_ply^3 / 12);
```

```
end;
```

```
%Critical Buckling Load Nx calculation
```

```
m=linspace(1,10,100);
```

```
Nx =
```

```
D(1,1)*(m*pi/a).^2+(2*D(1,2)+4*D(6,6))*(pi/b).^2+D(2,2).*(a*pi./m).^2*(1/b)^4;
```

```
%OSLO
```

$N_x = \min(Nx)$

$\text{plot}(m, Nx)$

APPENDIX E

Table E.1: Optimum stacking sequence for the Mesh 1 / Thickness and fiber orientation angle as design variables / Strength constraint only

Zones	Stacking Sequence	Zones	Stacking Sequence
fs1	[0/90/45/0]s	rs1	[0/90/45/0]s
fs2	[0/90/45/0]s	rs2	[0/90/45/0]s
fs3	[0/90/45/0]s	rs3	[0/0/90/90/45/0]s
fs4	[0/0/90/90/45/0/0]s	rs4	[0/0/90/90/45/0]s
fs5	[0/0/90/90/45/45/0/0]s	rs5	[0/0/90/90/45/45/0]s
fs6	[0/0/0/90/90/45/45/45/0/0]s	rs6	[0/0/90/90/45/45/45/0/0]s
ls1l	[0/90/45/0]s	us1l	[0/90/45/0]s
ls1m	[0/90/45/0]s	us1m	[0/90/45/0]s
ls1t	[0/90/45/0]s	us1t	[0/90/45/0]s
ls2l	[0/90/45/0]s	us2l	[0/90/45/0]s
ls2m	[0/90/45/0]s	us2m	[0/90/45/0]s
ls2t	[0/90/45/0]s	us2t	[0/90/45/0]s
ls3l	[0/90/90/45/0/0]s	us3l	[0/0/90/90/45/0]s
ls3m	[0/90/90/45/0]s	us3m	[0/90/45/0/0]s
ls3t	[0/90/90/90/0/0]s	us3t	[0/0/90/90/45/0]s
ls4l	[0/0/90/90/45/45/0]s	us4l	[0/0/90/90/45/45/0]s
ls4m	[0/0/90/90/45/0/0]s	us4m	[0/0/90/90/45/45/0]s
ls4t	[0/90/90/90/45/0/0]s	us4t	[0/90/90/45/0/0]s
ls5l	[0/0/90/90/45/45/0/0/0/0]s	us5l	[0/0/90/90/45/45/45/45/0/0]s
ls5m	[0/0/90/90/45/45/45/0/0]s	us5m	[0/0/90/90/90/90/45/45/0]s
ls5t	[0/0/90/90/90/90/45/45/0/0/0]s	us5t	[0/0/90/90/45/45/45/0/0]s
ls6m	[0/0/90/90/90/45/45/0/0/0]s	us6m	[0/0/90/90/45/45/45/45/0/0/0]s
r1l	[0/90/45/0]s	r4m	[0/0/90/90/45/0]s
r1m	[0/90/45/0]s	r4t	[0/0/90/90/45/45/0/0]s
r1t	[0/90/45/0]s	r5l	[0/0/90/90/45/45/0/0]s
r2l	[0/90/45/0]s	r5m	[0/0/90/90/45/45/0/0]s
r2m	[0/90/45/0]s	r5t	[0/0/90/90/45/45/0/0]s
r2t	[0/90/45/0]s	r6l	[0/0/0/90/90/90/90/45/45/45/0/0/0]s
r3l	[0/90/45/0/0]s	r6m	[0/0/90/90/45/45/0/0]s
r3m	[0/90/90/0/0]s	r6t	[0/0/90/90/45/45/45/45/0/0/0]s
r3t	[0/90/90/0/0/0]s	r7m	[0/0/0/90/90/90/90/45/45/45/0/0/0]s
r4l	[0/0/90/90/45/45/0]s		

Table E.2: Optimum stacking sequence for the Mesh 2 / Thickness and fiber orientation angle as design variables / Strength constraint only

Zones	Stacking Sequence	Zones	Stacking Sequence
fs1	[0/90/45/0]s	rs1	[0/90/45/0]s
fs2	[0/90/45/0]s	rs2	[0/90/45/0]s
fs3	[0/90/45/0]s	rs3	[0/0/90/90/45/0]s
fs4	[0/0/90/45/45/0/0]s	rs4	[0/0/90/90/45/45/0/0]s
fs5	[0/0/90/90/45/45/0/0]s	rs5	[0/0/90/90/45/45/0/0]s
fs6	[0/0/90/90/45/45/45/0/0/0]s	rs6	[0/0/0/90/90/90/45/45/0/0/0]s
ls1l	[0/90/45/0]s	us1l	[0/90/45/0]s
ls1m	[0/90/45/0]s	us1m	[0/90/45/0]s
ls1t	[0/90/45/0]s	us1t	[0/90/45/0]s
ls2l	[0/90/45/0]s	us2l	[0/90/45/0/0]s
ls2m	[0/90/45/0]s	us2m	[0/90/45/45/0]s
ls2t	[0/90/45/0]s	us2t	[0/90/45/45/0]s
ls3l	[0/90/90/45/0/0]s	us3l	[0/90/90/45/0]s
ls3m	[0/0/90/45/45/0]s	us3m	[0/90/45/45/0]s
ls3t	[0/90/90/45/0]s	us3t	[0/0/90/45/45/0]s
ls4l	[0/0/90/90/45/0/0]s	us4l	[0/0/90/90/45/45/0]s
ls4m	[0/0/90/90/45/0/0]s	us4m	[0/90/90/45/0/0]s
ls4t	[0/90/90/90/45/0/0]s	us4t	[0/0/90/45/45/0]s
ls5l	[0/0/90/90/45/45/0/0/0]s	us5l	[0/0/90/90/45/45/45/0/0]s
ls5m	[0/0/90/45/45/0/0/0]s	us5m	[0/0/90/90/90/45/45/0]s
ls5t	[0/0/90/90/90/45/45/0/0/0]s	us5t	[0/0/90/90/90/90/45/45/0/0]s
ls6m	[0/0/0/90/90/90/45/45/0/0/0]s	us6m	[0/0/90/90/45/45/0/0/0]s
r1l	[0/90/45/0]s	r4m	[0/0/90/90/45/45/0]s
r1m	[0/90/45/0]s	r4t	[0/90/45/45/0/0]s
r1t	[0/90/45/0]s	r5l	[0/0/90/90/45/45/0/0]s
r2l	[0/90/45/0]s	r5m	[0/90/90/90/45/0/0/0]s
r2m	[0/90/45/0]s	r5t	[0/0/90/90/45/45/0/0]s
r2t	[0/90/45/0]s	r6l	[0/0/0/90/90/45/45/45/0/0/0]s
r3l	[0/90/90/45/0/0]s	r6m	[0/0/90/90/45/45/0/0]s
r3m	[0/90/90/45/0/0]s	r6t	[0/0/90/90/90/45/45/0/0/0]s
r3t	[0/90/90/45/0/0]s	r7m	[0/0/0/90/90/90/45/45/45/0/0/0]s
r4l	[-45/-45/90/90/45/0/0]s		

Table E.3: Optimum stacking sequence for the Mesh 3 / Thickness and fiber orientation angle as design variables / Strength constraint only

Zones	Stacking Sequence	Zones	Stacking Sequence
fs1	[0/90/45/0]s	rs1	[0/90/45/0]s
fs2	[0/90/45/0]s	rs2	[0/90/90/45]s
fs3	[0/90/90/90/45/45]s	rs3	[0/0/90/90/90/0]s
fs4	[0/0/90/90/90/90/0]s	rs4	[0/0/90/45/0/0]s
fs5	[0/90/90/90/0/0/0]s	rs5	[0/0/90/45/45/45/0]s
fs6	[0/0/90/90/90/45/45/0/0/0]s	rs6	[-45/90/90/90/45/45/45/0/0/0]s
ls1l	[0/90/45/0]s	us1l	[0/90/45/0]s
ls1m	[0/90/45/0]s	us1m	[0/90/45/0]s
ls1t	[0/90/45/0]s	us1t	[0/90/45/0]s
ls2l	[0/90/90/0]s	us2l	[0/0/90/90/0]s
ls2m	[0/90/90/0]s	us2m	[0/90/90/45/0]s
ls2t	[0/90/45/0]s	us2t	[0/90/45/45]s
ls3l	[0/90/90/90/45/45]s	us3l	[0/0/90/90/90/0]s
ls3m	[0/0/90/45/0]s	us3m	[0/90/90/90/0]s
ls3t	[0/90/90/45/45]s	us3t	[0/0/90/45/0/0]s
ls4l	[0/90/90/90/90/0/0]s	us4l	[0/0/90/90/45/0]s
ls4m	[0/90/90/90/90/90/0]s	us4m	[0/0/90/45/0/0/0]s
ls4t	[0/90/90/90/90/0/0]s	us4t	[0/0/90/90/90/90/45]s
ls5l	[0/0/0/90/90/45/45/45/0/0]s	us5l	[0/0/90/90/90/90/45/45/0/0]s
ls5m	[0/0/90/90/90/0/0]s	us5m	[0/90/45/45/0/0/0]s
ls5t	[0/0/90/90/45/45/45/45/0/0]s	us5t	[0/0/90/90/45/45/45/0/0/0]s
ls6m	[0/0/90/90/90/45/45/0/0/0/0]s	us6m	[-45/-45/90/90/0/0/0/0/0/0]s
r1l	[0/90/45/0]s	r4m	[0/90/90/90/90/45/45]s
r1m	[0/90/45/0]s	r4t	[0/90/90/45/45/0/0]s
r1t	[0/90/45/0]s	r5l	[0/0/90/90/90/90/0/0/0]s
r2l	[0/90/45/0]s	r5m	[0/90/90/90/0/0/0]s
r2m	[0/90/45/0]s	r5t	[0/90/90/90/90/90/0]s
r2t	[0/90/45/0]s	r6l	[0/0/0/0/90/90/90/90/0/0]s
r3l	[0/90/90/45/0]s	r6m	[0/0/0/0/90/90/0/0/0]s
r3m	[0/90/90/45/0/0]s	r6t	[0/0/90/90/90/90/90/0/0/0]s
r3t	[0/90/90/45/0]s	r7m	[0/45/0/0/0/0/0/0/0]s
r4l	[0/0/90/90/90/0/0]s		

Table E.4: Optimization stacking sequence for the Mesh 3 / Thickness and fiber orientation angle as design variables / Strength and local buckling constraints

Zones	Stacking Sequence	Zones	Stacking Sequence
fs1	[45/0/45/45]s	rs1	[45/45/45/45]s
fs2	[0/45/45/0/0]s	rs2	[45/90/45/45/45]s
fs3	[0/0/90/90/0/0]s	rs3	[45/45/90/90/45/45]s
fs4	[0/0/45/45/0/0]s	rs4	[0/0/0/0/0/0]s
fs5	[45/45/45/45/45/45]s	rs5	[0/0/90/90/0/0/0]s
fs6	[0/0/0/0/0/0/0/0/0/0/0]s	rs6	[0/0/0/0/0/0/0/0/0/0]s
ls1l	[0/0/0/0/0/0]s	us1l	[0/45/45/0/0/0]s
ls1m	[45/45/45/45/0/0/0]s	us1m	[0/90/0/0/0]s
ls1t	[45/90/90/45/0/0/0]s	us1t	[0/45/45/0/0]s
ls2l	[90/90/90/90/90/90]s	us2l	[0/0/0/0/45/45]s
ls2m	[90/90/90/90/90/90/45]s	us2m	[0/0/0/0/45/0]s
ls2t	[90/90/90/90/90/90/90]s	us2t	[0/45/45/0/0/0]s
ls3l	[0/0/0/0/90/90/0]s	us3l	[0/0/0/0/0/0]s
ls3m	[0/0/0/0/0/0/0/0]s	us3m	[0/0/90/90/0/0]s
ls3t	[0/0/90/90/0/0/0/90/0]s	us3t	[0/45/45/45/0/0]s
ls4l	[0/0/0/0/0/0/0]s	us4l	[0/0/0/0/0/0/0]s
ls4m	[0/0/0/0/0/0/0/0/0]s	us4m	[0/0/90/90/0/0]s
ls4t	[0/0/0/0/0/0/0/0/0]s	us4t	[0/45/45/45/0/0]s
ls5l	[0/0/0/0/0/0/0/0]s	us5l	[0/0/90/90/0/0/0]s
ls5m	[0/0/0/0/0/0/0/0/0]s	us5m	[0/0/0/0/0/0/0]s
ls5t	[90/90/90/90/90/0/0/0/0/90]s	us5t	[0/0/0/0/45//0/0]s
ls6m	[0/0/0/45/45/0/0/0/0/0/0/0]s	us6m	[0/0/0/0/0/0/0/0/0/0]s
r1l	[0/90/45/0/0]s	r4m	[0/0/45/45/45/45]s
r1m	[0/90/90/0/0]s	r4t	[0/0/90/90/90/90/90/0]s
r1t	[0/90/90/90]s	r5l	[0/0/45/45/45/0]s
r2l	[45/45/90/90/45/45]s	r5m	[0/0/90/90/45/45/0]s
r2m	[45/45/90/90//45]s	r5t	[0/0/90/90/0/0]s
r2t	[45/45/90/90/90]s	r6l	[0/0/90/90/0/0/0]s
r3l	[90/90/90/90/90/90]s	r6m	[0/0/0/0/0/0/0/0]s
r3m	[45/45/45/45/45/45]s	r6t	[0/0/45/45/0/0/0]s
r3t	[45/45/90/90/45/45]s	r7m	[0/0/45/45/45/45/45]s
r4l	[90/90/90/90/90/90]s		